Mitigating the noise of a quantum sensor in single-spin nuclear magnetic resonance

Von der Fakultät 8 Mathematik und Physik der Universität Stuttgart zur Erlangung der Würde eines Doktors der Naturwissenschaften (Dr. rer. nat.) genehmigte Abhandlung

Vorgelegt von
Matthias Pfender
aus Stuttgart

Hauptberichter: **Prof. Dr. Jörg Wrachtrup**
Mitberichter: **Prof. Dr. Sebastian Loth**

Tag der mündlichen Prüfung: 22.11.2018

3. Physikalisches Institut der Universität Stuttgart

2018

Publications

Parts of the results from chapter 2 appeared in

"Addressing Single Nitrogen-Vacancy Centers in Diamond with Transparent in-Plane Gate Structures." By Moritz V. Hauf, Patrick Simon, Nabeel Aslam, Matthias Pfender, Philipp Neumann, Sébastien Pezzagna, Jan Meijer, Jörg Wrachtrup, Martin Stutzmann, Friedemann Reinhard, and José A. Garrido. In: *Nano Letters* (Apr. 9, 2014). DOI: 10.1021/nl4047619

"Protecting a Diamond Quantum Memory by Charge State Control." By Matthias Pfender, Nabeel Aslam, Patrick Simon, Denis Antonov, Gergő Thiering, Sina Burk, Felipe Fávaro de Oliveira, Andrej Denisenko, Helmut Fedder, Jan Meijer, Jose A. Garrido, Adam Gali, Tokuyuki Teraji, Junichi Isoya, Marcus William Doherty, Audrius Alkauskas, Alejandro Gallo, Andreas Grüneis, Philipp Neumann, and Jörg Wrachtrup. In: *Nano Letters* 17.10 (Oct. 11, 2017), pp. 5931–5937. DOI: 10.1021/acs.nanolett.7b01796

Parts of the results from chapter 3 appeared in

"Nanoscale Nuclear Magnetic Resonance with Chemical Resolution." By Nabeel Aslam, Matthias Pfender, Philipp Neumann, Rolf Reuter, Andrea Zappe, Felipe Fávaro de Oliveira, Andrej Denisenko, Hitoshi Sumiya, Shinobu Onoda, Junichi Isoya, and Jörg Wrachtrup. In: *Science* 357.6346 (July 7, 2017), pp. 67–71. DOI: 10.1126/science.aam8697. pmid: 28572453

"Nonvolatile Nuclear Spin Memory Enables Sensor-Unlimited Nanoscale Spectroscopy of Small Spin Clusters." By Matthias Pfender, Nabeel Aslam, Hitoshi Sumiya, Shinobu Onoda, Philipp Neumann, Junichi Isoya, Carlos A. Meriles, and Jörg Wrachtrup. In: *Nature Communications* 8.1 (Oct. 10, 2017), p. 834. DOI: 10.1038/s41467-017-00964-z

Parts of the results from chapter 4 are currently under peer-review, and are available as an online pre-print

"High-Resolution Spectroscopy of Single Nuclear Spins via Sequential Weak Measure-

ments." By Matthias Pfender, Ping Wang, Hitoshi Sumiya, Shinobu Onoda, Wen Yang, Durga Bhaktavatsala Rao Dasari, Philipp Neumann, Xin-Yu Pan, Junichi Isoya, Ren-Bao Liu, and J. Wrachtrup. In: (June 6, 2018). arXiv: 1806.02181 [cond-mat, physics:quant-ph]

Further publications appeared in

"Single Spin Optically Detected Magnetic Resonance with 60–90 GHz (E-Band) Microwave Resonators." By Nabeel Aslam, Matthias Pfender, Rainer Stöhr, Philipp Neumann, Marc Scheffler, Hitoshi Sumiya, Hiroshi Abe, Shinobu Onoda, Takeshi Ohshima, Junichi Isoya, and Jörg Wrachtrup. In: *Review of Scientific Instruments* 86.6 (June 1, 2015), p. 064704. DOI: 10.1063/1.4922664

"Proposal for a Room-Temperature Diamond Maser." By Liang Jin, Matthias Pfender, Nabeel Aslam, Philipp Neumann, Sen Yang, Jörg Wrachtrup, and Ren-Bao Liu. In: *Nature Communications* 6 (Sept. 23, 2015), p. 8251. DOI: 10.1038/ncomms9251

"Nuclear Quantum-Assisted Magnetometer." By Thomas Häberle, Thomas Oeckinghaus, Dominik Schmid-Lorch, Matthias Pfender, Felipe Fávaro de Oliveira, Seyed Ali Momenzadeh, Amit Finkler, and Jörg Wrachtrup. In: *Review of Scientific Instruments* 88.1 (Jan. 2017), p. 013702. DOI: 10.1063/1.4973449

Contents

Summary

Introduction

In the year 1946, Edward Purcell and Felix Bloch first detected the faint signal originating from nuclear spins placed inside a magnetic field. When Erwin Hahn, in the beginning of the 1950s, introduced the concept of short radio frequency (RF) pulses to induce rotations of the nuclear spins by a known angle, the concept of RF pulse sequences was born. Shortly thereafter, he published his work on spin echoes, the principles of which are still fundamental to modern day nuclear magnetic resonance (NMR), as well as this thesis. Since the nuclear spin Larmor precession frequency depends on the particular nuclear spin species, as well as on their chemical environment, it allows the characterization of the chemical composition of a multitude of molecules in NMR spectroscopy, including organic compounds, as for example proteins.

In magnetic resonance imaging (MRI), the shift of the resonances originating from a spatially variable magnetic field is used to reconstruct an image of nuclear spin properties. This is famously used in MRI machines in hospitals all over the world, providing a non-invasive method for diagnostics. When increasing the spatial resolution of this technique, the amount of spins contributing to the signal decreases, and thus the observed signal. Therefore, the investigation of samples on the length scale of micrometer is not possible when using inductive coils for detection.

In the last few years, alternative detectors, for example magnetic resonance force microscopy (MRFM) or nitrogen-vacancy centers in diamond have emerged as a new class of sensors. Due to their small effective size (a few nanometers), they can be brought closely to an object under study, and hence detect the very weak NMR signal originating from nanometer sized samples. This paves the way towards nanoscale NMR, capable of imaging structures that are much too small for conventional MRI machines. These sensors are furthermore compatible with NMR spectroscopy, which can enable the chemical analysis of samples with a spatial resolution of $\sim 10\,\mathrm{nm}$. These length scales are small enough to gain valuable inside about fundamental processes occurring in living cells. However, since the nuclear spin is a property of the atomic nucleus, the fundamental limit of NMR spectroscopy or MRI is the observation and characterization of a single nuclear spin. While the detection of single proton spins has been shown, the characterization thereof is still unpaved territory.

In classical NMR spectroscopy, the precession of the nuclear spins is only slightly per-

turbed by their environment (including the measurement apparatus), which allows the extraction of structural information from the obtained spectra. For single spin NMR, however, the inherent strength of interaction between sample and detector will inevitably cause disturbance of the system under study.

This thesis

In this work, experiments were performed using the nitrogen-vacancy center (NV center) in diamond as a sensor. It consists of a substitutional nitrogen atom in the carbon lattice of diamond, with an adjacent vacancy. Single defects can be detected optically, and its inherent electron spin used as a sensor for various quantities. The most significant feature, however, is that the initialization and measurement of the electron spin works at room-temperature, enabling experiments under biological conditions. In recent years, this optically detected magnetic resonance (ODMR) has made NV centers prime candidates for quantum information processing, detectors for electric and magnetic fields and temperature. Even the faint magnetic field signal originating from ensembles of nuclear spins in nanoscale volumes could be detected. In this work, the influence of the NV center in NMR spectroscopy of single spins is investigated for various cases.

Due to its fundamental role in forming the NV center, the intrinsic nitrogen nuclear spin is probably the first contact with NMR for many experimentalists working on NV centers. Since nitrogen nuclei mainly exist in the stable isotopes ^{14}N ($C \approx 99.5\%$) and ^{15}N($C \approx 0.5\%$), both of which exhibit a nuclear spin of $I = 1$ or $I = 1/2$, respectively, a nuclear spin free NV center is not possible. Owing to the close proximity between the nuclear and the electron spin, their mutual coupling is quite large ($\sim$ MHz), which invites the use of the two quantum mechanical systems as qubits, to form small quantum registers. The influence of the NV center electron spin on this nuclear spin is twofold. It enables manipulation and readout to the otherwise inaccessible nuclear spin qubit, by acting as an ancillary qubit. This interaction, however, also effectively couples the nuclear spin to the environment, for example to phononic excitations in the diamond lattice. While coherence times of well separated nuclear spins in solids can reach minutes or even hours, the nitrogen nuclear spin lifetime is limited by the electron spin to a few milliseconds. In order to overcome this dilemma, a surface gate structure comprising hydrogen and oxygen terminated surfaces was placed on the diamond surface. By applying a voltage to two adjacent hydrogen region, separated by a small oxygen region, the Fermi level in the diamond crystal close to the surface can be changed. By this, the charge state of an NV center placed in the volume of varying Fermi level can be changed. When increasing the bias voltage, a transition from NV$^-$, the most prominent charge state, to NV^0 can be observed. By further increasing the voltage, a second ionization occurs, to a yet unknown charge state: the positive charged NV$^+$. In this work, the nitrogen nuclear spin is used in NMR experiments to gain insight into this deterministic manipulation of the charge

states. The newly discovered NV^+ is shown to have electron spin $S = 0$, enabling some very interesting experiments. By initializing and reading out the nuclear spin while in NV^-, its coherence can be probed while the NV center is ionized to the positive, spinless charge state. This removes electron spin mediated couplings to the environment, and thus prolongs the coherence time significantly. The findings could potentially enable the implementation of a Kane-like quantum processor in diamond, where the nuclear spins act as quantum bits (qubits), and inter-qubit coupling, as well as interaction with the measurement apparatus switched by gate voltages.

There are other single nuclear spins accessible by the NV center, namely ^{13}C nuclear spins in the diamond lattice. Carbon mainly consists of two stable isotopes, the nuclear spin-less ^{12}C, as well as ^{13}C, which has spin $I = 1/2$. In naturally occurring carbon sources, the ^{13}C abundance is around 1%. Due to the stochastic placement in diamond, every NV center couples to a few ^{13}C spins that are placed stochastically in the diamond crystal. By changing the ^{13}C concentration in the raw material used for diamond growth, the density and thus the average coupling strength can be tuned. When choosing a ^{12}C concentration of 99.995%, for example, the coupling to the ^{13}C bath is around a few kilohertz. Due to the NV center electron spin lifetime, this is on the edge of detectability, and hence a prime testbed for characterizing the capabilities of the NV center as a sensor for single spin NMR. In order to perform spectroscopy with high spectral resolution, first the NV center needs to be improved. Due to the nature of quantum sensing, the resolution is limited by the electron spin decay time. By placing the experiment in a high magnetic field of 1.5 T, the nitrogen nuclear spin state is robust again cross-relaxation with NV center electron spin. In fact, its relaxation time increases to around 4 minutes, which is enough for any kind of NMR spectroscopy task. By using a novel detection sequence based on entangled states between electron spin (sensor) and nuclear (memory) spin, a robust and versatile framework for detecting NMR spectra of different nuclear spins is developed. This hybrid spin qubit combines the best of both spins: high sensitivity of magnetic field detection by the sensor spin, and long storage and correlation times by the memory spin.

However, similar to the case of the strong coupled nitrogen nuclear spin, the NV center electron spin mediates a coupling between the environment, e.g. phononic excitations in the diamond lattice, and the ^{13}C spin under study. This limits the free evolution of the spin on a timescale of the spin relaxation time of the sensor spin, and hence a spectral resolution of around 100 Hz. Since contributions to the spin Larmor frequency, as for example chemical shift and J-coupling are usually smaller, it is necessary to mitigate this deleterious effect of sensor to target coupling. By using the robustness of the memory spin against manipulation and optical excitation of the NV center electron spin, the dissipative effect of the sensor spin can be sped up to be faster than the coupling strength between sensor and target, reaching a regime of motional narrowing of the target spin. As a result,

the linewidth is decreased by a factor of 10. Different methods of dissipative decoupling are discussed, and the scaling with the sensor to target coupling is calculated. This allows predictions about the detection of single nuclear spins on the diamond surface, as well as the prospects of performing high spectral resolution NMR spectroscopy.

One drawback of NMR measurements with NV centers in diamond are the long accumulation times, often several hours. There are mainly two reasons for this. First, one optical readout cycle of the NV center electron spin only ends up in 0.1 photons with 30% contrast, and hence a very low signal-to-noise ratio (SNR) of only 0.1. Secondly, since readout of the sensor and the free evolution necessary for the NMR spectra are done in an alternating fashion, the long evolution times necessary for high spectral resolution decrease the readout rate of the sensor spin drastically. Recently, new measurement schemes for the detection of alternating magnetic fields were introduced, where the evolution of the detected signal and readout of the sensor is interleaved. This technique is called Qdyne, short for quantum heterodyne detection, due to its similarities with heterodyne detection schemes in classical signal processing. When detecting an AC magnetic field with the NV center, the resulting spin state that is read out depends on the phase between measurement sequence and signal. Since this phase evolves constantly, undisturbed by the measurement, correlations between subsequent measurements can be used to reconstruct the signal. The reconstructed signal does not exhibit any dependence on the spin lifetime, and can therefore be characterized by its inherent lifetime and frequency. In addition, since measurements on the sensor spin are performed more frequently than in conventional methods, accumulation times are reduced drastically.

There is, however, one drawback when applying this scheme to NMR spectroscopy of single nuclear spins. Here, the oscillating magnetic field stems from the Larmor precession of the nuclear spin around its quantization axis, in the plane spanned by its x and y axis. The measurement with the sensor spin thereof constitutes a measurement of the nuclear spin expectation value along one of these axes. Since one fundamental law of quantum mechanics is the collapse of a wavefunction upon measurement, this oscillation is disturbed by the measurement. In order to counteract this phenomenon, weak measurements as introduced by Yakir Aharonov in 1988 are employed. By freely choosing the strength of the measurement on the precessing nuclear spin, the measurement-induced back-action can be mitigated. When varying the parameters of the measurement, a phase transition between a quantum Zeno regime, where the nuclear spin state is trapped by the measurement, and a regime of unperturbed oscillation can be seen. By employing further readout enhancement of the sensor electron spin by means of an ancillary readout buffer (the host nitrogen nuclear spin), the free precession of a single ^{13}C spin can be observed up to a timescale of 90 ms, with a concomitant spectral resolution of 3.8 Hz. Due to the low signal accumulation time and high spectral resolution when observing single spins, this method will be of great importance in the field of single spin NMR when using the

NV center in diamond as a quantum sensor.

Thesis Outline

This thesis is separated in four chapters. In chapter 1, the NV center in diamond is introduced as a quantum sensor. The optical properties that lead to the room-temperature readout and initialization of a single spin are explained, followed by the main workhorse in NV based sensing: microwave (MW) pulse sequences.
Chapter 2 examines charge states of the NV center. By employing a surface gate structure on the diamond surface, a deterministic method to change the Fermi level of the diamond is introduced. The concomitant change of the charge state is detected by using the host nitrogen nuclear spin as a charge state probe. The previously known neutral charge state, as well as the evasive positive charge state are observed. Since NV^+ does not have unsaturated electrons, the host nitrogen coherence is prolonged significantly. Parts of this chapter have been previously published in [1, 2].
In chapter 3, single nuclear spin NMR spectroscopy is performed on ^{13}C spins in the diamond lattice. By combining the NV center electron and nitrogen nuclear spin to a hybrid spin register, the sensor mediated coupling to the environment can be characterized as the primary cause for decoherence of the ^{13}C spins, and eliminated. Parts of this chapter have been previously published in [3, 4]
Chapter 4 introduces a new detection scheme, capable of performing much faster measurements of oscillating magnetic fields, which is then transferred to the detection of single nuclear spins. Since it relies on interleaving free evolution and measurements of the nuclear spin, the observed dynamics show a phase transition between free evolution and a quantum Zeno regime, depending on the measurement parameters. Parts of this chapter are currently under peer-review, and are available as a pre-print [5].

Zusammenfassung

Einführung

Im Jahr 1946 detektierten Edward Purcell und Felix Bloch zum ersten Mal das schwache Signal, welches durch Kernspins in einem Magetfeld hervorgerufen wird. Als Erwin Hahn kurz darauf, am Anfang der 1950er Jahre, die Verwendung von kurzen Radiofrequenz (RF) Pulsen zur Rotation der Kernspins um einen bekannten Winkel einführte, erschuf er damit die erste RF Puls Sequenz. Kurz darauf veröffentlichte er seine Arbeit zu Spin Echos, die selbst heute noch ein zentraler Bestandteil moderner Techniken der Kernspinresonanz (NMR), als auch der vorliegenden Dissertation sind. Die Frequenz der Larmorpräzession der Kernspins ist sowohl von der Art des Spins, als auch dessen chemischer Umgebung abhängig. Dies ermöglicht die Charakterisierung des chemischen Aufbaus einer Vielzahl von Molekülen, inklusive vieler organischer Stoffe wie zum Beispiel Proteine, in der Kernspinresonanzspektroskopie (NMR).
In der Kernspinresonanztomographie (MRI) wird ein örtlich variables Magnetfeld dazu verwendet, ein räumliches Bild von Kernspineigenschaften zu rekonstruieren. Die bekannteste Anwendung ist die Verwendung von Kernspinresonanztomographen in Kliniken überall auf der Welt, welche ein nicht-invasives Werkzeug der Diagnostik darstellt.
Möchte man die räumliche Auflösung dieser Technik verbessern, so verringert man dadurch automatisch die Anzahl an Spins, die zum Gesamtsignal beitragen, und dadurch auch die gemessene Signalstärke. Dadurch wird es schwierig, Objekte auf Mikrometer Ebene zu untersuchen, wenn man wie bisher Induktionsspulen zur Detektion verwendet.

In den vergangenen Jahren wurden neuartige Sensoren, wie zum Beispiel Magnetresonanz Kraftmikroskopie (MRFM) oder Stickstofffehlstellenzentren in Diamant (NV Zentren) vorgestellt, die sehr nahe (wenige Nanometer) an zu untersuchende Objekte herangeführt werden können, und dadurch das sehr schwache Kernspinsignal von Proben auf der Nanometerskala detektieren können. Dies ermöglicht NMR auf einer Nanometer Längenskala, wodurch Strukturen dargestellt werden können, die anderweitig zu klein für konventionelle Magnetresonanztomographen wären. Weiterhin sind diese Sensoren dazu in der Lage NMR Spektroskopie durchzuführen, was zur chemischen Analyse von Proben auf einer Länge von $\sim 10\,\mathrm{nm}$ verwendet werden könnte. Diese Längenskala ist klein genug, um damit wertvolle Einblicke in fundamentale Prozesse zu erhalten, die sich in lebenden Zellen abspielen.
Da der Kernspin allerdings eine Eigenschaft des Atomkerns ist, ist das fundamentale Li-

mit der NMR die Beobachtung und Charakterisierung eines einzelnen Kernspins. Auch wenn einzelne Protonenspins bereits detektiert wurden, ist ihre Charakterisierung bisher eher unzureichend.
In der klassischen NMR Spektroskopie werden die im Magnetfeld präzedierenden Kernspins nur sehr schwach von ihrer Umgebung (dies beinhaltet den Messapparat) beeinflusst. Dies erlaubt es, Rückschlüsse über deren chemische Struktur aus den Spektren zu erhalten. In der Einzelspin-NMR muss die Wechselwirkung zwischen Probe und Sensor notwendigerweise viel stärker sein, was zu einer unausweichlichen Beeinflussung des zu untersuchenden Systems führt.

Diese Arbeit

Im Rahmen dieser Arbeit wurden Experimente durchgeführt, bei denen das Stickstofffehlstellen-Zentrum in Diamant (NV Zentrum) als Sensor verwendet wurde. Dieses besteht aus einen Stickstoffatom, welches ein Kohlenstoffatom im Kristallgitter des Diamanten ersetzt, sowie einem benachbarten leeren Gitterplatz (Fehlstelle). Einzelne solche Defekte kann man optisch detektieren. Der mit dem Defekt einhergehende einzelne Elektronenspin kann als Sensor für vielfältige physikalische Größen verwendet werden. Die wichtigste Eigenschaft ist jedoch, dass die Initialisierung und Messung des Spins bei Raumtemperatur möglich ist, und damit unter Bedingungen die bei Anwendungen in biologischen Systemen gegeben sind. In den vergangenen Jahren hat diese optisch detektierte Magnetresonanz (ODMR) dazu geführt, dass NV Zentren zur Quanteninformationsverarbeitung und zur Detektion von elektrischen und magnetischen Feldern, sowie von Temperatur verwendet wurden. Sogar das schwache magnetische Signal von einer wenige Nanometer großen Menge an Kernspins konnte detektiert werden. In dieser Arbeit wurde der Einfluss des NV Zentrums auf das Ergebnis von NMR Spektroskopie, durchgeführt an einzelnen Kernspins, untersucht.

Dadurch dass jedes NV Zentrum einen eigenen Kernspin, den des Stickstoff Kerns, besitzt, ist dieser der erste Berührungspunkt für viele Experimentalphysiker die sich mit NV Zentren beschäftigen. Da Stickstoff hauptsächlich in den zwei stabilen Isotopen ^{14}N und ^{15}N vorkommt, die jeweils einen Kernspin $I = 1$ bzw. $I = 1/2$ besitzen, ist ein NV Zentrum ohne eigenen Kernspin nicht möglich. Durch die kurze Distanz zwischen dem Elektronen- und Kernspin ist ihre Kopplung relativ stark ($\sim$ MHz), was eine Anwendung der beiden Quantenmechanischen Systeme als qubits, und deren Verbindung zu einem kleinen Quantenregister, ermöglicht. Der Elektronenspin des NV Zentrums hat zweierlei Einfluss auf den Kernspin. Als Hilfsqubit ermöglicht er das Auslesen und die gezielte Kontrolle des Kernspins, welcher ansonsten nicht zugänglich wäre. Auf der anderen Seite koppelt diese Wechselwirkung den Kernspin auch an die weitere Umgebung, zum Beispiel an phononische Anregung im Diamantgitter. Während die Kohärenzzeiten gut separierter Kernspins in Festkörpern durchaus Minuten oder sogar Sunden erreichen können, ist die

Lebenszeit des Stickstoff Kernspins durch den Elektronenspin auf wenige Millisekunden beschränkt.
Um dieses Dilemma zu umgehen wurden Gatterstrukturen mithilfe von Sauerstoff- und Wasserstoffterminierung der Oberfläche hergestellt. Indem zwischen zwei, durch eine Sauerstoffregion getrennte, benachbarten Wasserstoffregionen eine Spannung angelegt wird, kann das Fermi-Niveau innerhalb des Diamanten verändert werden. Dadurch kann der Ladungszustand eines in der Nähe liegenden NV Zentrums verändert werden. Bei Änderung dieser Gittervorspannung kann eine Veränderung des Ladungszustandes vom bekannten NV^- zu NV^0 beobachtet werden. Verändert man diese Spannung weiter, so erfolgt eine zweite Ionisierung des Zentrums, zu einem bisher unbekannten Ladungszustand: Dem positiv geladenen NV^+. In dieser Arbeit wurden am Stickstoff Kernspin NMR Messungen durchgeführt, um damit Kenntnis über die deterministische Manipulation des Ladungszustandes des NV Zentrums zu erlangen. Es wird gezeigt, dass der neu entdeckte Ladungszustand NV^+ einen Elektronenspin von $S = 0$ besitzt, was einige sehr interessante Experimente ermöglicht. Durch die Initialisierung und das Auslesen des Kernspins in NV^-, kann seine Kohärenzzeit gemessen werden, während das NV Zentrum in den positiven, spinlosen Ladungszustand ionisiert wurde. Dies entfernt Wechselwirkungen mit der Umgebung, welche zuvor durch den Elektronenspin ermöglicht wurden, was zu einer deutlichen Erhöhung der Kohärenzzeit führt. Diese Ergebnisse haben das Potential, in einem Quantenprozessor nach Kane verwendet zu werden, bei dem Kernspins als qubits verwendet werden, deren Wechselwirkung untereinander sowie zur Messapparatur durch Gatterspannungen geschaltet werden können.

Im Diamantgitter befinden sich noch weitere Kernspins, hauptsächlich das ^{13}C Isotop. Kohlenstoff besteht hauptsächlich aus zwei verschiedenen stabilen Isotopen, ^{12}C ohne Kernspin, sowie ^{13}C welches einen Kernspin $I = 1/2$ besitzt. In natürlich vorkommendem Kohlenstoff beträgt das Vorkommen von ^{13}C rund 1%. Durch die zufällige Verteilung im Diamantgitter ist jedes NV Zentrum an mehrere ^{13}C Kernspins gekoppelt. Die Dichte, sowie die durchschnittliche Kopplungsstärke zwischen den Kernspins und dem NV Zentrum, kann durch Änderung der ^{13}C Konzentration während der Herstellung des Diamanten kontrolliert werden. So beträgt die durchschnittliche Kopplung des ^{13}C Kernspinhintergrunds an ein NV Zentrum einige wenige Kilohertz, wenn man bei der Herstellung eine ^{12}C Konzentration von 99.995% wählt. Aufgrund der Lebenszeit des Elektronenspins, befinden sich diese Kernspins am Rande der Empfindlichkeit des Sensors und eignen sich dadurch als Testumgebung, um NV Zentren als Sensoren für NMR Spektroskopie zu charakterisieren. Um NMR Spektroskopie mit hoher spektraler Auflösung durchzuführen, müssen zuerst einmal die Eigenschaften des NV Zentrums verbessert werden. Aufgrund der Art und Weise, wie Quantenmechanische Sensorik funktioniert, ist die spektrale Auflösung durch die Zerfallszeit des Elektronenspins begrenzt. Indem man das Experiment in ein hohes Magnetfeld von 1.5 T setzt, wird der Stickstoff Kernspin unempfindlich gegenüber

einer Kreuzrelaxation mit dem NV Elektronenspin. Tatsächlich verlängert sich die Relaxationszeit auf ungefähr 4 Minuten, was für jegliche Anwendung in der NMR Spektroskopie ausreichend ist. Indem eine neuartige Detektionssequenz verwendet wird, die mit verschränkten Zuständen von Elektron- (Sensor-) und Kernspin (Speicherspin) arbeitet, kann eine robuste und vielseitige Platform zur Detektion von NMR Spektren unterschiedlicher Kernspinarten entwickelt werden. Dieses hybride Spin Qubit verbindet die guten Eigenschaften beider Spintypen: die hohe Sensitivität auf Magnetfelder des Sensorspins, sowie die langen Speicher- und damit Korrelationszeiten des Speicherspins.
Allerdings erzeugt der Elektronenspin, ähnlich wie bei dem vorher diskutierten Stickstoff Kernspin, eine Wechselwirkung des ^{13}C Kernspins mit der Umgebung. Dies beschränkt die ungestörte Entwicklung des Kernspins auf einer Zeitskala die der Lebenszeit des Elektronenspins entspricht, und damit die spektrale Auflösung auf ungefähr 100 Hz. Da wichtige Beiträge zur Resonanzfrequenz der Kernspins, wie zum Beispiel die chemische Verschiebung und die J-Kopplung für gewöhnlich kleiner sind, ist es nötig, diesen negativen Einfluss des Elektronenspins zu verhindern. Indem man die Stabilität des Speicherspins gegenüber optischer Anregung des Sensorspins verwendet, kann die Wechselwirkung zwischen Sensorspin und Umgebung beschleunigt werden, so dass sie schneller als die Kopplungsstärke zwischen Sensor- und Zielspin ist. Dann wird die Wechselwirkung aufgrund schneller Fluktuationen zu Null gemittelt. Das Resultat ist eine Verringerung der Linienbreite um einen Faktor 10. In dieser Arbeit werden verschiedene Methoden zur Erzeugung dieser schnellen Fluktuationen besprochen, sowie deren Wirkung auf Kernspins unterschiedlicher Kopplungsstärke berechnet und gemessen. Dadurch lassen sich Aussagen über die Detektion von einzelnen Kernspins an der Oberfläche des Diamanten treffen, sowie zur Möglichkeit der Hochaufgelösten NMR Spektroskopie an einzelnen Kernspins.

Ein Nachteil von NMR Messungen mit NV Zentren in Diamant sind lange Messzeiten, welche oft mehrere Stunden betragen. Dafür gibt es hauptsächlich zwei Gründe. Einerseits führt ein einzelner optischer Auslesevorgang eines NV Zentrums im Durchschnitt nur zu ungefähr 0.1 Photonen, mit einem Signalkontrast von ca. 30%, und einem damit einhergehenden Signal-zu-Rausch Verhältnis (SNR) von nur 0.1. Andererseits, da die ungestörte Evolution der Zielspins und das Auslesen des Elektronenspins immer abwechselnd geschehen, führen lange Evolutionszeiten (welche für hohe spektrale Auflösung benötigt werden) zu einer stark verringerten Ausleserate des Sensorspins. Vor Kurzem wurde eine neue Messtechnik für die Detektion von magnetischen Wechselfeldern mithilfe von NV Zentren eingeführt, bei der die Evolution des detektierten Signals sowie das Auslesen des Sensors ineinander verschachtelt sind. Diese Technik nennt sich Quantenmechanische Heterodyne Detektion (kurz: Qdyne), aufgrund der starken Ähnlichkeit mit Heterodyner Detektion in der klassischen Signalverarbeitung. Detektiert man ein magnetisches Wechselfeld mit einem NV Zentrum, so hängt der finale Spinzustand von der Phase zwischen der Detektionssequenz und des Wechselfeldes ab. Da diese Phase sich unbeeinflusst von

der Messung des Sensorspins kontinuierlich weiterentwickelt, können Korrelationen zwischen benachbarten Messungen dazu verwendet werden, das Signal zu rekonstruieren. Diese Rekontruktion ist unabhängig von der Lebenszeit des Sensorspins, und kann daher mit einer dem Wechselfeld inhärenten Genauigkeit charakterisiert werden. Da Messungen des Sensorspins häufiger stattfinden, als in konventionellen Messmethoden, werden Messzeiten stark verringert.
Es gibt allerdings einen gravierenden Nachteil, wenn man diese Technik für NMR Spektroskopie an einzelnen Kernspins verwendet. In diesem Fall wird das Wechselfeld durch die Larmorpräzession der Zielspins um ihre Quantisierungsachse hervorgerufen. Die Ebene in der die Spinpräzession stattfindet ist die Ebene die durch die x- und y-Achse des Spins definiert wird. Misst man das Wechselfeld mit dem NV Elektronenspin, so misst man den Erwartungswert des Zielspins entlang einer dieser Achsen. Da ein quantenmechanischer Zustand in einen Eigenzustand des Messoperators zerfällt, sobald man diesen misst, wird die Präzession des Zielspins durch die Messungen gestört. Um diesen Einfluss zu Umgehen werden schwache Messungen verwendet, wie sie von Yakir Aharonov 1988 eingeführt wurden. Indem man die Messstärke der Messung des präzedierenden Zielspins frei wählt, kann der Einfluss der Messung verhindert werden. Verändert man die Parameter der Messung, so beobachtet man einen Phasenübergang zwischen einem Quanten-Zeno Bereich, in dem der Zielspin durch die Messung fixiert ist, sowie ein Bereich der ungestörten Präzession. Verbessert man weiterhin den Auslesevorgang des Sensorspins mithilfe eines Auslesepuffers (den Stickstoff Kernspin des NV Zentrums), so kann man die ungestörte Entwicklung eines einzelnen ^{13}C Kernspins bis zu einer Zeit von 90 ms beobachten, mit einer damit einhergehenden spektralen Auflösung von 3.8 Hz. Aufgrund der geringen Messzeit trotz hoher spektraler Auflösung bei der Detektion einzelner Spins, ist diese Methode von großem Interesse für NMR an einzelnen Kernspins.

Umfang der Arbeit

Die vorliegende Arbeit ist in vier Kapitel unterteilt.
Kapitel 1 beinhaltet eine Einführung des NV Zentrums in Diamant als Quantensensor. Die optischen Eigenschaften, die zur Initialisierung und Auslesung eines einzelnen Spins führen, werden erklärt. Dem folgt eine kurze Einführung in das Thema der Mikrowellen (MW) Pulssequenzen, welche das detektieren verschiedenster physikalischer Größen erst ermöglichen.
In Kapitel 2 werden die Ladungszustände von NV Zentren untersucht. Oberflächengatterstrukturen werden dazu verwendet, gezielt das Fermi Niveau innerhalb des Diamanten zu verändern. Die damit einhergehende Änderung des Ladungszustandes wird mithilfe des Stickstoff Kernspins detektiert. Es werden sowohl der bekannte neutrale Ladungszustand NV^0, als auch der bisher unbekannte positive Ladungszustand NV^+ identifiziert. Da NV^+ keine ungepaarten Elektronen besitzt, wird die Kohärenzzeit des Stickstoff Kern-

spins stark verlängert. Teile dieser Ergebnisse wurden bereits in Ref. [1, 2] veröffentlicht. In Kapitel 3 wird NMR Spektroskopie an einzelnen ^{13}C Kernspins im Diamantgitter durchgeführt. Indem der Elektronenspin des NV Zentrums und der Stickstoff Kernspin zu einem hybriden Spinregister vereint werden, kann die von dem Elektronenspin hervorgerufene Wechselwirkung des Zielspins mit der Umgebung als primäre Ursache für Dekohärenz des ^{13}C Spins erkannt und gebannt werden. Teile dieser Ergebnisse wurden bereits in Ref. [3, 4] veröffentlicht.

Kapitel 4 führt eine neue Deketionsmethode ein, die in der Lage ist, magnetische Wechselfelder viel schneller zu messen. Diese Methode wird zur Detektion von einzelnen Kernspins eingesetzt. Da sie auf der Verschachtelung von ungestörter Evolution der Zielspins und deren Messung basiert, beobachtet man einen Phasenübergang in der Dynamik des Zielspins, abhängig von den Parametern der Messung. Teile dieser Ergebnisse befinden sich momentan im peer-review Prozess, und sind unter Ref. [5] als pre-print verfügbar.

List of Figures

List of Tables

Abbreviations

AOM acousto-optic modulator

APD avalanche photo-diode

AWG arbitrary waveform generator

CNOT gate controlled NOT gate

CPHASE gate controlled phase gate

CPMG Carr-Purcell-Meiboom-Gill

CVD chemical vapor depositions

DD dynamical decoupling

DFT Kohn-Sham density functional theory

DPSS diode-pumped solid state

ENDOR electron nuclear double resonance

ESR electron spin resonance

FFT fast Fourier transform

FWHM full width at half maximum

GSD ground-state depletion

HPHT high pressure and high temperature

ISC intersystem crossing

KDD Knill dynamical decoupling

LAC level anti-crossing

MRFM magnetic resonance force microscopy

MRI magnetic resonance imaging

MW microwave

NMR nuclear magnetic resonance

NV center nitrogen-vacancy center

OCXO oven controlled quartz oscillator

ODMR optically detected magnetic resonance

Qdyne quantum heterodyne detection

qubit Quantum bit

RF radio frequency

SNR signal-to-noise ratio

SSR single-shot readout

STORM stochastic optical reconstruction microscopy

SWAP gate SWAP gate

ZFS zero-field splitting

ZPL zero-phonon line

1. The nitrogen-vacancy center in diamond as a quantum sensor

For the last few years, the NV center in diamond has developed from an optically active single spin system [9, 10], to a small quantum register [11–20], and was furthermore employed as a room-temperature Maser [7, 21]. The most prominent application, however, is that of a formidable atomic-sized sensor capable of working at room-temperature. Measured properties range from magnetic fields [22–24] and electric fields [25–27] to temperature [28–30]. These capabilities can even be used for the detection and characterization of other spins. The NV center has been shown to be able to detect and position single nuclear spins inside the diamond [20, 31, 32], ensembles of nuclear spins outside the diamond [33–36], as well as electron spins [37–40].

This chapter will concentrate on introducing this formidable construct of nature, and explain how it can be used as a quantum sensor.

1.1. Diamond: the host material

Diamond is most probably the most prestigious form of carbon, due to its use a gemstone of different colors and shapes. The carbon atoms comprising the diamond crystal have sp^3 hybridized electron orbitals, whose tetrahedral symmetry reflects in the diamond lattice. It is of face-centered cubic shape, with the unit cell having two carbon atoms at the position $(0, 0, 0)$ and $(\frac{1}{4}, \frac{1}{4}, \frac{1}{4})$. The lattice constant is $a = 0.357\,\text{nm}$. The distance between next neighbor carbon atoms is $0.154\,\text{nm}$. From a technical or scientific viewpoint, diamond has several attributes that invite the use in material or electronic science. It is the hardest material occurring naturally that we know of [41], and can therefore be used for cutting or grinding different materials. From an electronic point of view, diamond is a semiconductor, however, due to its large band gap of $5.48\,\text{eV}$, it is an insulator in most cases. The most prominent dopants of diamond are nitrogen and boron, which are often used to characterize diamonds as follows [42]:

Type I diamonds contain a high concentration of nitrogen that is detectable with an optical spectrometer (usually around 0.1%). The **Type Ia** subtype has clustered regions of nitrogen impurities, often appearing yellow due to absorption in the blue spectral

range. **Type Ib** has lower nitrogen concentration, which is dispersed throughout the crystal. They often appear of brownish color, due to additional absorption in the green spectral range.

Type II has lower nitrogen concentration which is not detectable by optical spectroscopy. **Type IIa** are colorless diamonds with a nitrogen concentration below 1 ppm. **Type IIb** diamond is characterized by boron doping below 1 ppm, which makes it semiconducting.

Naturally occurring diamonds are created at high temperatures and high pressure, conditions that usually exist inside earth's shell. Synthetic diamonds are often produced by high pressure and high temperature (HPHT) synthesis [43], which mimics the conditions of natural growth. A source material, graphite, is converted into the more stable diamond[1] by help of a catalyst. Another way of producing diamond is the homoepitaxial growth of diamond crystals by chemical vapor deposition (CVD) [44, 45]]. A small diamond acting as a seed is grown upon under low pressure conditions, assisted by a microwave induced plasma. Due to precise control of the trace gas, the composition of the resulting diamond, including dopant concentrations, can be very well controlled.

In this work, spin properties of diamond defects are the center of attention. Two factors enable the remarkable properties of the NV center. Diamond has a very high Debye temperature of 1860 K, resulting in a very low phonon density at room temperature. Additionally, due to the high natural abundance of ^{12}C of almost 99%, the nuclear spin density in diamond is quite low. The occurrence of 1.1% of ^{13}C nuclei, that possess an $I = 1/2$ nuclear spin can conversely be used as additional quantum bits (qubits).

1.2. Formation of nitrogen-vacancy centers

The NV center in diamond, first observed by Davies et al. [46], is a point defect occupying two next neighbor lattice sites. At one site, the carbon atom is replaced by a nitrogen atom, the other is empty [47]. There are consequently four different directions of NV centers in diamond, corresponding to the tetrahedral shape of the diamond lattice. Every direction can be oriented in two ways (i.e. N-V or V-N). Energy levels corresponding to point defects often reside inside the band gap, and due to the high band gap of diamond, multiple states separated by energies corresponding to photons of visible light can exist, resulting in fluorescent defects. Because the amount of fluorescence emitted by an optically excited NV center is quite high, the optical detection of single centers using a confocal microscope is possible [48]. Hence, the NV center is often compared to a single trapped atom.

[1] Note that diamond is the more stable configuration at HPHT, but not at ambient conditions.

While NV centers occur in natural diamond crystals, they can also be created artificially. In HPHT synthesis, nitrogen can be incorporated in the crystal during growth, substituting carbon atoms. Vacancies can be created via electron irradiation. In oder to combine a substitutional nitrogen atom with a vacancy, the diamond crystal is annealed at temperatures of around 800 °C to 1000 °C for several hours. This enables the vacancies to diffuse through the diamond lattice. Upon combination with a nitrogen atom to an NV center, the stability of this defect stops the vacancy diffusion [46].

NV centers can also be created by nitrogen implantation. Nitrogen ions are accelerated via an electric field towards the diamond surface. The penetration depth depends on the kinetic energy of the particles. For moderate implantation energies of a few keV, this depth is on the order of a few nanometer. Subsequent annealing can then, similar to the case of bulk nitrogen, convert the incorporated nitrogen atoms to NV centers [49, 50].

1.3. Different charge states of the nitrogen-vacancy center

The NV center defect incorporates 5 electrons, two from the substitutional nitrogen atom, and three from the carbon dangling bonds neighboring the vacancy. This is the so called neutral charge state, NV^0. By absorption of an additional electron from the valence band or from nearby defects, another stable charge state is created, NV^-. Both charge states can be differentiated by their fluorescence emission, with the emission from NV^0 being slightly shifted towards higher photon energies (see fig. 1.1). Interestingly, a single NV center does not occur in one exclusive charge state, but can be ionized and recombined by optical excitation [51, 52]. This photo-ionization was later used unknowingly for an implementation of ground-state depletion (GSD) microscopy [53]. After identifying this dark state as the neutral charge state [54], and further investigation of the optically induced ionization and recombination [55], the neutral charge state was used for an implementation of a super-resolution technique similar to stochastic optical reconstruction microscopy (STORM) [56].

Except for a few exotic diamond crystals [57], this coexistence as well as optical interconversion of the two charge states cannot be avoided, and has to be taken into account for experiments of quantum computation [18, 54] and quantum sensinq (see chapters 3 and 4 of this thesis). The main interest, however, lies in the negative charge state NV^-. Therefore, when not further mentioned, the term "NV center" refers to the negative charge state.

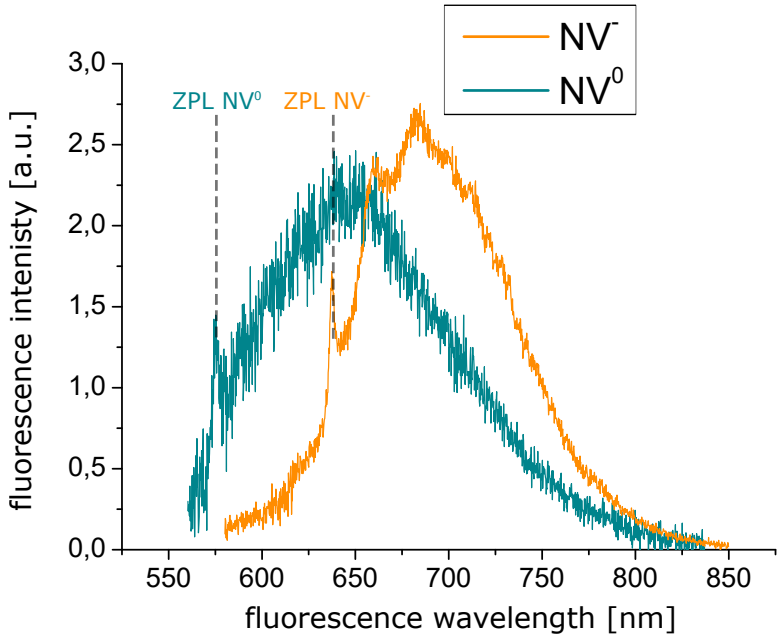

Figure 1.1.: Fluorescence emission spectra of nitrogen-vacancy centers in diamond. The NV center mainly resides in one of two charge states, NV^- and NV^0. Both can be excited by laser excitation and fluoresce at slightly different wavelength with a ZPL of 637 nm and 575 nm, respectively.

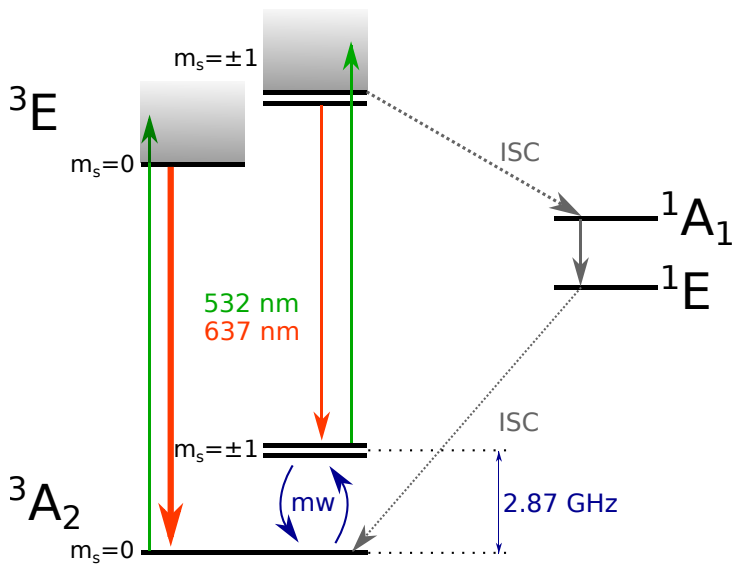

Figure 1.2.: Energy level scheme of the negatively charged nitrogen-vacancy center. Green and red arrows denote optical transitions, gray arrows are radiation-less transitions. Blue arrows show coherent transitions between spin states.

1.4. Optical properties of the NV center

The NV center triplet ground state ($^3A_2$) and excited state ^3E lie within the band gap of diamond, separated by an energy of 1.945 eV. Both of those states ($^3A_2$ and ^3E) of the NV center have an electron spin $S = 1$ submanifold. The corresponding spin states $m_s = 0$ and $m_s = \pm 1$ are split by a zero-field splitting (ZFS) of $D = 2.87$ GHz [48, 58] in the ground state, and $D = 1.42$ GHz in the excited state [59]. Off-resonant optical excitation with green ($\lambda = 532$ nm) laser light, transfers the NV center to its excited state ^3E, conserving the electron spin state. Fluorescence emission is possible for all spin states (with decay rate $\gamma = 1/(8\,\text{ns})$ for $m_s = 0$ and $\gamma = 1/(12\,\text{ns})$ for $m_s = \pm 1$ [60]) at a zero-phonon line (ZPL) of 637 nm, accompanied by a large phonon sideband. Furthermore, electron spin-orbit coupling enables an intersystem crossing (ISC) transition to the singlet $^1A_1$ state for the $m_s = \pm 1$ manifold. From there, the system decays by emitting a photon at a wavelength of around 1042 nm [61, 62][2] to the metastable state ^1E, and from there with a decay rate of $\gamma \approx 1/(250\,\text{ns})$ to the $m_s = 0$ ground state [47, 63, 64]. The system is schematically shown in fig. 1.2.

1.4.1. Optical spin initialization and readout

The energy level structure, especially the ISC to the singlet state enables some very curious and useful properties. Optical illumination of the $m_s = 0$ sublevel of the ground state excites the system to the $m_s = 0$ excited state. From there, the system relaxes back to the ground state by emitting a photon, within roughly 12 ns. Since both these transitions are spin conserving, the optical cycling and continuous emission of photons does not change the spin state. When exciting the $m_s = \pm 1$ sublevels, additionally to the transition from $m_s = 0$, an ISC transition to the singlet state is possible. Since decay via the singlet state occurs on a much longer timescale, and without the emission of detectable photons, the number of emitted photons is much lower. The $m_s = 0$ state is therefore sometimes called the bright, the $m_s = \pm 1$ levels dark states.

Since the ISC occurs between spin triplet and singlet states, it is by definition not spin conserving. Similar to the spin dependence of the transition from the triplet excited to the singlet excited state, the transition from singlet ground to triplet ground state predominantly ends up in the $m_s = 0$ spin state [47, 65]. Taking the optical cycle for $m_s = 0$, and the ISC cycle for $m_s = \pm 1$ together, the NV center electron spin can be cooled to the $m_s = 0$ ground state by optical excitation. The degree of polarization is reportedly 80% or higher for ensembles of NV centers[65].

Together, the optical spin initialization and readout, motivate the use of NV centers as quantum sensors. As it turns out, the spin state of NV centers can be read out with around 30% photon contrast, at a count rate of around 300 kcounts/s. Since the

[2] These photons are mostly not detected in our experimental setup

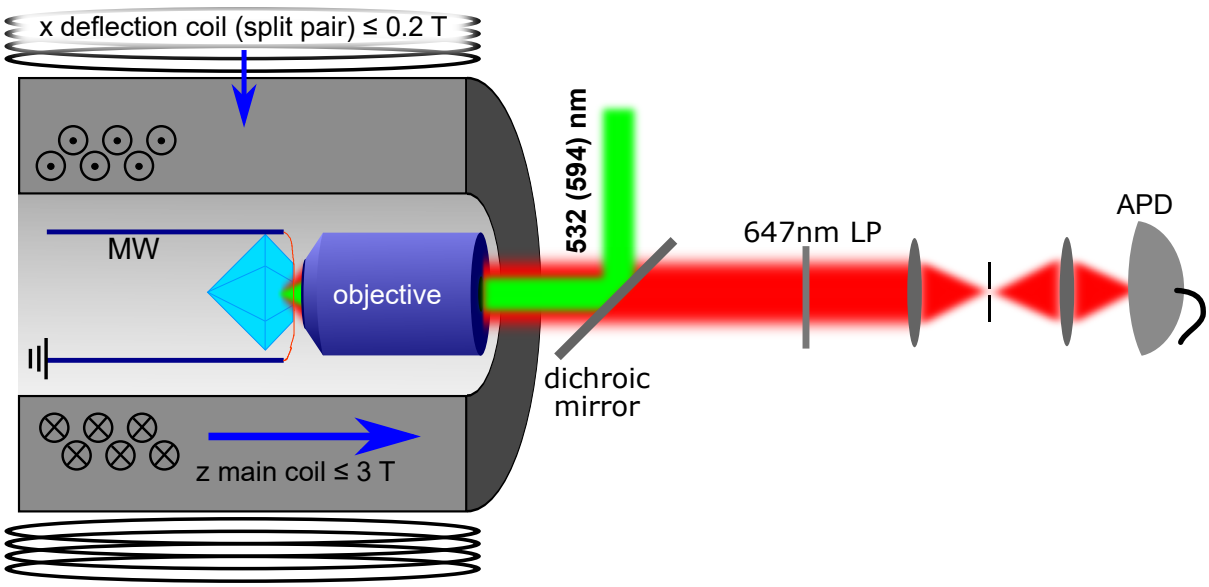

Figure 1.3.: Confocal microscope working inside a superconducting magnet. Optical excitation is performed via a pulsable green laser, focused on the diamond by an objective. By mounting the objective on a piezo-electric scanner, the focus can be moved inside the diamond. Fluorescence of an excited NV center is collected by the same objective, and after spectral and spatial filtering focused on an APD. The whole sample part of the experimental setup is positioned inside a superconducting magnet.

spin initialization under excitation occurs within $\sim 300\,\mathrm{ns}$, one readout of the NV center generates around 0.1 photons, with 30% contrast between the $m_s = 0$ and $m_s = \pm 1$ spin states. The following section introduces an experimental setup, capable of performing confocal microscopy in conjunction with single electron spin readout and manipulation.

1.5. A single spin confocal microscope

An experimental setup, capable of performing single spin electron spin resonance (ESR) on NV center in diamond can be separated into two parts. First is a homebuilt confocal microscope, with an excitation laser at around 532 nm and single photon detection. The second part is equipment capable of producing the MW and RF radiation to manipulate the spins. The experiment used in this work was furthermore placed in a superconducting magnet, able to work at magnetic fields up to 3 T.

1.5.1. The microscope

The initialization and readout of the NV center happens by optical excitation and fluorescence collection. In order to perform experiments on single defects, a homebuilt confocal

microscope is used. Excitation is done by a pulsable green laser[3], at a wavelength of 532 nm (a diode-pumped solid state (DPSS) Nd:YAG laser) or 520 nm (a semi-conductor laser diode). In order to switch the DPSS laser on and off on a timescale of a few nanoseconds, it is guided through an acousto-optic modulator (AOM). The laser diode, however, can itself be switched on a timescale of nanoseconds. By sending the excitation light through a single-mode fiber, the quality of the beam profile is increased before reaching the objective. The beam is then reflected by a dichroic mirror onto the objective (Olympus UPlanSApo 60x, oil immersion, NA=1.35), focusing the beam onto a diffraction limited spot inside the diamond. Since the objective is mounted on a piezo electric scanner, it (and hence the focus inside the diamond) can be moved on a range of 100 μm along the x and y direction, and 25 μm along z. The diamond itself is mounted on a long range piezo positioner, capable of traversing 2 cm in each direction, for raw positioning of the sample. This whole part is immersed in the bore of a superconducting magnet, capable of producing a magnetic field of 3 T along the optical axis, as well as 0.2 T in the two perpendicular axes (see fig. 1.3) At the full field amplitude of 3 T, these deflection coils can rotate the field about 5° from the optical axis. Fluorescence emitted from excited NV centers is collected by the objective, and transmitted through the dichroic mirror. Further spectral filtering with an 647 nm longpass filter removes traces of the excitation laser. Spatial filtering is done by focusing the beam through a 50 μm pinhole, before detection by an avalanche photo-diode (APD), capable of detecting single photons.

1.5.2. Spin manipulation

In order to perform meaningful spin resonance experiments, sources of coherent MW and RF radiation are needed. The resonance of the NV center electron spin ranges in the range of GHz (2.87 Ghz at zero magnetic field, up to $\sim$ 90 GHz at 3 T). Nuclear spin resonances are on the order of up to $\sim$ 120 MHz. Oscillating magnetic fields, necessary to induce Rabi oscillations on the spins, are produced by an oscillating current in a coplanar waveguide stripline, on which the diamond sample is mounted[4]. This produces a linearly polarized, oscillating magnetic field at the locate of the NV center. A schematic setup for generating RF and MW radiation can be seen in fig. 1.4. The central element is the arbitrary waveform generator (AWG) (Keysight M8190A), with a sampling rate of 12 GS/s, capable of producing MWs at frequencies up to $\sim$ 4 GHz. Since the frequency range is enough to manipulate nuclear spins, the first output of the AWG is connected directly to a RF amplifier (Amplifier-Research 150A250, frequencies from 100 kHz to 250 MHz, output power 150 W). At moderate magnetic fields, the output frequencies of the AWG are however not high enough for electron spin manipulation. The second output of the AWG is therefore connected to a harmonic mixer (Miteq DB0250LW1 for frequencies

[3]In later experiments, a second orange ($\lambda = 594$ nm) laser is added to the beampath.
[4]In some experiments, a 50 μm thick copper wire spanned across the diamond surface is used

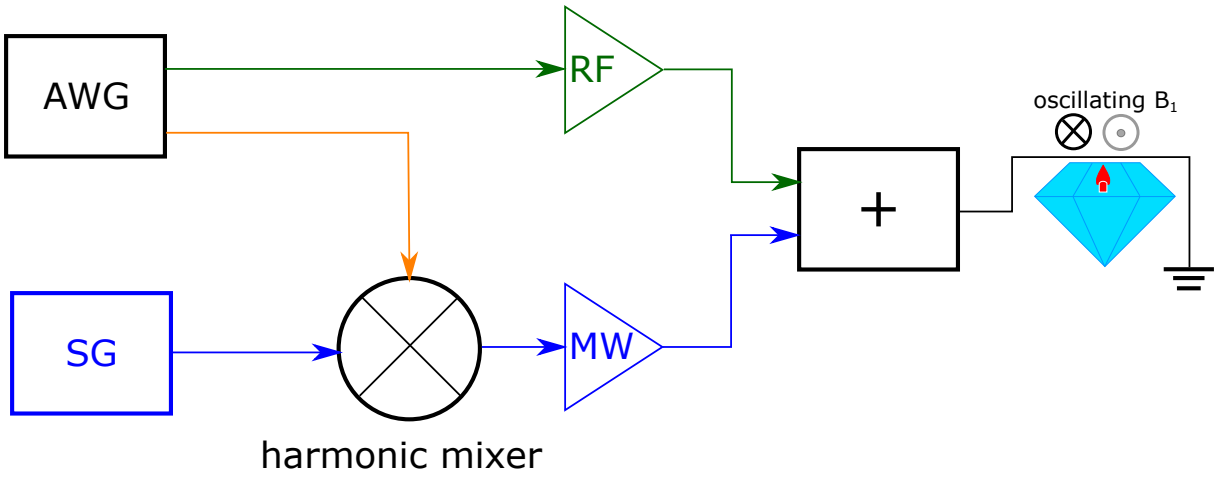

Figure 1.4.: Schematic of the experimental setup generating RF and MW radiation for electron and nuclear spin manipulation. The heart of the setup, generating pulses of different length, frequency and phase, is the AWG. RF radiation is generated directly by one output of the AWG, and amplified. Since the MW frequencies needed are out of range of the AWG, another output is mixed onto a carrier signal provided by a signal generator, and subsequently amplified. The signal is combined by a Bias Tee, and led to the coplanar waveguide stripline. The oscillating current then produces a linearly polarized magnetic field at the place of the NV center, perpendicular to its quantization axis. Colors denote the frequency range (green: $\sim 1-100$ MHz, orange: ~ 1 GHz, blue: $\sim 2-90$ GHz)

of $2-50$ GHz or Mini-Circuits ZX05-C60LH-S+ for $1.6-6$ GHz), where the signal is mixed onto a carrier signal produced by a signal generator (Anritsu MG3697C, frequencies from 0.1 Hz to 70 GHz). The mixed signal is then amplified by a MW amplifier depending on the used frequency range (Gigatronics GT-1050A for frequencies from $2-50$ GHz or Hughes 8010H traveling wave tube amplifier for frequencies from $4-8$ GHz). The amplified MW and RF signals are then combined to a single coaxial cable by a Bias Tee (Microwave Circuits D1G018G3), which is then connected to a coplanar waveguide, on which the signal is transmitted through a tapered stripline with a diameter of roughly $\sim 100\,\mu$m. The diamond sample is positioned above, with the oscillating magnetic field produced by the oscillating current in the stripline capable of manipulating electron and nuclear spins inside and outside the diamond.

1.6. Coupling of the spin to the environment

This section concentrates on the behavior of the NV center electron spin in response to the environment, including deliberate effects like the application of a constant magnetic field or oscillating magnetic fields, as well as effects intrinsic to NV centers in diamond.

The discussion will be based on the Hamiltonian of the NV center electron spin

$$H = \hat{H}^{\mathrm{el}} + \hat{H}^{\mathrm{N}} + \hat{H}^{\mathrm{C}} + \hat{H}^{\mathrm{coupl}} \tag{1.1}$$

$$\tag{1.2}$$

with the components $\hat{H}^{\mathrm{el}}$ of the single electron spin, $\hat{H}^{\mathrm{N}}$ of the single ^{14}N nuclear spin associated with the defect, the spin bath $\hat{H}^{\mathrm{C}}$ and the coupling between the spins $\hat{H}^{\mathrm{coupl}}$.

1.6.1. A magnetic bias field

The Hamiltonian of a single NV center electron spin $\hat{H}^{\mathrm{el}}$ from eq. 1.1 can be written as

$$\hat{H}^{\mathrm{el}} = D\hat{S}_z^2 + B_0\tilde{\gamma}_{\mathrm{el}}\hat{S}_z, \tag{1.3}$$

with the ZFS $D = 2.87\,\mathrm{GHz}$ of the NV center, the bias magnetic field B_0 and the reduced gyromagnetic ratio $\tilde{\gamma}_{\mathrm{el}}$ of the NV center electron spin. Experiments in this work are solely performed with magnetic fields aligned along the symmetry axis of the NV center, hence components along the x or y direction are omitted. The eigenstates of $\hat{H}_{\mathrm{el}}$ are therefore fixed to $|m_s = 0\rangle$, $|m_s = -1\rangle$ and $|m_s = +1\rangle$. The eigenenergies, and thus the transition frequencies between these states, however, depend on the magnetic field B_0 and the reduced gyromagnetic ratio $\tilde{\gamma}_{\mathrm{el}} = 28\,\mathrm{GHz/T}$. The same argument is valid for ^{14}N and ^{13}C nuclear spins.

1.6.2. An oscillating magnetic field for spin manipulation

When applying the MW radiation introduced in sec. 1.5.2, the Hamiltonian has to be extended

$$\hat{H}^{\mathrm{el}} = D\hat{S}_z^2 + B_0\tilde{\gamma}_{\mathrm{el}}\hat{S}_z + \tilde{\gamma}_{\mathrm{el}}B_1(t)\hat{S}_x \tag{1.4}$$

with the alternating magnetic field $B_1(t) = B_1^{\mathrm{amp}} \cdot \cos(\omega t)$, linearly polarized, without affecting generality, along the x axis. In order to solve this time-dependent Hamiltonian, the system is brought to the rotating frame of the applied microwave, by using the rotating-wave approximation [66]. The now time-independent Hamiltonian then is

$$\hat{H}_{\mathrm{el}}^{\mathrm{rot}} = \Delta\hat{S}_z + \tilde{\gamma}_{\mathrm{el}}B_1^{\mathrm{amp}}\hat{S}_x, \tag{1.5}$$

with the frequency detuning of the MW (and thus the rotating frame) to the transition frequency $\Delta_\pm = |D \pm \tilde{\gamma}_{\mathrm{el}}B_0| - \omega$. The plus and minus sign correspond to the $m_s = +1$ and $m_s = -1$ state, respectively. In this form, the detuning Δ causes the spin to rotate around the z axis. For the near resonance condition, $\Delta \approx 0$, the second term causes

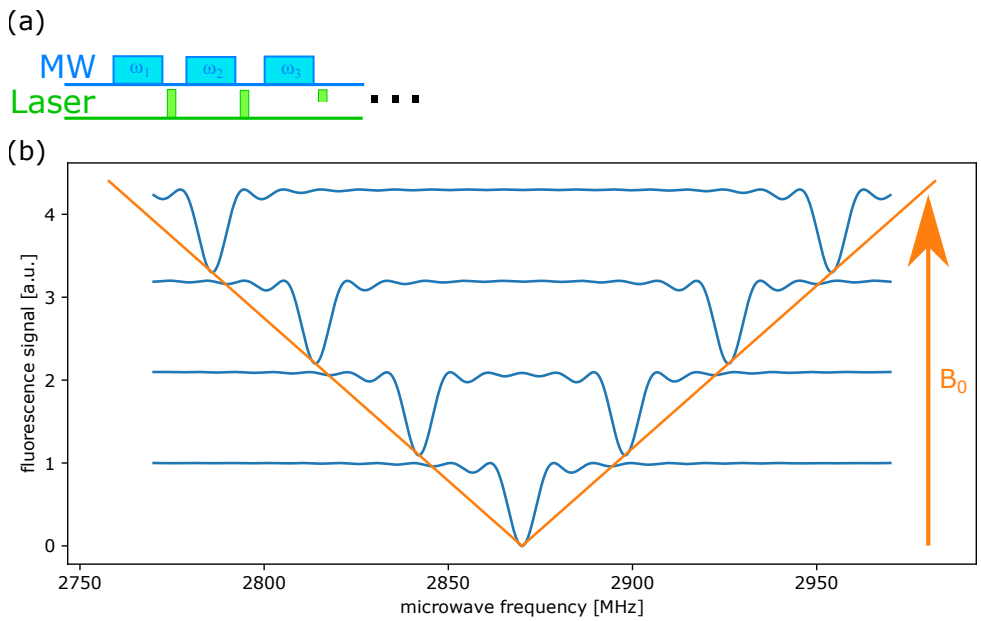

Figure 1.5.: Simulation of NV center ODMR spectra for different magnetic fields. (a) shows the sequence used to detect the spectra. The NV center is initialized to $m_s = 0$ with a green laser pulse, and subsequently manipulated by a MW pulse, that flips the spin state from $m_s = 0$ to $m_s = \pm 1$, if the frequency of the pulse is on resonance. (b) shows the resulting fluorescence over the applied MW frequency for magnetic fields of 0 G, 10 G, 20 G and 30 G (from bottom to top). The signal frequencies are marked with an orange line, the lower frequency transition belonging to the $m_s = 0$ and $m_s = -1$, the higher frequency transition belonging to the $m_s = 0$ to $m_s = +1$ transition. Due to the rectangular shape of the MW pulses, the spectra exhibit sinc-like peak functions.

the spin state to undergo Rabi oscillations around the x axis with precession frequency $\Omega = \tilde{\gamma}_{\mathrm{el}} B_1^{\mathrm{amp}}$. By using discrete MW pulses of the length $\tau_\pi = \frac{\pi}{\tilde{\gamma}_{\mathrm{el}} B_1^{\mathrm{amp}}}$ (so called π pulses) the electron spin can therefore be brought from its $m_s = 0$ state to the $m_s = \pm 1$ state, if the applied MW pulse is on resonance. By sweeping the frequency of the applied microwave radiation and observing the respective fluorescence levels, an ESR spectrum of a single NV center electron spin can be recorded (see fig. 1.5(a)). This is called ODMR. Simulated spectra for different magnetic fields can be seen in fig. 1.5(b). The signal is of sinc-like shape, due to the rectangular shaped envelope of the MW pulses.

Another important rectangular pulse is the $\pi/2$ pulse. When applying the MW radiation for $\tau_\pi/2$, the electron spin is rotated around the y axis by an angle of $\pi/2$, and if initially initialized to $m_s = 0$ ends up in the $|x\rangle$ state. Since magnetic fields induce a rotation around the z axis, the NV center spin state then oscillates over time between the $|\pm y\rangle$ and $|\pm x\rangle$ states. This will be used for magnetometry applications later on. The same argument is valid for ^{14}N and ^{13}C nuclear spins.

1.6.3. Nuclear spins in the diamond lattice

Although the diamond crystal mainly consists of ^{12}C nuclei, which are nuclear spin-less, there is a dilute spin bath due to ^{13}C nuclei. In addition, every NV center has its own nuclear spin from the host nitrogen (either ^{14}N or ^{15}N, although the latter is omitted in the following discussion). Few NV centers also exhibit strongly coupled ^{13}C nuclear spins [14, 18], this case will be neglected in the following discussion. The Hamiltonian from eq. 1.1 includes three important components

$$\hat{H}^{\mathrm{N}} = C_q^{\mathrm{N}} (\hat{I}_z^{\mathrm{N}})^2 + \tilde{\gamma}_{\mathrm{N}} B_0 \hat{I}_z^{\mathrm{N}} \tag{1.6}$$

$$\hat{H}^{\mathrm{C}} = \tilde{\gamma}_{\mathrm{C}} B_0 \sum_{\mathrm{bath}} \hat{I}_z^{\mathrm{C}} \tag{1.7}$$

$$\tag{1.8}$$

$$\hat{H}^{\mathrm{coupl}} = \underline{\hat{S}}\ \underline{\underline{A}}^{\mathrm{N}}\ \underline{\hat{I}}^{\mathrm{N}} + \underline{\hat{S}} \sum_{\mathrm{bath}} \underline{\underline{A}}^{\mathrm{C}} \underline{\hat{I}}^{\mathrm{C}} \tag{1.9}$$

$$, \tag{1.10}$$

with the quadrupole splitting of the ^{14}N nuclear spin $C_q^{\mathrm{N}} = -4.945\,\mathrm{MHz}$, the hyperfine coupling tensors $\underline{\underline{A}}$ and the respective reduced gyromagnetic ratios $\tilde{\gamma}$. The nitrogen nuclear spin and the ^{13}C spin bath will in the following be discussed separately.

The intrinsic nitrogen nuclear spin

Due to the colinearity of the ^{14}N nuclear spin's and the NV center electron spin's quantization axis, and the axis connecting their positions, the hyperfine coupling tensor $\underline{\underline{\hat{A}}}^{\mathrm{N}}$ is diagonal of the form $\underline{\underline{A}}^{\mathrm{N}} = \mathrm{diag}\left(A_\perp, A_\perp, A_\parallel\right)$ [15, 67]. Therefore, the coupling term of the Hamiltonian, for the ^{14}N nuclear spin can be written as

$$\hat{H}^{\mathrm{coupl,N}} = \underline{\hat{S}}\ \underline{\underline{A}}^{\mathrm{N}}\ \underline{\hat{I}}^{\mathrm{N}} \tag{1.11}$$

$$= \hat{S}_x A_\perp \hat{I}_x + \hat{S}_y A_\perp \hat{I}_y + \hat{S}_z A_\parallel \hat{I}_z \tag{1.12}$$

$$= \left(\hat{S}_+ \hat{I}_- + \hat{S}_- \hat{I}_+\right) A_\perp/2 + \hat{S}_z A_\parallel \hat{I}_z. \tag{1.13}$$

The first term are so-called spin flip-flop terms, that enable the exchange of spin quanta between NV center electron and ^{14}N nuclear spin. Due to the large energy mismatch between the electronic states ($\sim$ GHz) and the nuclear spin states ($\sim$ MHz), this term can be neglected when calculating the energy eigenstates of the system[5]. The parallel hyperfine interaction $A_\parallel = 2.16\,\mathrm{MHz}$ causes the electron spin spectrum from fig. 1.5(b) to exhibit a hyperfine splitting. Every line is split in three, split by 2.16 MHz each. The resulting spectra can be seen in fig. 1.6. Further information about the ^{14}N nuclear

[5] This is the so called secular approximation, all terms in the Hamiltonian containing electron spin operators aside from $\hat{S}_z$ are neglected.

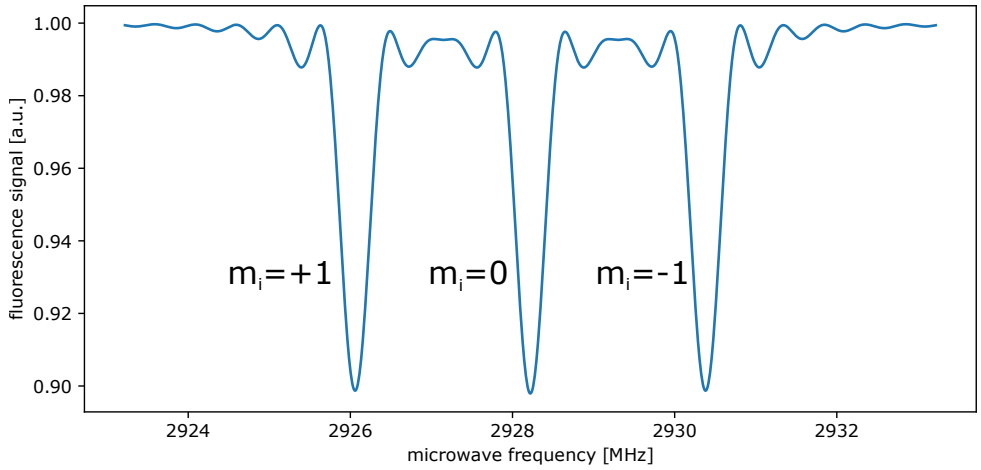

Figure 1.6.: Simulated hyperfine spectrum of the $m_s = 0$ to $m_s = +1$ electron spin transition, split due to the hyperfine interaction with the ^{14}N nuclear spin. The pulse length of a π pulse was set to $2\,\mu$s, to increase the spectral resolution. Each of the lines can be attributed to one nuclear spin state $m_i = -1, 0, +1$

spin can be found in sec. 1.8, where it is introduced as a robust memory for quantum information.

^{13}C spin bath

For ^{13}C spins dispersed inside the diamond, the case looks slightly different. First of all, the line connecting NV center electron and ^{13}C nuclear spin is in general not parallel to the external magnetic field. Consequently, the hyperfine tensor $\underline{\underline{A}}^{\mathrm{C}}$ is not diagonal, but also contains terms connecting spin operators along different axis, e.g. $\hat{S}_z A_{zx} \hat{I}_x$. Similar to the case of the ^{14}N nuclear spin, terms containing $\hat{S}_x$ or $\hat{S}_y$ can be neglected due to the secular approximation at high magnetic fields [15, 67]. The multitude of remaining terms is two-fold.

The term $\hat{S}_z A_{zx} \hat{I}_z$, similar to the ^{14}N nuclear spin, hyperfine splits the NV center electron spin transition, according to the respective coupling of each ^{13}C nuclear spin in the bath. For natural abundance concentration of ^{13}C spins ($\sim 1.1\%$), this results in couplings of up to $\sim 100\,$kHz. The smaller the coupling of the ^{13}C spin, the more possible sites exist in the diamond lattice. The overlap of all hyperfine splittings of spins comprising the ^{13}C spin bath is called the Overhauser field [68]. It limits the achievable T_2^* lifetime of the NV center electron spin.

The second group of terms are of the form $\hat{S}_z A_{zx} \hat{I}_{(x,y)}$. Since a nuclear spin oriented along its $|x\rangle$ axis (or $|y\rangle$, for that matter) rotates around the z axis with a frequency corresponding to the Larmor frequency of the spin, it can be seen as generating an oscillating magnetic field with amplitude A_{zx} at the place of the NV center electron spin. Since

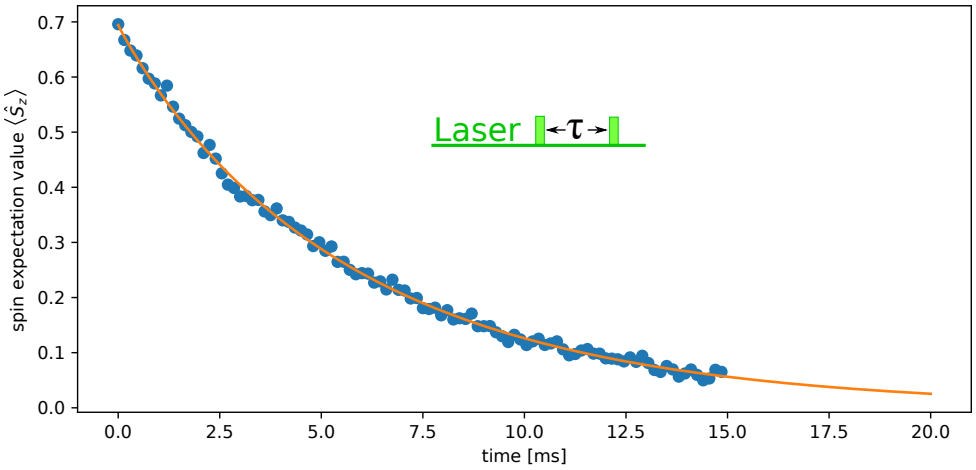

Figure 1.7.: This figure shows the exponential decay of the NV center electron spin state over time, without optical excitation. The signal decays on a timescale of $T_1 = 5.9\,\mathrm{ms}$. The inset shows the measurement sequence. A green laser pulse polarizes the NV center to its $m_s = 0$ state. After a variable waiting time τ, the spin state is read out by a second laser pulse and fluorescence collection.

all ^{13}C spins have the same Larmor frequency[6], the oscillating fields of all spins add up. Similar to the case of parallel hyperfine interaction, the amplitude varies with the state of all ^{13}C spins, however, the frequency stays the same[7]. The presence of this alternating magnetic field can be used to detect and characterize the respective nuclear spins [11, 20, 31, 32], and even nuclear spins outside the diamond [33, 35, 69].

1.6.4. Spin lifetimes

Longitudinal spin lifetime

The Hamiltonian introduced in eq. 1.1 does not depict the whole picture. Interactions of the NV center electron spin with the diamond lattice, e.g. due to spin-orbit coupling, are neglected. At room-temperature, these couplings enable the spin-phonon interaction of the NV center spin, resulting in a longitudinal spin lifetime (i.e. the lifetime of the spin states $|m_s = -1, 0, +1\rangle$, and hence the spin expectation value in z direction $\left\langle \hat{S}_z \right\rangle = \langle\psi| \hat{S}_z |\psi\rangle$) of $T_1 \sim 5\,\mathrm{ms}$ [70] (see fig. 1.7)[8]. This behavior, as well as its influence on nuclear spins in the vicinity of the NV center is treated in section 3.

[6]Technically, the frequency can differ slightly due to magnetic field inhomogeneity or coupling to other spins.

[7]This point of view is not exactly correct, since it does not account for the quantum nature of the ^{13}C spins. This will be discussed further in chapter 4.

[8]Even though this number is quite homogeneous among different diamond crystals, the measurement thereof can differ due to charge state transitions between NV$^-$ and NV^0, as well as unwanted leakage of excitation light.

Transversal spin lifetime

The transversal spin lifetime of the NV center (i.e. the lifetime of the $|\pm x\rangle$ or $|\pm y\rangle$ states) can differ from the T_1 lifetime. By applying a $\pi/2$ pulse on the $|m_s = 0\rangle$ state of the NV center it is brought to the $|+x\rangle$ state. In the rotating frame, the state then precesses with the detuning Δ between spin Larmor frequency and MW frequency (see sec. 1.6.2). While a constant Δ during an experiment can be compensated by choosing the correct MW driving frequency, a random time-varying Δ causes the spin to precess in unforeseen ways. Noise-sources for Δ can be separated into transient and fast varying magnetic fields. Transient noise (i.e. Δ is approximately constant during one run of the experiment) causes the inhomogeneous decay of the NV center spin state on the timescale $T_2^* \sim 5\,\mu$s, mostly due to the Overhauser field due to hyperfine interaction with the ^{13}C spins in the diamond lattice. A prolongation is therefore possible by increasing the ^{12}C concentration during diamond production.
By employing echo pulse sequences (e.g. a Hahn-echo sequence [71]), the stochastic detuning during a single run of the measurement can be refocused. This can increases the homogeneous lifetime of the transversal spin state up to $T_2 = T_1/2$.

1.7. Microwave pulse sequences

In this section, microwave pulse sequences will be introduced. In order to use the NV center as a quantum sensor, it needs to be sensitive to the quantity under study, while at the same time being robust against noise. Starting with the basic sequences needed to characterize the system, more complex pulse sequences can be performed.

1.7.1. Rabi oscillations

In sec. 1.6.2, so-called π pulses were introduced. The fixed length of the pulse, according to $\tau_\pi = \frac{\pi}{\tilde{\gamma}_{\mathrm{el}} B_1^{\mathrm{amp}}}$, performs a rotation with an angle π around the x axis, therefore swapping the eigenstates of the addressed transition. Since the amplitude of the MW field is generally not known (and is usually inhomogeneous for different NV centers in the same crystal), it needs to be measured. By observing the NV center spin state, dependent on an applied MW pulse with varying length, the oscillations of the spin state between the $m_s = 0$ and $m_s = \pm 1$ spin state become visible (see fig. 1.8). By choosing the MW pulse duration to be half the oscillation period, a π pulse can be performed. Consequently, the duration for a $\pi/2$ pulse is $\tau_{\pi/2} = \tau_\pi/2$.

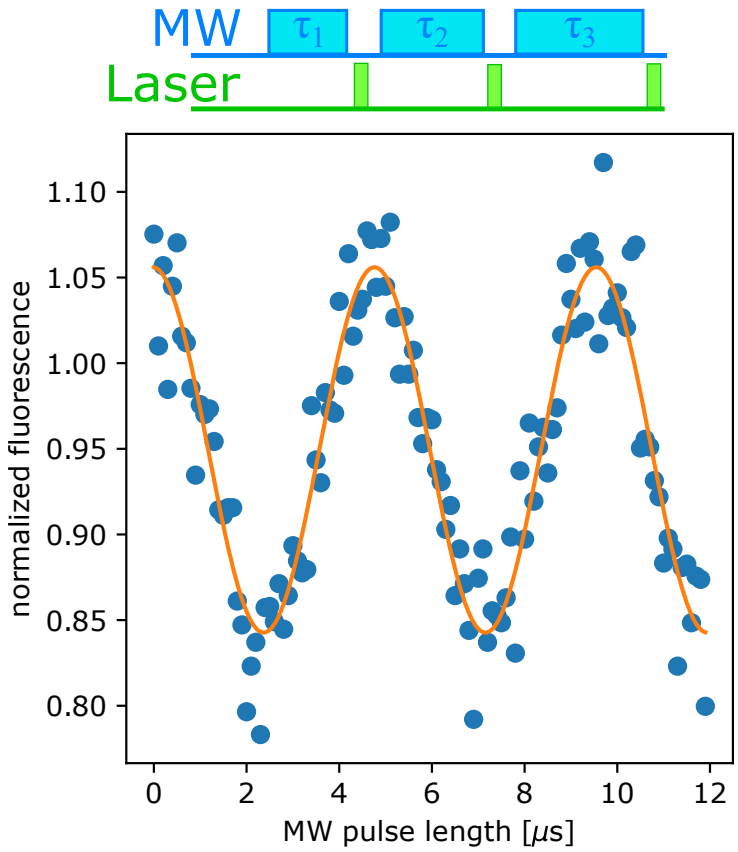

Figure 1.8.: Rabi oscillations of an NV center electron spin. In between two green readout laser pulses, a MW pulse with varying duration is applied on resonance to the $m_s = 0$ to $m_s = -1$ (or $m_s = +1$) transition. By observing the fluorescence of the subsequent laser pulse in dependence on the duration, oscillations of the spin state become visible. The Rabi frequency can be fitted to be 209 kHz, resulting in the length of a π pulse of $\tau_\pi = 2.39\,\mu$s

1.7.2. Microwave square pulse

A MW square pulse is defined as a pulse, where the envelope of the oscillating field has rectangular shape, i.e. the pulse is switched on and off within an infinitesimal small time. In eq. 1.5, the Hamiltonian of the NV center in the rotating frame of the MW signal was introduced. Without detuning between MW frequency and transition frequency, i.e. $\Delta = 0$, the Rabi oscillations from section 1.7.1 are induced. For small detunings ($\Delta \leq \Omega$), however, the spin state is also altered. Rabi oscillations occur with an effective oscillation frequency of

$$\Omega_{\text{eff}} = \sqrt{\Omega^2 + \Delta^2}. \tag{1.14}$$

The amplitude of the oscillation is reduced to

$$A = A_0 \left(\Omega/\omega_{\text{eff}}\right)^2 = \frac{A_0}{1 + \left(\Delta/\Omega\right)^2}, \tag{1.15}$$

with the amplitude A_0 of resonant Rabi oscillations, and therefore the full contrast between the spin states $m_s = 0$ and $m_s = \pm 1$. The change of spin state by a rectangular MW pulse has the shape

$$S(\Delta, \tau) = A_0 \left(\Omega/\omega_{\text{eff}}\right)^2 \cdot \sin\left(\frac{\Omega_{\text{eff}}\tau}{2}\right), \tag{1.16}$$

with the fixed pulse length τ. This explains the sinc-like shape of the ODMR spectra from figures. 1.5 and 1.6.

1.7.3. Ramsey interferometry

Previously, magnetic fields could be measured by employing square pulses, and observing the position of the ODMR signal (fig. 1.5). Another possibility, explained in this section, are Ramsey measurements, where oscillations in the spin state due to a detuning between transition frequency and MW frequency are induced. First, the electron spin is initialized to its $m_s = 0$ state by green laser excitation. The spin is then brought to a superposition state by a MW $\pi/2$ pulse[9].

$$|\psi\rangle = \frac{1}{\sqrt{2}} \left(|0\rangle + |1\rangle\right) = |+x\rangle \,. \tag{1.17}$$

[9]The spin states to which the MW radiation is resonant will be $m_s = 0$ and $m_s = 1$. The same is however true for $m_s = -1$

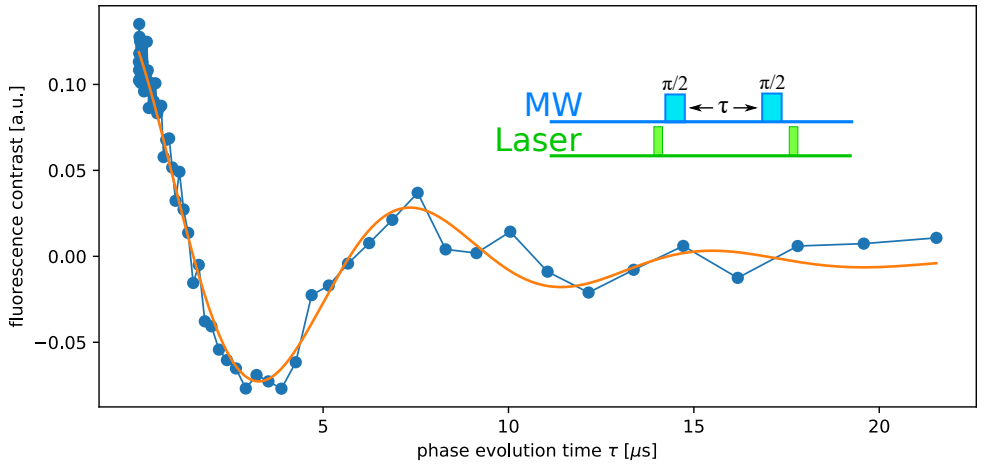

Figure 1.9.: Ramsey oscillations of an NV center electron spin. The pulse sequence consists of an initialization laser pulse, two MW $\pi/2$ pulses separated by a phase evolution time τ, and subsequent readout, and is shown inline. Due to a detuning between the MW and transition frequency, the spin expectation value along its z axis oscillates with the detuning. By fitting, the detuning can be determined to be $\Delta = 122.65\,\text{kHz}$, and the decay time $T_2^* = 5.21\,\mu\text{s}$

This state is an eigenstate of the $\hat{\sigma}_x$ operator. As can be seen from eq. 1.5, the spin then rotates around the z axis with frequency Δ. After a time τ, the spin is in the state

$$|\psi\rangle(\tau) = \frac{1}{\sqrt{2}}\left(|0\rangle + e^{i\Delta\cdot\tau}|1\rangle\right). \tag{1.18}$$

A second $\pi/2$ pulse then rotates the state again around the y axis, transforming the spin polarization along the x axis, to a polarization along z, where it can be read out. The expectation value $\langle\hat{\sigma}_z\rangle$ then reads [72]

$$\langle\hat{\sigma}_z\rangle = -1\cdot\cos(\Delta\cdot\tau) + 1. \tag{1.19}$$

A Ramsey measurement on an NV center can be seen in fig. 1.9. Here, the detuning of $\Delta = 122.65\,\text{kHz}$ is due to a deliberate detuning of the applied MW frequency. The inhomogeneous transversal lifetime amounts to $T_2^* = 5.21\,\mu\text{s}$.

Ramsey interferometry is not only dependent on a constant detuning Δ, but can also show signals due to time-dependent magnetic fields. This can be further understood, by looking at the spectral filter function of the sequence [73]. It can be obtained by Fourier transformation of the Filter function in the time-domain. Since the NV center is insensitive to magnetic fields before the first $\pi/2$ pulse, as well as after the second $\pi/2$ pulse, the filter function in the time domain equals $F(t) = 1$ for $0 < t < \tau$, and $F(t) = 0$

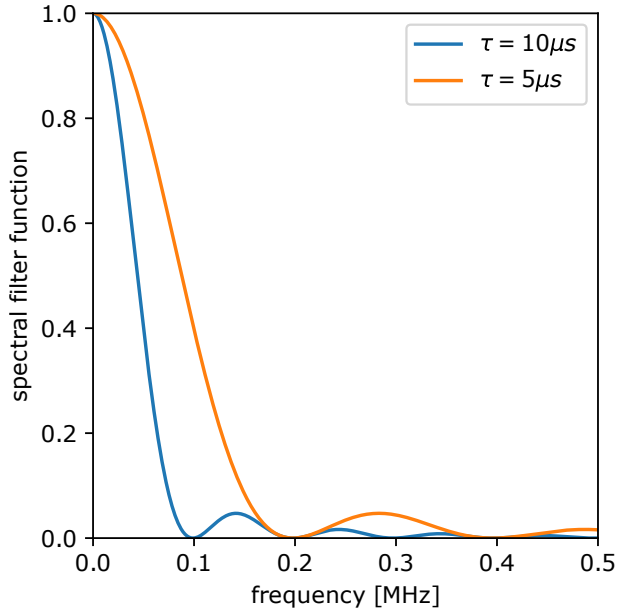

Figure 1.10.: Spectral filter function for a Ramsey sequence with two different values for τ. It is obtained by Fourier transformation of the time-domain filter function of the Ramsey sequence. Since the NV center is only sensitive to magnetic fields between the two $\pi/2$ pulses, the time-domain filter function is $F(t) = 1$ for $0 < t < \tau$, and $F(t) = 0$ in any other case. The Fourier transformation then yields the spectral filter function $F^*(f) = \frac{2\sin^2(\pi f t)}{\tau(\pi f)^2}$.

in any other case[10]. The Fourier transformed filter function in the time domain then reads

$$F^*(f) = \left| \int_{-\infty}^{\infty} e^{-2\pi i f t} F(t) \right| \tag{1.20}$$

$$= \frac{2\sin^2(\pi f t)}{\tau(\pi f)^2}, \tag{1.21}$$

with the evolution time τ between the two $\pi/2$ pulses. The resulting filter function can be seen in fig. 1.10. The additional maxima in the filter function in fig. 1.10 occur, when $\tau \mod (1/f) = 1/2$.

1.7.4. Hahn echo

In order to detect AC magnetic fields, two things need to be changed from the Ramsey sequence filter function. The sensitivity to noise at $f = 0$ needs to be removed, while the filter function at a desired frequency needs to be increased. In the year 1950, Erwin Hahn published his work on spin echoes [71]. Hereby, an inhomogeneously dephasing spin ensemble could be refocused by applying a π pulse after a certain phase evolution time, thus increasing the coherence time. For the case of an NV center electron spin, this will be demonstrated as follows. The spin is, similar to the Ramsey sequence, rotated to its

[10]Strictly, this is only true for MW pulses of negligible duration

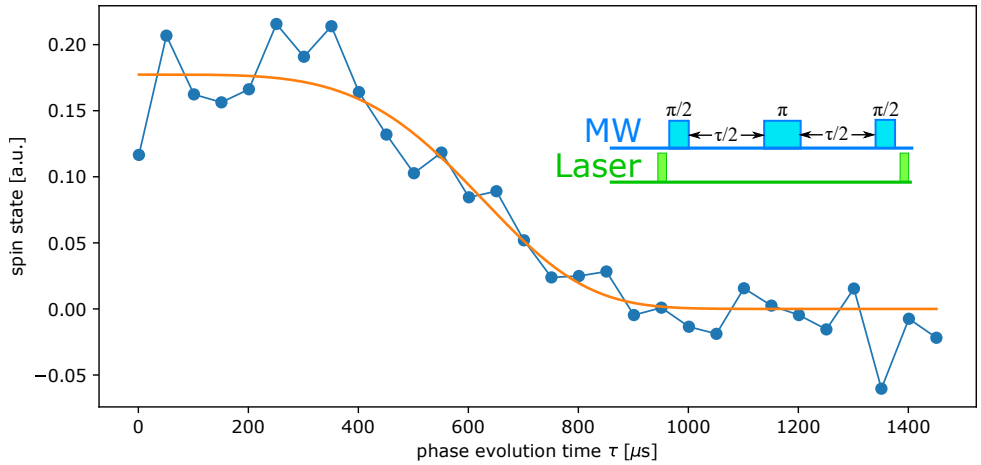

Figure 1.11.: Hahn echo measurement on an NV center electron spin. The sequence consists of two $\pi/2$ pulses, separated by time τ. After a free evolution time $\tau/2$, a refocusing π pulse is introduced. The fit assumes homogeneous dephasing on a timescale of $T_2 = 667\,\mu$s.

$|{+x}\rangle$ state by a $\pi/2$ pulse, followed by a free evolution time $\tau/2$. Afterwards, the spin is in the state

$$|\psi\rangle = \frac{1}{\sqrt{2}}\left(|0\rangle + e^{i\Delta\tau/2}\,|1\rangle\right). \tag{1.22}$$

The following refocusing π pulse swaps the $|0\rangle$ and $|1\rangle$ states, resulting in

$$|\psi\rangle = \frac{1}{\sqrt{2}}\left(|1\rangle + e^{i\Delta\tau/2}\,|0\rangle\right). \tag{1.23}$$

The second phase evolution again adds a phase onto the $|1\rangle$ state

$$|\psi\rangle = \frac{1}{\sqrt{2}}\left(e^{i\Delta\tau/2}\,|1\rangle + e^{i\Delta\tau/2}\,|0\rangle\right). \tag{1.24}$$

Since quantum mechanical states are symmetric under the multiplication of a global phase, this state is the same as after the first $\pi/2$ pulse

$$|\psi\rangle = \frac{1}{\sqrt{2}}\left(e^{i\Delta\tau/2}\,|1\rangle + e^{i\Delta\tau/2}\,|0\rangle\right) \tag{1.25}$$

$$= \frac{1}{\sqrt{2}}\left(|1\rangle + |0\rangle\right) \tag{1.26}$$

$$= |{+x}\rangle\,. \tag{1.27}$$

The Hahn echo sequence therefore refocuses constant detunings Δ. In fig. 1.11, an echo measurement is performed on an NV center electron spin. The decay time $T_2 = 667\,\mu$s is much longer than the previously determined inhomogeneous dephasing[11].

[11]The function used for the fit is a super-gaussian function [74, 75].

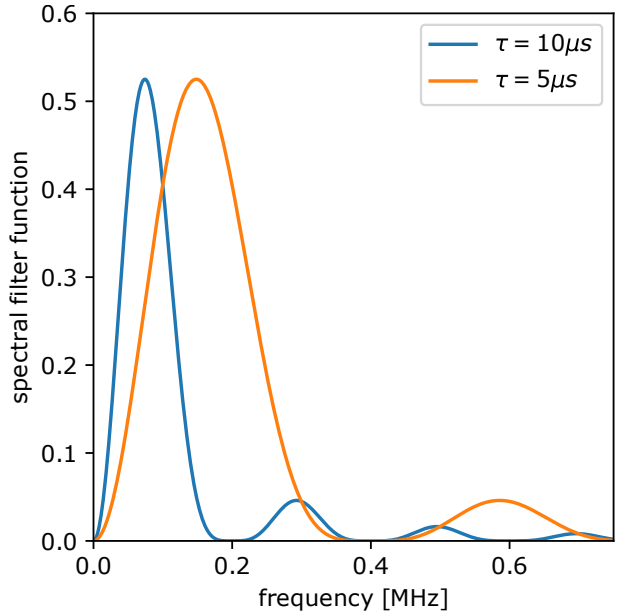

Figure 1.12.: Spectral filter function for a Hahn echo sequence with two different values for τ. The sequence is most sensitive for noise at a frequency near $f = 1/(\tau)$.

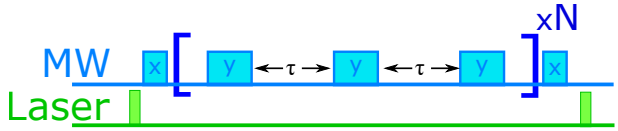

Figure 1.13.: CPMG sequence for improved dynamical decoupling. Instead of one π pulse, as for the Hahn echo, the spin is rotated three times around the y axis. The sequence can be repeated N times, to form the CPMG-N sequence.

The spectral filter function of the Hahn echo sequence can be obtained similar to sec. 1.7.3. The filter function in the time domain is $F = 1$ for $0 < t < \tau/2$, and after the refocusing pulse inverted to $F = -1$ for $\tau/2 < t < \tau$. By Fourier transforming, the spectral filter functions are obtained, see fig. 1.12. As can be seen, constant noise is efficiently cancelled out, while increasing sensitivity for oscillating fields near a frequency $f = 1/\tau$ [12]. Since the maximum of the spectral filter function can be changed by varying τ, a spectrum of environmental noise can be recorded [76].

1.7.5. Dynamical decoupling sequences

After the introduction of the Hahn echo sequence in 1950, it did not take long until scientists were working on sequences with better performance. In 1954, Carr and Purcell extended the simple echo sequence to incorporate more than one refocusing π pulse [77]. Furthermore Meiboom and Gill applied the refocusing pulses not along the y, but along the x axis [78]. Together, the Carr-Purcell-Meiboom-Gill (CPMG) sequence was born.

[12] Note that it is not exactly $1/\tau$. For echo sequences employing N number of π pulses, the resonance nears $f = (N + 1)/(2\tau)$

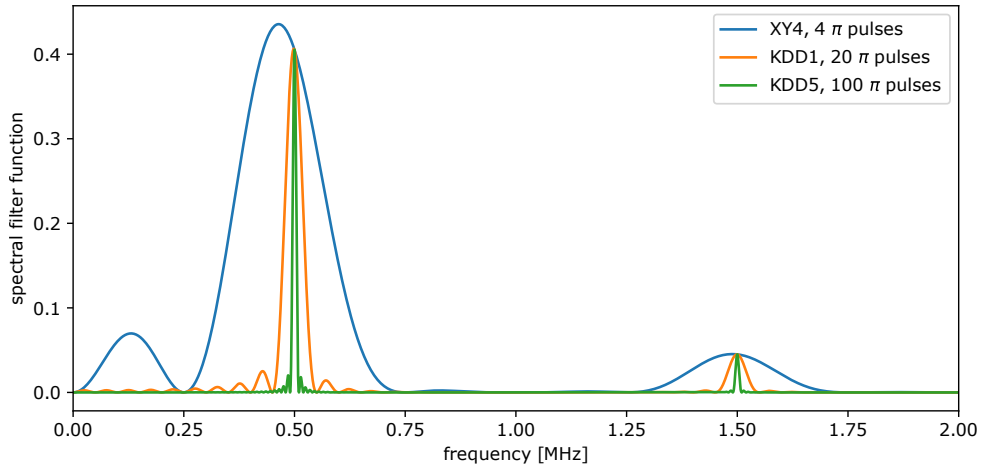

Figure 1.14.: Spectral filter functions for XY4, KDD1 and KDD5 dynamical decoupling sequences. The inter-pulse spacing τ was set to $\tau = 1\,\mu$s.

The sequence can be seen in fig:1.13(a). Due to the large number of pulses that are applied, small pulse errors e.g. in frequency or amplitude tend to sum up [79]. Therefore, more sophisticated dynamical decoupling (DD) sequences were created, for example the XY4 [80], XY8 and XY16 [81] or KDD (short for Knill dynamical decoupling) sequence [79, 82]. The difference between these sequences is the number of refocusing π pulses, as well as the axis around which the spin is rotated. For XY4, the π rotation pattern is (x)-(y)-(x)-(y), hence the name. An XY8 sequence is formed by performing two XY4 sequences consecutively, with the second one reversed, i.e. (x)-(y)-(x)-(y)-(y)-(x)-(y)-(x). Due to the use of an AWG for signal generation, arbitrary phases can be added to the MW signal, thus enabling the rotation of the spin around arbitrary axes. In this case, the Knill dynamical decoupling (KDD) performs best under noisy conditions [79]. It consists of 20 π pulses with the pattern (π/6)-(0)-(π/2)-(0)-(π/6)-(4π/6)-(π/2)-(π)-(π/2)-(4π/6)-(π/6)-(0)-(π/2)-(0)-(π/6)-(4π/6)-(π/2)-(π)-(π/2)-(4π/6), with the number denoting the angle of the axis of rotation, shifted from the x axis (see fig. 4.6).
The spectral filter functions are independent on the angle of rotation of the π pulses, and only depend on their number. By repetitively inverting the filter function in the time domain, and subsequent Fourier transformation, the spectral filter function can be obtained similar to sec. 1.7.4. In fig. 1.14, the spectral filter functions are plotted for the XY4, KDD1 and KDD5 sequence. As can be seen, the width of the main resonance decreases with the number of pulses [83], according to

$$\Delta f = 1/(N\tau). \tag{1.28}$$

1.7.6. Correlation spectroscopy

The hitherto introduced dynamical decoupling sequences can be used for the detection of oscillating magnetic fields. The frequency resolution if given by $\Delta f = 1/(N\tau)$, where

Figure 1.15.: Correlation spectroscopy measurement sequence. Two XY4 DD sequences are separated by a free evolution time T. Since the quantum phase accumulated during the DD sequence depends on the relative phase of the signal to the DD sequence (see fig. 4.2), the quantum phase in the second XY4 sequence oscillates with the frequency of the AC magnetic field. During the free evolution time, the x component of the NV center spin state is rotated to the quantization axis, where is persists for the longitudinal relaxation time T_1.

N is the number of π pulses, and τ the inter-pulse spacing. It is therefore limited by the homogeneous transversal relaxation time T_2 to $\Delta f_{\max} = 1/T_2$. This limit can be overcome by correlation spectroscopy sequences [84–86]. Here, the sequence is divided in three parts: Two DD sequences, in resonance with an oscillating magnetic field, and an in-between free evolution time. During this, the quantum phase accumulated during the DD sequence is transferred onto the polarization of the NV center electron spin, where it decays on a timescale $T_1 > T_2$. The second DD sequence then effectively correlates the oscillating signal at a later time to the signal during the first DD. By observing the final NV center spin state with varying free evolution time, the time-domain signal becomes visible[13]. The sequence can be seen in fig. 1.15.

The filter function for this sequence can be again calculated similar to the previous chapter. For the dynamical decoupling part, the time-domain filter function oscillates between +1 and -1, while it is set to zero during free evolution. The Fourier transformed spectral filter function can be seen in fig. 1.16. As can be seen, the slight variations of the free evolution time T shift the peaks of sensitivity inside the encapsulating filter set by the XY4 DD sequence. The width of the peaks corresponding to the correlation spectroscopy scheme is given by $\Delta f = 1/(T)$, which is ultimately limited by $\Delta f_{\max} = 1/T_1$. It should be noted, that since only the x component of the superposition state of the spin is rotated to the polarization axis, part of the information accumulated is lost, and therefore the signal reduced.

This technique motivated the formation of the hybrid spin register in this work (see chapter 3).

1.7.7. On the detection of nuclear spins

In classical NMR spectroscopy, a small thermal polarization ($P = e^{-E_{\text{Zeeman}}/k_{\text{B}}T} \approx 10^{-5}$, at room-temperature and 1 T magnetic field) is enough to generate a measurable signal. On the other side, when only a small number of spins are detected, this results in negligible

[13]The mechanism behind this technique is applied and explained further in chapters 3 and 4.

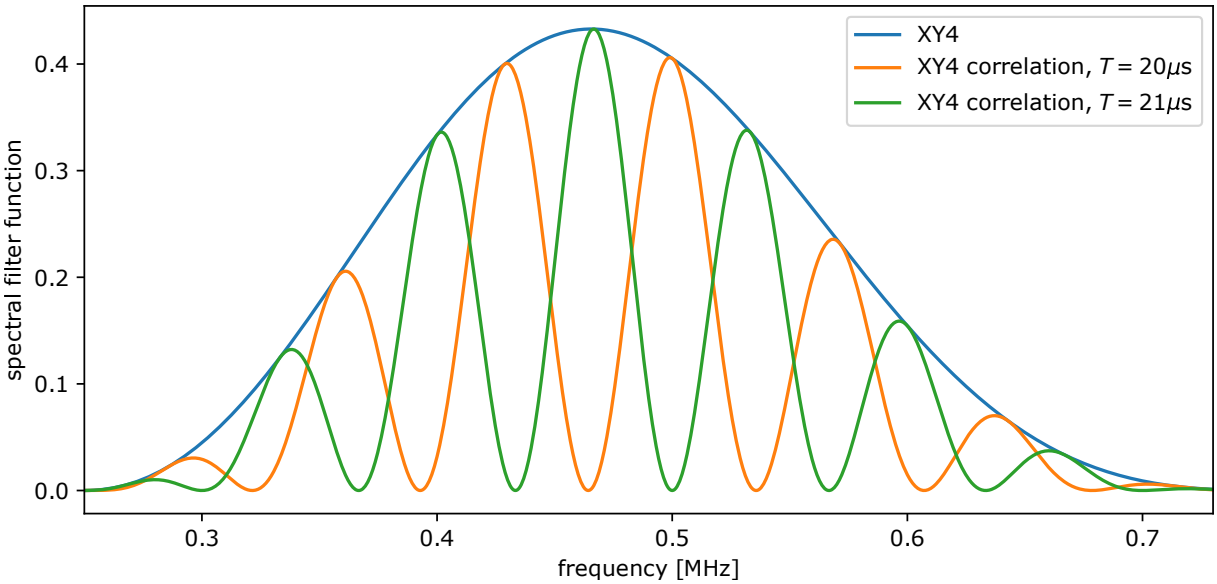

Figure 1.16.: Spectral filter function of the correlation spectroscopy sequence. The DD sequences used for calculation are the same as in fig. 1.14, the bare XY4 sequence is shown as comparison. The two lines corresponding to the correlation spectroscopy were calculated by assuming one iteration of XY4 DD prior and after the free evolution time. By varying the time T, the spectral filter function can be swept across the encapsulating filter function of the DD sequence.

polarization of the nuclear spin bath. However, for small number of spins, the deviation of the momentary polarization of nuclear spins might strongly differ from the case of perfect cancellation. In fact, the polarization due to stochastic alignment of the spin ensemble is $P_\mathrm{s} = \frac{\sqrt{N}}{N}$, which is e.g. 10^3 for 10^6 nuclear spins, and therefore much larger than the thermal polarization [87].

As explained in sec. 1.6.3, the influence that nuclear spins inside (and outside) the diamond have on the NV center is twofold. The parallel hyperfine interaction terms in the Hamiltonian are of the form $\hat{S}_z A_{zz} \hat{I}_z$. These terms slightly shift the resonance of the NV center electron spin, depending on the spin states of the nuclear spins. For a completely unpolarized spin bath, the interactions cancel each other out. Since, however, the spin bath only averages to zero when averaging over time, one single measurement run is still influenced by the momentary stochastic polarization of the spin bath. Ramsey sequences can in principle reveal the signal due to nuclear spins, however, since it is unspecific to the nuclear spin species (or other sources of magnetic noise), it is not the first choice.

In contrast to magnetic noise, the frequency shift due to nuclear spins can be altered. Similar to MW radiation changing the spin state of the NV center electron spin, RF pulses can alter the nuclear spin states. Therefore, an easy way to detect nuclear spins is by performing a Hahn echo sequence on the NV center electron spin, and simultaneously flipping electron and nuclear spins with the refocusing π pulse. Since this inverts the

nuclear spin polarization, the phase refocusing effect of the Hahn echo does not apply for the flipped nuclear spins. This is in principle the electron nuclear double resonance (ENDOR) sequence known from ESR [88].

The second class of terms from sec. 1.6.3, are terms of the shape $\hat{S}_z A_{zx} \hat{I}_{(x)}$[14]. Since a nuclear spin polarized along its x or y axis rotates about the z axis with its Larmor frequency, it creates an oscillating shift of the NV center transition frequency. In this section, DD sequences were introduced, that decouple the electron spin from noise, but are susceptible to noise at a very well defined frequency. By tuning the parameters of these sequence, the signal from nuclear spins can be observed and characterized [20, 31–33, 35, 36, 69].

In this work, both techniques are used to detect and characterize very weakly coupled nuclear spins inside the diamond lattice, and explore the limits in terms of frequency resolution of a nanoscale NV center NMR ssensor.

1.8. A nuclear spin memory for readout enhancement

The optical spin initialization of the NV center was introduced in sec. 1.4.1. Summarizing, the NV center is read out by a short (300 ns) green laser pulse. Although the fluorescence intensity of NV centers is quite high, this results in only around 0.1 photons emitted per readout. The fluorescence contrast between the different spin states is 30%, i.e. 0.1 photons for $m_s = 0$, and 0.07 photons for $m_s = \pm 1$. Ergo, in order to distinguish between two spin states, the experiment needs to be repeated, until the SNR exceeds the photon shot noise

$$\mathrm{SNR} = \frac{\text{signal}}{\text{noise}} = \frac{0.3 \cdot N \cdot 0.1}{\sqrt{N \cdot 0.1}}, \tag{1.29}$$

with the number of readouts N. So in order to reach a SNR of 1, around 110 readouts of the NV center are needed. The SNR can also be expressed as a spin state sensitivity by substituting the number of measurements with the total duration $T = N\tau$

$$\mathrm{SNR} = \frac{0.3 \cdot T/\tau \cdot 0.1}{\sqrt{T/\tau \cdot 0.1}} = 0.3\sqrt{0.1 \cdot T/\tau} \tag{1.30}$$

$$\frac{\mathrm{SNR}}{\sqrt{T}} = 0.3\sqrt{0.1 \cdot \tau} \tag{1.31}$$

This section will briefly introduce the usage of the host nitrogen nuclear spin as a memory to enhance the readout efficiency.

As introduced in sec. 1.6.3, the Hamiltonian of the coupled NV center electron and

[14] Without loss of generality, the x axis can be set as the axis transversal to the NV center quantization axis, pointing towards the nuclear spin

nitrogen nuclear spin system is

$$\hat{H} = D\hat{S}_z^2 + B_0\tilde{\gamma}_{\mathrm{el}}\hat{S}_z \tag{1.32}$$
$$+ C_q^{\mathrm{N}}(\hat{I}_z^{\mathrm{N}})^2 + \tilde{\gamma}_{\mathrm{N}}B_0\hat{I}_z^{\mathrm{N}} \tag{1.33}$$
$$+ \left(\hat{S}_+\hat{I}_- + \hat{S}_-\hat{I}_+\right) A_\perp/2 + \hat{S}_z A_\parallel \hat{I}_z. \tag{1.34}$$

Except for the spin flip-flop term $\left(\hat{S}_+\hat{I}_- + \hat{S}_-\hat{I}_+\right) A_\perp/2$, only z components of the electron and nuclear spin operators occur. Notably, the Hamiltonian in the electronic excited state is of the same form, but with different values [15, 59]

$$D^{\mathrm{exc}} = 1.4\,\mathrm{GHz} \tag{1.35}$$
$$A_\parallel \approx 40\,\mathrm{MHz} \tag{1.36}$$
$$A_\perp \approx 40\,\mathrm{MHz}. \tag{1.37}$$

The value of the excited state quadrupole splitting $C_q^{\mathrm{N,exc}}$ is not known. Since the density of other nitrogen nuclear spins in the diamond lattice is negligible, the most dominant decay mechanism are spin flip-flops with the NV center electron spin. For electron spin transition frequencies larger than the hyperfine coupling, the flip-flop probability can be approximated as [67]

$$p_{\mathrm{ff}}(B_0) \approx \frac{4A_\perp^2}{(\tilde{\gamma}_{\mathrm{el}}B_0 - D)^2}. \tag{1.38}$$

Notably, the rate goes down quadratically when increasing the electron spin transition frequency, by applying higher magnetic fields B_0.

The readout of the nitrogen spin via the electron spin can be seen in fig. 1.17. When the amplitude of the MW field used for spin manipulation is adequately low, the ^{14}N hyperfine splitting becomes visible in the ODMR spectrum. A π pulse resonant on one of the hyperfine split transitions only flips the NV center electron spin, when the nuclear spin is in the respective state, comprising a conditional rotation (similar to a controlled NOT gate (CNOT gate)) of the electron spin. The subsequent readout of the NV center spin is strongly correlated with the nuclear spin state[15]. At low magnetic fields, however, the optical excitation of the NV center destroys the nuclear spin state, due to the larger hyperfine coupling in the excited state.

In ref. [15], Neumann et al. increased the magnetic field far beyond the level anti-crossing (LAC) of the NV center electron spin. At that point, the flip-flop rate was so low, that the nitrogen nuclear spin state persisted for several tens of milliseconds, even while repetitively reading out the electron spin. By performing the readout for ~ 1000 times,

[15] It is actually only a perfect correlation between nuclear spin state $m_i = +1$ and not $m_i = +1$. There is no information about $m_i = 0$ or $m_i = -1$

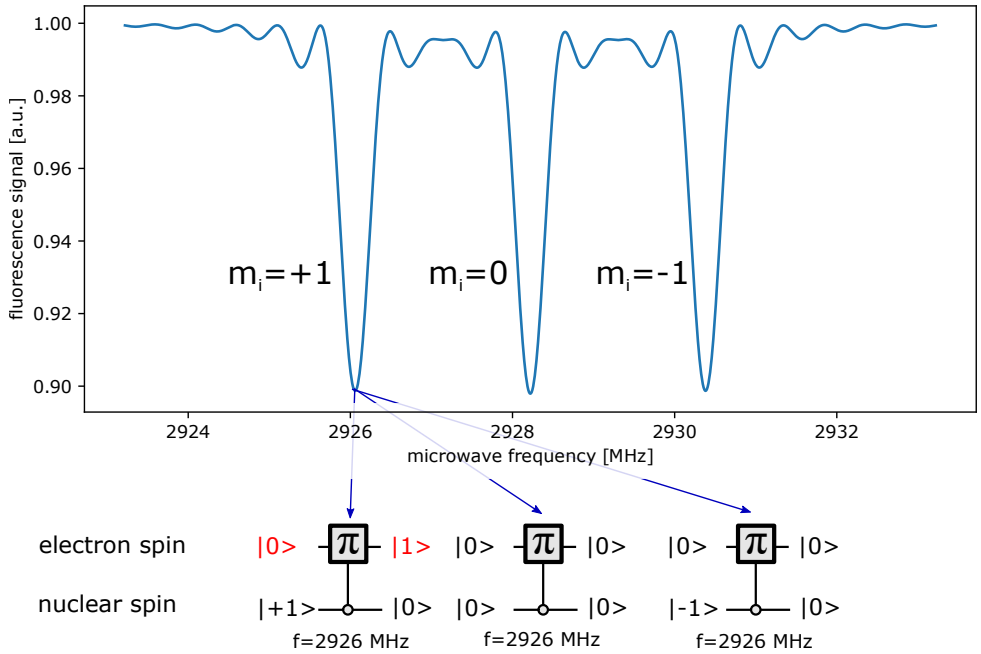

Figure 1.17.: Readout of the nitrogen nuclear spin via the NV center electron spin. An ODMR spectrum, recorded with low MW amplitude and therefore low Rabi frequencies, enables the resolution of the hyperfine splitting caused by the ^{14}N nuclear spin. By applying a MW pulse resonant on the transition belonging to the $m_i = +1$ nuclear spin state, the electron spin is flipped only when the nuclear spin is in said state (in the lower part of the figure represented by the connection of the π pulse to the nuclear spin state). For the $m_i = 0, -1$ state, nothing happens. The final electron spin state is hence perfectly correlated with the nuclear spin state. This represents a CNOT gate on the electron spin, conditional on the nuclear spin.

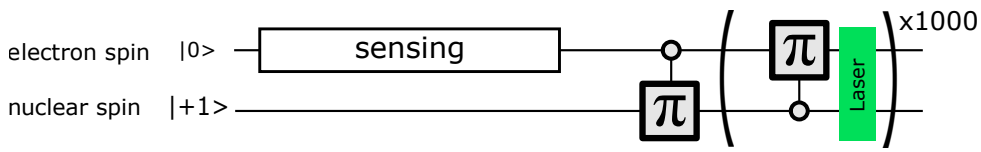

Figure 1.18.: The sequence used to implement the nitrogen nuclear spin as a readout buffer for enhanced readout of the NV center electron spin. Both spins are initialized in the beginning (the electron spin by green laser excitation, the nuclear spin by a preceding measurement and post-selection). A sensing sequence acquires a signal, and changes the electron spin state accordingly. By applying a CNOT gate on the nuclear spin, the polarization of the electron spin is transferred to the nuclear spin, which is afterwards read out in a single shot by repetitively transferring its state to the electron spin, and subsequent readout. This is repeated for around 1000 times to reach a high signal to noise ratio.

the SNR of the readout, according to eq. 1.29, is much larger than one, resulting in a single-shot readout (SSR) of the nuclear spin, with a fidelity approaching unity. The maximum information extracted can therefore not exceed 1 bit.
This technique can be used to initialize the nuclear spin and perform NMR spectroscopy on it, and furthermore allows an enhanced readout of the electron spin. By applying appropriate controlled gates, and subsequent SSR, the electron spin state can be transferred to the nuclear spin and read out in a single shot by using the nuclear spin as a readout buffer. The schematic sequence can be seen in fig. 1.18. Since the initial as well as the final nuclear spin state are known with a very high fidelity, the readout can be expressed as a spin flip probability, in principle reaching a maximum value of 1 [54]. Experimental results quantifying the readout enhancement were previously published in parts in [8].

2. Deterministic Charge State Control

When talking about the nitrogen-vacancy center (NV center) in diamond, people usually refer to the negatively charged NV^-. However, it is known that at least one other charge state, the neutral one, exists [89–91], and that conversion between NV^- and NV^0 can be done by optical excitation [51, 52, 55]. Recent works suggest, that in addition to the neutral charge state, a third positive charge state exists [1, 92]. Interestingly, when considering that the ionization of NV^- over NV^0 to NV^+ works by removing electron by electron, starting with the highest occupied single electron state, the positive charged state has no unpaired electrons, and thus no electron spin ($S = 0$).

In recent years, the NV center in conjunction with nearby coupled nuclear spins has been shown to act as a well controllable qubit register [11, 13, 18, 19, 93–96]. Due to its exceptional optical readout capabilities, even at room-temperature, the NV center electron spin can act as an ancilla qubit for selective readout and manipulation of these nuclear spins. However, the comparably short spin lifetime of the electron spin ($T_1 \approx 5\,\mathrm{ms}$) limits the spin coherence time of coupled nuclear spins. Furthermore, scaling up such a quantum registers would entail coupling several NV centers with a distance of $\sim 20\,\mathrm{nm}$ [17, 97]. This however would impede selective readout of single centers, since their distance is much smaller than the optical diffraction limit.

For phosphorous donors in silicon (Si:P), after initialization and manipulation of the phosphorous nuclear spin with help of the ancilla electron spin, ionization and thus removal of the electron spin gives rise to minute long coherence times [98–101]. The positive charge state of the NV center can potentially induce the same effect. Furthermore, NV^+ is supposed to be optically inactive [1, 92], which could enable the selective readout of a single NV center within an ensemble of closely spaced NV centers (given the possibility to manipulate the respective charge state separately).

In this chapter, we use the nitrogen nuclear spin as a charge state probe. By looking at properties of its nuclear magnetic resonance (NMR) spectrum, it is shown that the previously observed dark state is indeed the positively charged NV center. The electron spin-less nature of the charge state is shown, in conjunction with a coherence time surpassing the spin lifetime of the NV^- electron spin. The results in this chapter are published in [1, 2].

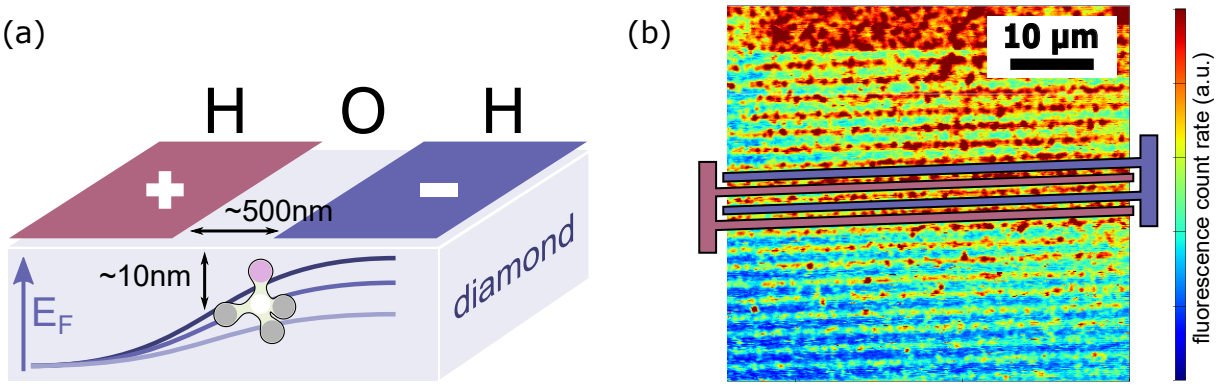

Figure 2.1.: (a) Schematic representation of two hydrogen terminated surface regions (red and blue), separated by an oxygen terminated surface. By applying a voltage between the two hydrogenated surfaces, the Fermi level at the position of an NV center positioned near the transition can effectively be changed. This effect is sketched by three different Fermi levels, for three different bias voltages. When the Fermi level crosses the charge transition level, a change in charge state is observable. (b) Confocal scan of the capacitor comprised by the two hydrogen terminated surface electrodes. The inset schematic illustrates the gate structure. Observed fluorescence is caused by NV centers implanted in the diamond. The hydrogen termination causes the NV fluorescence to quench, hence the image contrast. The interdigitated design was chosen to maximize the amount of possibly switchable NV centers.

2.1. Surface termination of diamond

The charge state of NV centers near the surface of diamond can be switched deterministically by the use of in-plane gate structures [1]. Here, two hydrogen terminated, conductive areas are separated by an oxygen terminated surface region. By applying a voltage between the two hydrogen areas, the Fermi level near the diamond surface can be shifted deterministically (see fig. 2.1(a)) For this work, a (111)-oriented diamond sample was prepared according to appendix A.1. The resulting hydrogen terminated gate electrodes, separated by an oxygen terminated surface area can be seen in figure 2.1(b). The design of the interdigitated gate electrodes was chosen in order to maximize the number of NV centers in the controllable transition region between hydrogen and oxygen termination, and therefore the number of potentially controllable NV centers. Fast control of the gate voltages was done using an arbitrary waveform generator (AWG) (see appendix A.1). Due to the non-deterministic placement of NV centers and a technical limitation on the maximum gate voltage, not every defect center can be controlled. By doing confocal scans with differing gate voltages, possible candidates can be chosen (see figure 2.2).

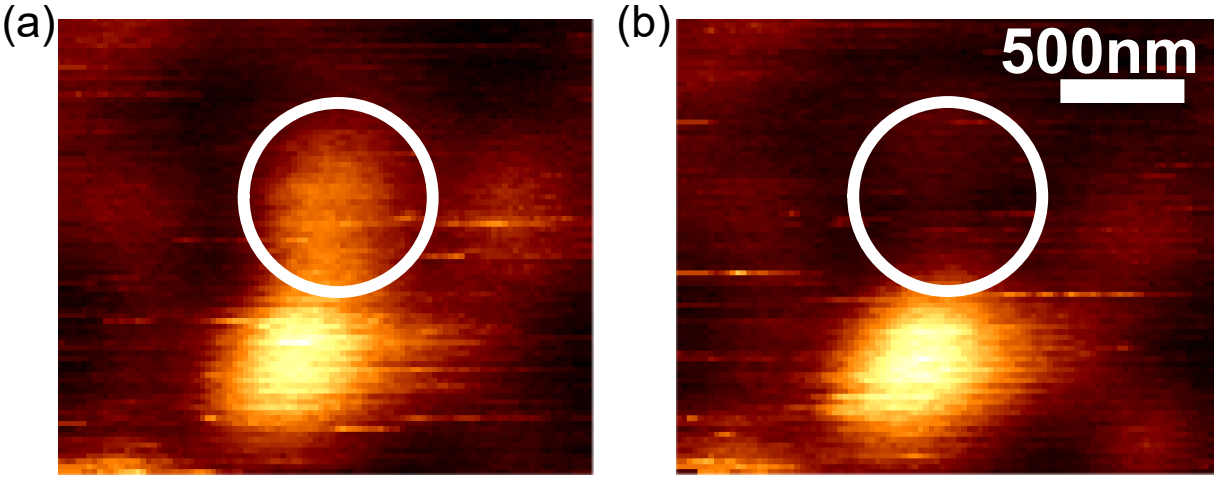

Figure 2.2.: Confocal scan of an NV center that can be manipulated by applying a gate voltage. (a) Is recorded with a constant gate voltage of $-8\,\mathrm{V}$. The visible fluorescence in the inset area can be attributed to a single NV. In (b), the gate voltage was inverted to $8\,\mathrm{V}$, completely quenching the fluorescence of the NV center. This hints to an NV center where the achievable change in Fermi level is enough to alter the charge state.

2.2. Nuclear spins as charge state probes

Up until now, most experiments investigating the charge-state behavior of NV centers rely on fluorescence spectral properties of the NV center. However, continuous optical excitation drives the defect center out of thermal equilibrium, and induces changes of the charge state [55]. In order to probe the charge state in thermal equilibrium, one needs to look at a non-optical property of the system. Every NV center electron spin is intrinsically coupled to the host nitrogen nuclear spin, either ^{14}N (Spin 1) or ^{15}N (Spin 1/2). The Hamiltonian of the coupled NV$^-$ center can be seen in eq. 1.1. In this chapter, the single nitrogen nuclear spin part $\hat{H}^{\mathrm{N}}$, as well as the coupling between electron spin and nitrogen nuclear spin $\hat{H}^{\mathrm{coupl,N}}$ will be discussed in detail. These two components amount to

$$\begin{aligned} \hat{H}^{\mathrm{N}} &= C_q^{(-)}\hat{I}_z^2 + \tilde{\gamma}_{\mathrm{n}} B_z \hat{I}_z \\ \hat{H}^{\mathrm{coupl,N}} &= A_{\parallel}\hat{S}_z\hat{I}_z + A_{\perp}/2\left(\hat{S}_+\hat{I}_- + \hat{S}_-\hat{I}_+\right) \end{aligned} \tag{2.1}$$

with the reduced gyromagnetic ratio $\tilde{\gamma}_{\mathrm{n}}$ of the nuclear spin, the external magnetic field along the NV center symmetry axis B_z, the nuclear spin quadrupole splitting parameter $C_q^{(-)}$(only for ^{14}N), the parallel and perpendicular hyperfine interaction $A_{\parallel}$ and $A_{\perp}$. The values are summarized in table A.1. For the case of NV^0, the electronic part of the Hamiltonian consists of a spin 1/2, which removes the zero-field splitting parameter. Furthermore, the quadrupole splitting, which depends on the gradient of the electric field produced by the electron at the place of the nuclear spin, changes [54]. The hyperfine

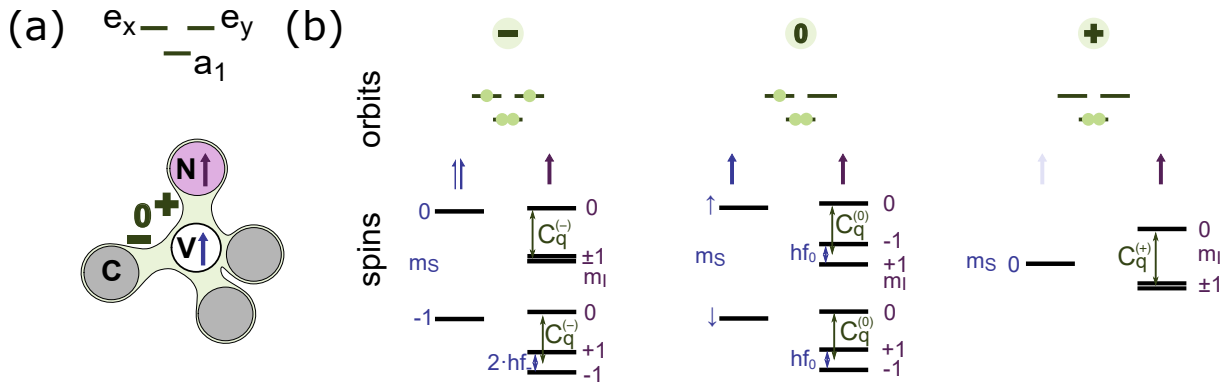

Figure 2.3.: Sketched ^{14}N NMR transitions depending on the charge state. (a) Schematically shows the three electron orbitals of interest, a_1, e_x and e_y, as well as the wave-function inside the diamond. In (b), the occupation of the electron orbitals for the three different charge states is shown. Since the number of unpaired electrons changes, so does the overall electronic spin. The ^{14}N nuclear spin level scheme is shown below. The charge state influences the energy levels by two different mechanisms: The hyperfine splitting (hf_-, hf_0), as well as the quadrupole splitting ($C_q^{(-)}$, $C_q^{(0)}$, $C_q^{(+)}$). Hence, a ^{14}N NMR spectrum can be used as a charge state fingerprint. Note, that for ^{15}N there is no quardrupole splitting, and therefore only the hyperfine coupling changes between charge states. In all level schemes, the Zeeman splitting was neglected.

coupling parameters also change due to different electronic configuration [54]. The resulting NMR energy levels can be seen in figure 2.3, and are summarized for an applied magnetic field of 470 mT in table A.2 in the appendix A.2. When we consider removing electrons when transitioning from NV$^-$ to NV^0, we expect the NV^0 ground state to be $S = 1/2$ (as was shown experimentally [102]). Further removal of an electron, creating the NV$^+$ charge state, is expected to produce an electron spin-less $S = 0$ ground state.

2.2.1. NMR charge state measurements

To deduce the charge state of the NV center we start off by initializing the nitrogen nuclear spin state by a single-shot readout (SSR) [15], facilitated by the NV center in its negative charge state. Afterwards, the charge state is altered by changing the gate voltage. A radio frequency (RF) pulse then rotates the nitrogen nuclear spin state, if the applied RF frequency and the NMR transition frequency (and thus the charge state) coincide. Afterwards, the gate voltage is reverted, and the nitrogen nuclear spin again read out via SSR. The measured probability to detect a different spin state before and after the manipulation can be used to calculate the charge state occupation probability[1]. The measurement scheme is shown in figure 2.4.

[1]For this calculation, the fidelities of the RF pulses were assumed to be 1.

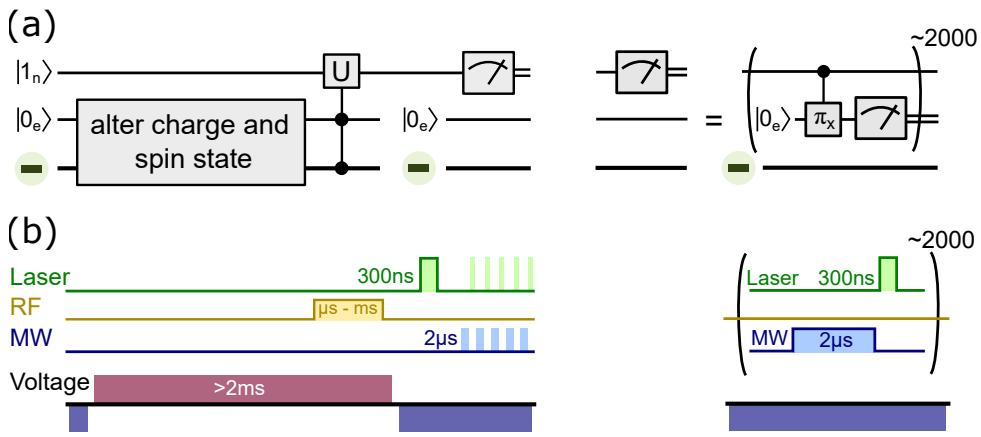

Figure 2.4.: Measurement scheme for measuring the NV center charge state properties via single-shot NMR of the nitrogen nuclear spin. (a) shows the scheme as a generalized wire diagram. After initialization of the electron and nuclear spin state (which happens in the negative charge state), some operation changes the spin and/or charge state (e.g. change in gate voltage). The actual detection of the state happens by the gate U, which depends on the electron spin and the charge state. Afterwards, the nitrogen nuclear spin state (and thus the changes due to U) are read out via SSR, which is shown on the right side. (b) is the pulse scheme of the actual experiment. The blue and red part of the gate voltage belong to the NV^- and the charge state under probe, respectively. The gate U is implemented via RF radiation with differing frequency and duration. SSR of the nuclear spin is done by alternating laser and MW pulses.

2.3. Observing charge state transitions in ^{15}NV

To circumvent the lack of knowledge about the ^{14}N quadrupole splitting for NV$^+$, we start off by using an implanted NV center with ^{15}N nuclear spin. The NMR signal with the NV center being initialized into the $m_s = 0$ state can be seen in figure 2.5(a). Furthermore, the signal corresponding to the NV^0 charge state can also be seen, due to the insufficient initialization into NV$^-$ by green excitation [54, 55]. By varying the length of the RF pulse with fixed frequency, one can see the Rabi oscillations of the ^{15}N spin, for the NV$^-$ charge state. Setting the pulse length to induce a rotation angle of π maximizes the visibility of the experiment. Due to the short electron spin lifetimes, this is not possible for NV^0 [54]. Here, the nitrogen nuclear spin can only be manipulated towards a mixed state. We fix the RF pulse frequency and duration to induce a π pulse on the nitrogen spin for NV$^-$ charge, and $m_s = 0$ spin state. The resulting spin flip probability can be used to calculate a charge state witness W_- (or W_0, for the neutral charge state).

$$W_- = (\text{amplitude} - \text{baseline})/(1 - 2 \cdot \text{baseline}) \tag{2.2}$$

$$W_0 = 2 \cdot (\text{amplitude} - \text{baseline})/(1 - 2 \cdot \text{baseline}) \tag{2.3}$$

Slightly increasing the gate voltage during the manipulation causes W_- to decrease at around $-4\,\text{V}$, while simultaneously increasing W_0 (see figure 2.5(c)). After further increasing the bias voltage, at around $8\,\text{V}$ W_- increases again, with a simultaneous decrease of W_0. Since we probe the NV$^-$ NMR transition with electron spin in $m_s = 0$ for W_-, this can be attributed to either a reappearance of NV$^-$, or hint towards a third charge state without electron spin.

2.3.1. Investigating the transition dynamics

The low value of W_- in figure 2.5 at a gate voltage of $8\,\text{V}$ hints towards a transition dynamic slower than the measurement time. To visualize the dynamics, we insert a waiting time between changing the gate voltage and probing the charge state via an NV$^-$ selective RF pulse. The experimental results (see figure 2.6) shows a transition time of $(0.54 \pm 0.08)\,\text{ms}$. Due to this fact, every measurement investigating the positive charge state (except the voltage series measurement in figure 2.5) includes a $2\,\text{ms}$ waiting time after changing the gate voltage, to complete the charge state transition.

2.3.2. Hyperfine enhancement: Proof for a spin-less charge state

The previous hints towards a positive charged NV$^+$ charge state are based on nuclear spin rotations selective on a $m_s = 0$ electron spin state (since we expect NV$^+$ to be $S = 0$). Similar to the case of NV$^-$, this rotation is still induced for any integer number electron

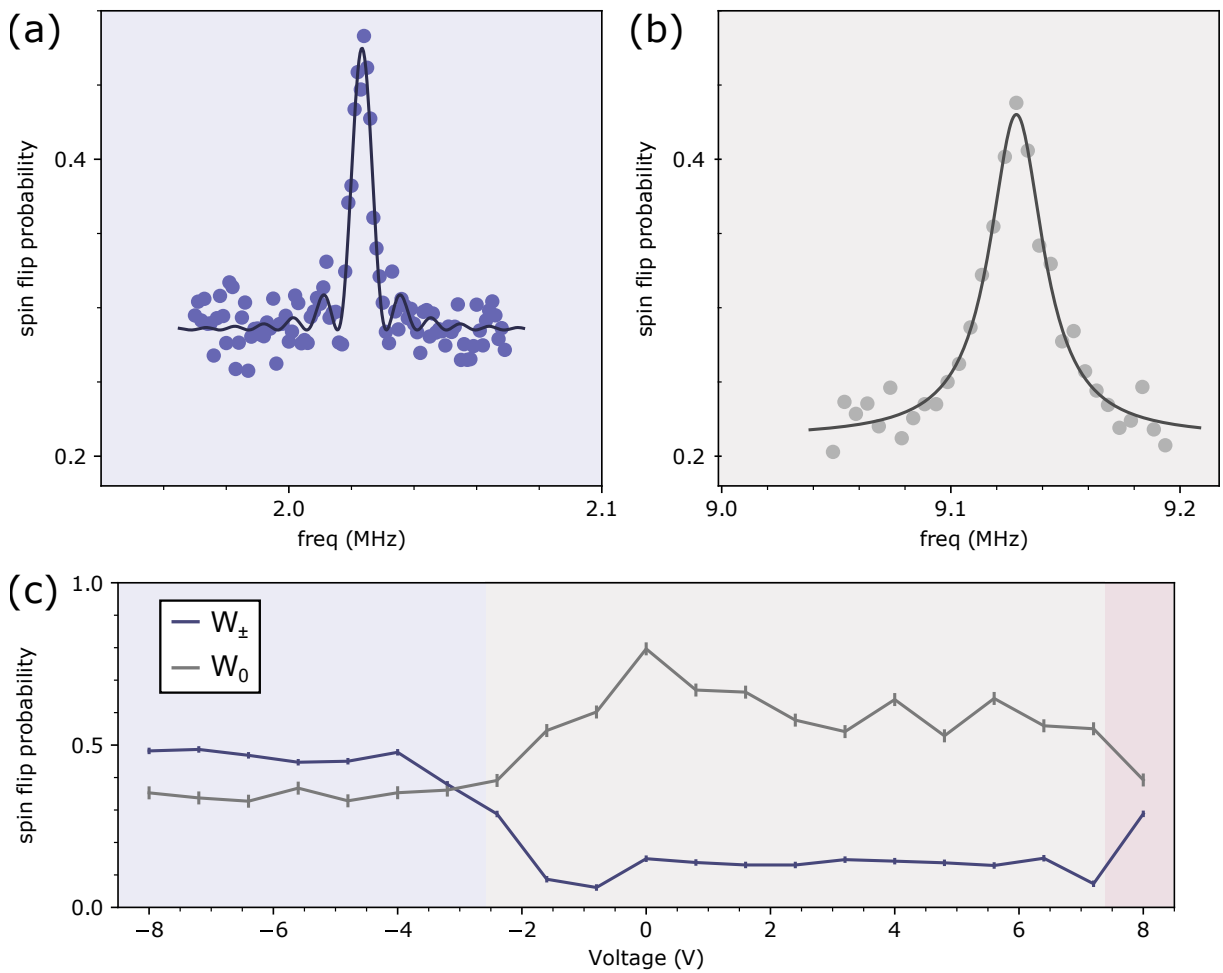

Figure 2.5.: In (a), the ^{15}N spectrum, for the electron spin state $m_s = 0$ is shown. The measurement scheme can be seen in fig. 2.4(a), with the gate U being a nominal rotation with an angle π. The y-axis is the ^{15}N nuclear spin flip probability, as explained in sec. 1.8. The peak height can be used to calculate the charge state witness W_- according to eq. 2.2. The measurement scheme can be seen in fig. 2.4(a), when the gate U is a nominal rotation with an angle π around the x-axis. The gate voltage in this experiment was kept constant at $-8\,\mathrm{V}$. For (b), the gate voltage was changed during the gate U. Since the concomitant change in Fermi level changes the charge state, the gate U is resonant at a different frequency, corresponding to the neutral charge state. In (c), the charge state witnesses that can be calculated from the peak amplitudes from (a) and (b), are measured in dependence on the gate voltage during the gate U. The transition from NV$^-$ to NV^0 can be seen at a voltage of around $-3\,\mathrm{V}$ (denoted by the faint background colors). At $8\,\mathrm{V}$, the charge state witness W_- increases again, which might be attributed to the positive charge state (since the ^{15}N transition frequency is the same for NV$^-$ with $m_s = 0$ and NV$^+$ with $S = 0$).

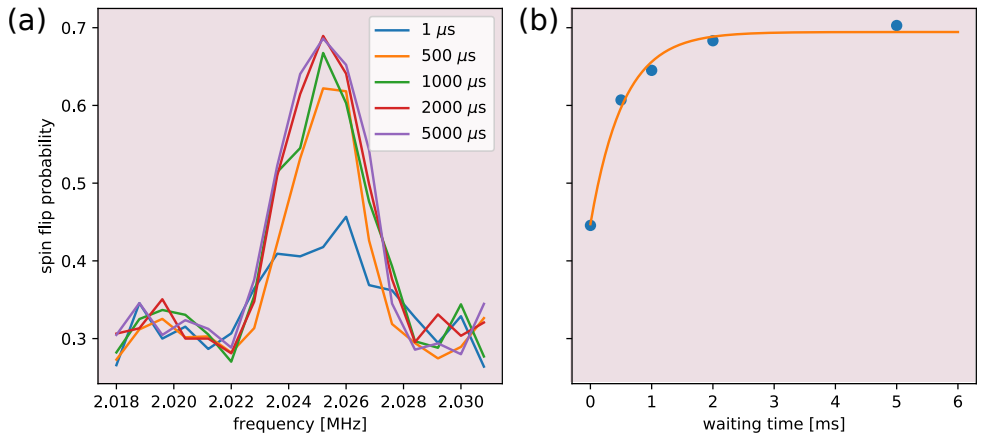

Figure 2.6.: The measurements in (a) were performed the same way as in fig. 2.5, at a gate voltage of 8 V. The waiting time between the change in gate voltage and the gate U was varied. It can be seen, that it takes a few milliseconds for the charge state to change. In (b), the peak positions of the spectra from (a) are plotted over the waiting time, and fitted with an exponential decay. The observed decay time is (0.54 ± 0.08) ms. Faint background colors denote the applied gate voltage, see fig. 2.5(c)

.

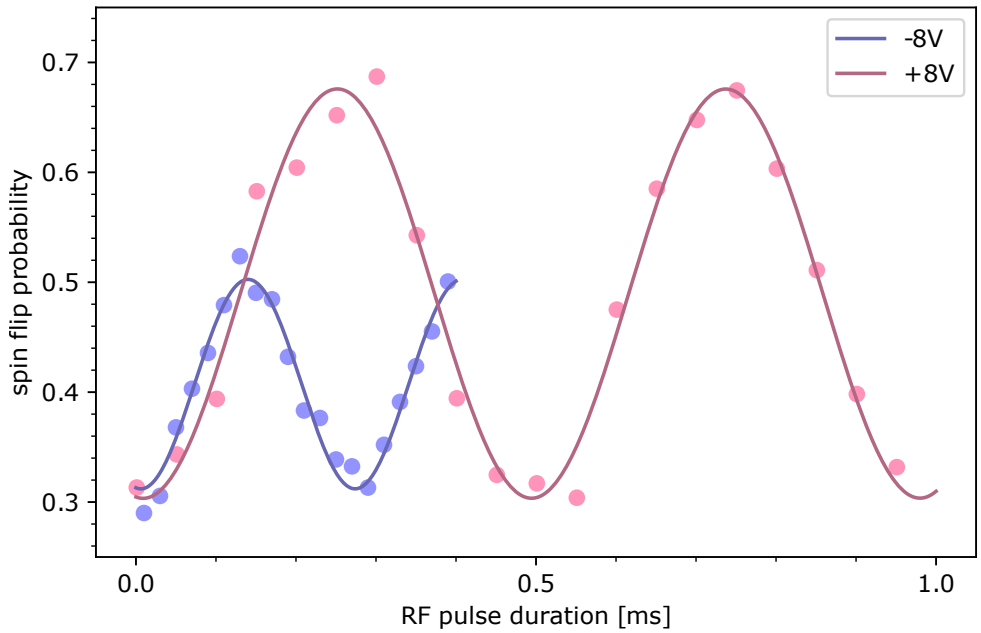

Figure 2.7.: Rabi oscillation of the ^{15}N nuclear spin, recorded by varying the length of the RF pulse (at the frequency of the signal in fig. 2.6) comprising the gate U. The transition frequency is the same for both the negative and the positive charge state, and is therefore not usable as a clear fingerprint. However, the Rabi oscillations show a clear difference in frequency. The supposed NV^+ case is slower by a factor of 1.81 ± 0.04. The higher frequency for the case of NV^- is caused by a mixing of the electron and nuclear spin states.

spin, with a probability proportional to the population of the $m_s = 0$ state. To differentiate the two cases, one can look at the Hamiltonian in eq. 2.1. For calculations of the nuclear spin eigenenergies, H^e can be neglected. When comparing the eigenstates of the coupled Hamiltonian to the product states of the single spin eigenstates (e.g. $|0\uparrow\rangle$ and $|0\downarrow\rangle$, which is the transition that is driven by the RF pulse), one can use first order perturbation theory [11] to obtain the coupled eigenstates $|0\uparrow\rangle \mapsto |0\uparrow\rangle - \frac{A_\perp}{\sqrt{2}(\tilde{\gamma}_\mathrm{e}B_z+D)}|+1\downarrow\rangle$ and $|0\downarrow\rangle \mapsto |0\downarrow\rangle + \frac{A_\perp}{\sqrt{2}(\tilde{\gamma}_\mathrm{e}B_z-D)}|-1\uparrow\rangle$. From that, we can derive the change in susceptibility to an applied RF magnetic field, and thus a Rabi frequency enhancement factor of $1 + \frac{\tilde{\gamma}_\mathrm{e}}{\tilde{\gamma}_\mathrm{n}}\frac{2A_\perp D}{\tilde{\gamma}_e^2 B_z^2 - D^2} = 1.832$ at 470 mT, for the case of a coupled S=1 electron spin, compared to the bare nitrogen nuclear spin Rabi.

Measuring the frequency of Rabi oscillations for a given RF field indeed shows a difference in Rabi frequency for gate voltages of -8 V (NV^-) and 8 V (supposedly NV^+) (see figure 2.7). In fact, the observed ratio of 1.81 ± 0.04 agrees very well with the theoretical value. In addition, the amplitude of the Rabi oscillation for 8 V gate voltage is larger than for the NV^- case. When calculating the charge state probability (eq. 2.2), we obtain unity occupation probability of the $m_s = 0$ electron spin state.

This leads to the conclusion, that at 8 V gate voltage, only one electron spin state, the $m_s = 0$ state, exists (hence the 100% occupation probability). Furthermore, due to the absent hyperfine enhancement, there is no electron spin coupling to the nitrogen nuclear spin at all. The only explanation left is a $S = 0$ ground state of this newly discovered charge state.

2.4. Determination of the charge state dependent ^{14}N quadrupole splitting parameter

As explained in section 2.2, the hyperfine coupling between NV center electron and nuclear spin is only one property of the Hamiltonian (eq. 2.1) capable of identifying the charge state. For ^{14}N nuclear spins, the $m_i = 0$ and $m_i = \pm 1$ are split by an additional term, the quadrupole splitting. Here, an electric field gradient lifts the degeneracy of nuclear spin energy levels with different absolute value of m_i (hence only for $S \geq 1$). In the case of the NV center the electric field gradient causing the quadrupole splitting is due to its electron density at the pace of the nitrogen nuclear spin. The quadrupole splitting parameters for NV^- and NV^0 are known from previous experiments to be $C_q^{(-)} = -4.945$ MHz and $C_q^{(0)} - 4.655$ MHz, respectively [54]. Kohn-Sham density functional theory (DFT) calculations suggest, that the quadrupole splitting parameter for the positive charge state is slightly larger than the value for NV^0, around $C_q^{(+)} = (-4.82 \pm 0.19)$ MHz (with the calculated values for the other charge states being $C_q^{(-)} = (-5.02 \pm 0.19)$ MHz and $C_q^{(0)} = (-4.92 \pm 0.19)$ MHz). In order to gain further proof of the existence of a third

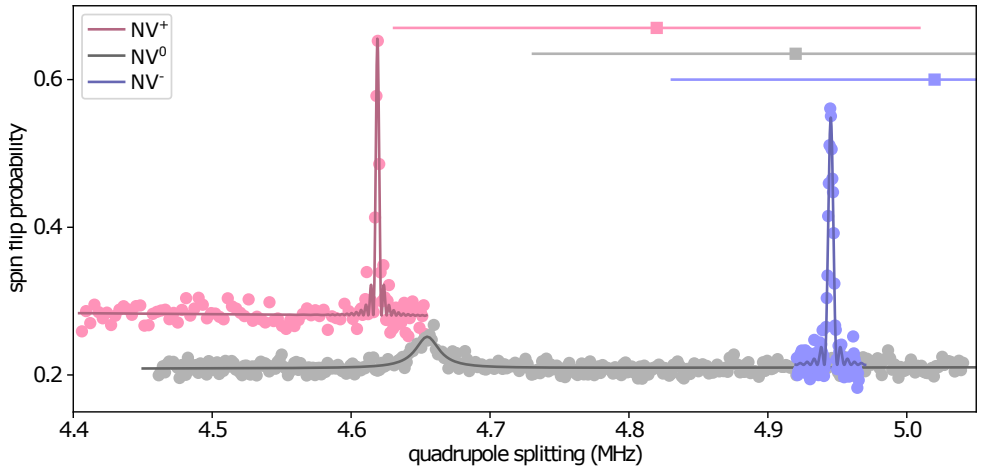

Figure 2.8.: Measurement of the ^{14}N quadrupole splitting parameter for different charge states. The spectra were recorded at gate voltages according to fig. 2.5(c). The Zeeman term was removed from the actual frequency, as was the hyperfine term in case of NV^0 (see text). The NV$^-$ and NV^0 case confirm the previously known results of $C_q^{(-)} = -4.945\,\text{MHz}$ and $C_q^{(0)} - 4.655\,\text{MHz}$, respectively. The quadrupole splitting was measured for the the first time for the NV$^+$ charge state to be $C_q^{(+)} = -4.619\,\text{MHz}$. This result again confirms the different electron density at the nuclear spin, and hence a different charge state. The error bars at the top denote the results from DFT calculations

charge state (and knowledge about the quadrupole splitting parameter $C_q^{(+)}$), NMR on an implanted ^{14}NV is performed. The ^{14}N NMR spectrum, for the $m_i = +1$ to $m_i = 0$ transition is measured for all three charge states, similar to section 2.3. For NV$^-$, the electron spin is initialized into $m_s = 0$. NV^0 does not have the possibility to be initialized, hence the NMR transition is split. We only record one of those lines. The NV$^+$ charge state inherently only shows one line. To obtain a pure quadrupole splitting spectrum, the nuclear Zeeman term and hyperfine contributions (in the case of NV^0) have to be subtracted. The resulting spectra can be seen in figure 2.8, a gaussian fit to the data for NV$^+$ reveals a quadrupole splitting parameter of $C_q^{(+)} = -4.619\,\text{MHz}$.

2.5. Prolonging the lifetime of a nuclear spin quantum memory

When comparing the lifetimes of electron and nuclear spins, electron spins typically relax on a timescale of milliseconds [70], while nuclear spin states can be stable for minutes [4]. However, for coupled electron and nuclear spins, the short relaxation time of the electron spin limits the coherence time of the nuclear spin to around the T_1 time of the electron spin [4, 93, 103]. This limitation can be overcome by decreasing the timescale of relaxation of the electron spin [4, 104] (or see chapter 3). Another way, as was shown in Si:P, another hybrid spin system, is the reversible removal of the electron spin by

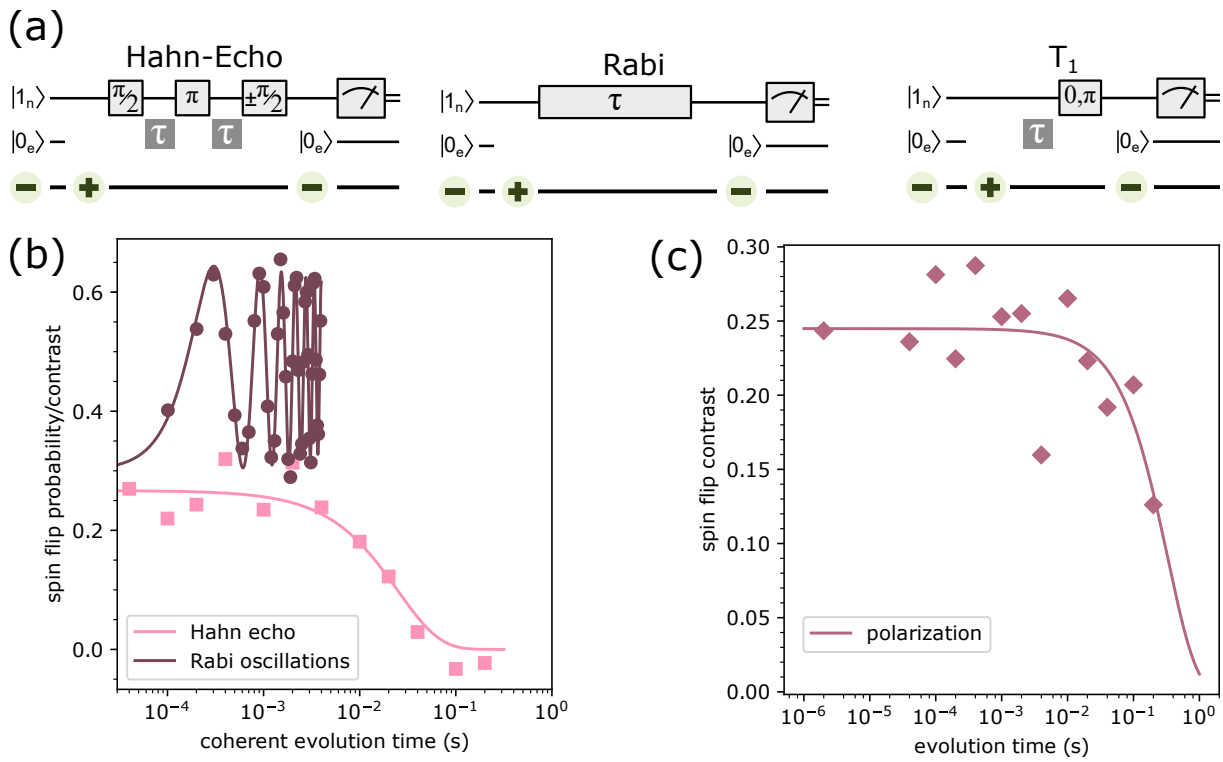

Figure 2.9.: (a) Shows the measurement sequence to measure the T_2 (Hahn echo), T_1^ρ (Rabi) and T_1 lifetimes of the ^{14}N nuclear spin for the positive charge state. For the T_2 and the T_1 measurement, the last RF pulse can rotate the spin in two different directions. Both measurements are performed, and the difference is used as the measurement contrast. (b) The results of the Hahn echo and the Rabi oscillations measurement. The fit reveals a T_2 time of (25 ± 10) ms and a T_1^ρ time of $T_1^\rho = (22 \pm 12)$ ms. The result of the T_1 measurement can be seen in (c). The fitted decay time is around $T_1 \approx 300$ ms, which hints towards an instability of the charge state (see text).

ionization. It was possible, to reach nuclear spin coherence times on the order of minutes (even at room-temperature) for ensembles of spins [98, 99], as well as around a second for single ^{31}P nuclear spins [100, 101]. In the previous chapter, a third, positively charged state of the NV center was identified to incorporate no ground state electron spin. Given that this charge state is stable over time, it has the potential to significantly prolong the coherence time of the host nitrogen nuclear spin (or other ^{13}C nuclear spins in the vicinity of the NV center). To evaluate the nuclear spin coherence time, we alter the measurement sequence from 2.4 to incorporate a Hahn echo pulse sequence after successful initialization of the ^{14}N spin state in the negative charge state, and ionization to NV$^+$. The sequence is shown in fig. 2.9(a). By varying τ and evaluating the spin flip probability for every value, the decay of the transversal magnetization is visible, see fig. 2.9(b). An exponential fit to the measurement data reveals a coherence time of $T_2 = (25 \pm 10)$ ms. Rabi oscillations induced by RF pulses of varying length also show a relaxation on the same timescale, $T_1^\rho = (22 \pm 12)$ ms. The spin lifetimes are clearly prolonged when compared to

the NV$^-$ case, however, they do not quite reach the values expected from measurements of phosphorous nuclear spins in silicon. This can be explained by two effects. First, the NV centers used for this study have been created by nitrogen implantation, which creates NV centers close to the surface. The electron spin coherence time of these defects is often limited to $\sim 10\,\mu$s by paramagnetic defects on the surface, or defects created by the implantation procedure [105–108]. The same effect also influences the coherence of the ^{14}N nuclear spin, however weakened due to the lower g-factor of the nuclear spin ($\tilde{\gamma}_e/\tilde{\gamma}_n \approx 10^5$), to about 100 ms. Another effect is indicated by the relatively short T_1 relaxation time of the ^{14}N nuclear spin of about 300 ms (see fig. 2.9(c)). Since comparable magnetic fields provide ^{14}N T_1 relaxation times of around one minute (see chapter 3) for the negative charge state, one would expect even longer T_1 times for the positive charge state. The measured value can, however, be explained by recombination of NV$^+$ to NV^0, where the T_1 time is limited to around 100 ms due to the fast fluctuation of the electron spin in NV^0. A fluctuation of the charge state on a timescale of ~ 100 ms could explain the short T_1 , as well as the shorter than expected T_2 relaxation times.

2.6. Conclusion

In this chapter, we shed some light on a previously reported dark state of the NV center that could be switched electrically via surface gate structures [1, 92, 109, 110]. This dark state was previously labeled as the positive charged NV$^+$, however, the only evidence was the lack of NV$^-$ as well as NV^0 fluorescence under optical excitation. Since this could potentially also be explained by other mechanisms (e.g. fluorescence quenching due to the conducting surface), another measurement tool to investigate this charge state was needed. We employed the nitrogen nuclear spin inherent to every NV center as a charge state probe [54]. Information about the charge state is available via the electron spin system, whose hyperfine interaction with the nuclear spin can be measured via NMR spectroscopy of a single nuclear spin. An interdigitated structure of hydrogen terminated surface patches, separated by an oxygen termination, makes it possible to alter the Fermi level in the transition region. The charge state of NV centers positioned at the edge of the termination can be controlled by applying a voltage between the two hydrogen terminated (and thus conducting [111]) surfaces. In 2.3 we show, that this device can indeed be used to switch between the negative and the neutral charge state, as well as a third state, in which the electron spin (if there is one) seems to reside in the $m_s = 0$ spin state. The transition from NV$^-$ to this state seems to take place on the order of around 1 ms. By investigating the induced Rabi rotations of the ^{15}N nuclear spin in both the NV$^-$ and the supposed positive charge state, a decreased Rabi frequency is observed in the newly discovered state. The difference fits very well to the expected hyperfine enhancement caused by a coupled $S = 1$ electron spin in NV$^-$, and no electron spin in the

newly discovered charge state. This claim is fortified by the observation of about unity probability to flip the nuclear spin with a single frequency RF pulse, due to no observable hyperfine coupling. Further evidence for a positive charge state is provided in section 2.4. The quadrupole splitting parameter of the ^{14}N nuclear spin is determined by the gradient of the electric field at the position of the nuclear spin. Since this gradient is caused by the electrons of the NV center, removing electrons also changes the quadrupole splitting. For NV$^-$ and NV^0, the quadrupole splitting parameter is known to be $C_q^{(-)} = -4.945\,\mathrm{MHz}$ and $C_q^{(0)} - 4.655\,\mathrm{MHz}$, respectively. We measured the value for NV$^+$ to be $C_q^{(+)} = -4.619\,\mathrm{MHz}$, in rough accordance with DFT calculations. One application of a electron spinless charge state is the prolongation of nuclear spin coherence times. In NV$^-$, the dephasing time of coupled nuclear spins is usually limited by the electron spin's longitudinal ($T_1 \approx 5\,\mathrm{ms}$) relaxation. Similar hybrid spin systems, for example phosphorous donors in silicon, have circumvented this limit by ionization and thus effectively removing the electron spin [98–101]. By initialization of the ^{14}N nuclear spin in NV$^-$, altering the charge state to NV$^+$, and subsequently performing a Hahn echo sequence, a decay on the timescale of $(25 \pm 10)\,\mathrm{ms}$ is visible. This surpasses the longitudinal lifetime of the NV$^-$ electron spin by more than a factor of two. The value is, however, quite low when compared to the coherence time of dilute nuclear spins in NMR experiments (or to Si:P nuclear spins, which are on the order of minutes). Among other things, this can be attributed to the size of the gate structure on the diamond ($\approx 100\,\mu\mathrm{m}$). Different NV centers near the structure did not show the charge state switching on time scales of $\approx 1\,\mathrm{ms}$, but showed a slow change in fluorescence on the order of seconds. These NV centers were not used for experiments, however, they hint towards a slow change in charge environment. By using different gate architectures, this can be sped up to around 1 ns [110]. Fast switching would have another huge advantage. In our experiment, perpendicular components of the nitrogen nuclear spin state are lost when changing the charge state, only the parallel component is kept. When the timescale of the charge state switching is much larger than $1/A_{\parallel}$, the complete state might be uninfluenced by switching the charge state. This would make the positive NV center a very good candidate for a Kane-like architecture of a quantum processor [112].

3. High-resolution spectroscopy of single nuclear spins assisted by a nuclear spin memory

Apart from being used in quantum registers, the nitrogen-vacancy center (NV center) is an exceptional nanoscale quantum sensor, capable of working at room temperature. It can be used to measure magnetic [22, 23] and electric fields [25], temperature [28, 30] and pressure [113]. One application of magnetic field sensing with the NV center is nanoscale nuclear magnetic resonance (NMR) spectroscopy, inside [18, 20, 103] as well as outside the diamond lattice [33–35]. The spectral resolution of these experiments is sufficient to distinguish between different nuclear spin species [36, 69]. However, modern applications of NMR spectroscopy in biology, chemistry and medicine [114–116] requires spectral resolutions on the order of a few Hertz. In this chapter, we elucidate the influence of the quantum nature of the NV center electron spin (sensor spin) on the achievable spectral resolution. Even though the electron spin lifetimes of NV centers in diamond are among the longest at room-temperature, they are greatly surpassed by nuclear spins in liquids. Hence, the electron spin can't detect the nuclear spin precession with the highest resolution [84, 86]. In this work, this problem is overcome by utilizing a long-lived memory, the ^{14}N nuclear spin (memory spin). Furthermore the deleterious effect of dissipation mediated by the sensor spin on ^{13}C NMR (target spins) is analyzed and overcome by various methods. The results are published in [3, 4].

3.1. Spectral resolution of an NV center quantum sensor

NMR spectra are usually obtained, by observing the free Larmor precession of nuclear spins. The resulting measurement in the time domain is then Fourier transformed, to obtain a spectrum. An observable signal in general has the form

$$S(t) = A_0 e^{-t/\tau} \cdot \cos(2\pi\nu t), \tag{3.1}$$

with the signal decay time τ and the signal frequency ν. This results in a peak in the Fourier transformed spectrum with a full width at half maximum (FWHM) linewidth of

$$\Delta\nu = 1/\pi\tau. \tag{3.2}$$

For NMR measurements, the decay of the signal is determined by the inhomogeneous decay T_2^* of the nuclear spins. In the case of measurements using the NV center, the electron spin is used as a memory for the precession signal, which can therefore be recorded up to a spin memory time T^{mem} [84, 86, 103]. The linewidth can then be expressed as

$$\Delta\nu = \frac{1}{\pi}\left(\frac{1}{T_2^*} + \frac{1}{T^{\text{mem}}}\right) \tag{3.3}$$

With the NV center electron spin lifetime of about 5 ms, this results in a NMR linewidth limited to about 100 Hz in correlation spectroscopy sequences, similar to the Mims electron nuclear double resonance (ENDOR) sequence [84, 86].

3.1.1. Introducing a long-lived quantum memory

In correlation spectroscopy sequences, two phase accumulation parts are separated in time, during which one component of the spin state is transferred to the quantization axis of the spin. This increases the available correlation time to the T_1^{sens} time of the manipulated electron spin. NV centers in diamond inherently consist of two spins, the electron spin with exceptional sensing and readout capabilities (referred to as sensor spin), as well as the strongly coupled ^{14}N nuclear spin (referred to as memory spin). This strong coupling can be utilized, to perform conditional gates between electron and nuclear spin, enabling the transfer of a quantum mechanical phase. In ref. [103], the correlation spectroscopy sequence is altered in a way, that the accumulated phase is transferred onto the long living ^{14}N nuclear spin, instead of the electron spin z-component. However, due to the strong coupling, the dephasing time of the ^{14}N nuclear spin is strongly limited by the electron spin T_1^{sens} lifetime (see fig. 3.1). Interestingly, the T_1^{mem} lifetime of the ^{14}N nuclear spin is not influenced by the electron spin. Applying a bias magnetic field of above ∼2000 G, aligned along the symmetry axis of the NV center, increases the T_1^{mem} lifetime to a point, where even quantum non-demolition measurements of the nuclear spin are possible [15]. In fig. 3.1 (a), measurements of the T_2 time of the electron (T_2^{sens}) and nuclear spin (T_2^{mem}), as well as a measurement of the T_1^{mem} time can be seen. While T_2^{mem} is limited to ∼6 ms, the T_1^{mem} lifetime greatly surpasses that value. It is limited by spin flip flops with the NV center electron spin to about 240 s. This long storage time can be used to prolong the frequency resolution of correlation spectroscopy sequences, employing the ^{14}N nuclear spin longitudinal polarization as an intermediate memory, instead of the electron spin's.

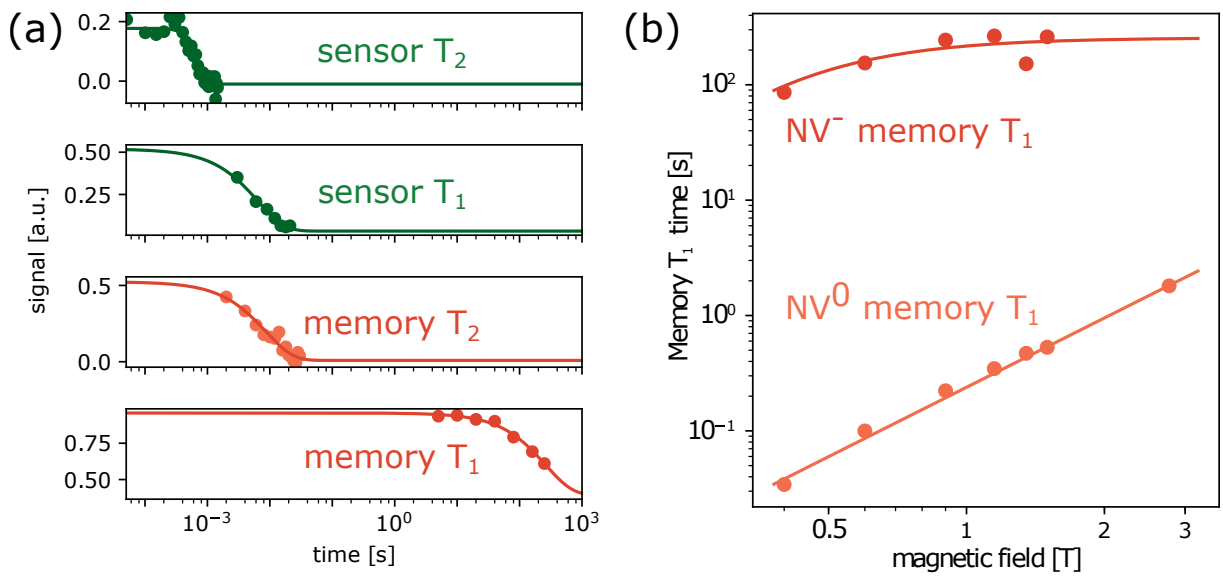

Figure 3.1.: In (a), the spin lifetimes of the NV center electron (sensor) and ^{14}N nuclear (memory) spin are shown, for a magnetic field of 1.5 T. $T_2^{\text{sens}} = 688\,\mu\text{s}$, $T_1^{\text{sens}} = 6.4\,\text{ms}$ and $T_2^{\text{mem}} = 8.6\,\text{ms}$ are on the order of a few milliseconds, ultimately limited by the sensor T_1^{sens} time. The T_1^{mem} time, however, strongly surpasses that value, and reaches 240 s. (b) Shows the scaling of the T_1^{mem} time with the applied magnetic field, for the negative and the neutral charge state of the NV center. The NV^0 measurement is fitted with a quadratic dependence of lifetime on magnetic field, $(T_1^{\text{mem}})_{\text{NV}^0} = (0.239 \pm 0.003)\,\text{sT}^{-2} \cdot B^2$. For the NV$^-$ case, the expected quadratic behavior could not be reproduced, probably due to a yet unknown decay mechanism dominating at high magnetic fields. It was empirically fitted with the equation $(T_1^{\text{mem}})_{\text{NV}^-} = \left[((1700 \pm 1200)\,\text{sT}^{-2} \cdot (B - 0.1\,\text{mT})^2)^{-1} + ((260 \pm 40)\,\text{s})^{-}\,1\right]^{-1}$.

3.1.2. Entanglement based correlation spectroscopy

In order to use the hybrid spin system comprised of sensor and memory spin to full extend, we devise a sensing sequence that employs an entangled state between the two spins to accumulate a signal phase from the target spins (similar to ref. [103]). The complete sensing sequence can be seen in figure 3.2 (a). We start of with a sensor spin initialized by optical excitation, while the memory spin is in general in a mixed state. By using the results of the previous measurement of the memory spin to post-select $m_i = +1$ states, the resulting state at the beginning of the measurement sequence can be written as

$$|\Psi_s\rangle \otimes |\Psi_m\rangle = |0_\mathrm{s}\rangle \otimes |1_\mathrm{m}\rangle = |01\rangle \,. \tag{3.4}$$

For the whole experiment, the sensor is only manipulated in the $m_s = 0$ and $m_s = -1$, the memory in the $m_i = +1$ and $m_i = 0$ manifold. Both can therefore be viewed as two-level systems (qubits). Next, the memory spin is rotated by an angle of $\pi/2$ around the x-axis. This leaves the system in the state

$$|\Psi\rangle = 1/\sqrt{2}\,(|0_\mathrm{s}\rangle \otimes (|0_\mathrm{m}\rangle + |1_\mathrm{m}\rangle))\,. \tag{3.5}$$

The influence of magnetic fields on this superposition state is negligible, since the gyromagnetic ratio of the nuclear spin is 5 orders of magnitude smaller than the electron's. Afterwards, we perform one of four possible basic sensing steps. They comprise of two controlled NOT gate (CNOT gate)s on the sensor spin (represented by the conditional π rotations in the wire diagram, the open or filled circle denote the memory's conditional state), separated by a phase accumulation time. The first CNOT gate entangles sensor and memory spin, e.g.

$$|\Psi\rangle = 1/\sqrt{2}(|0_\mathrm{s}\rangle \otimes |0_\mathrm{m}\rangle + |1_\mathrm{s}\rangle \otimes |1_\mathrm{m}\rangle) = 1/\sqrt{2}(|0_\mathrm{s}0_\mathrm{m}\rangle + |1_\mathrm{s}1_\mathrm{m}\rangle). \tag{3.6}$$

Any momentary magnetic field offset (i.e. also due to nuclear spin statistical polarization) causes the entangled state to accumulate a phase

$$|\Psi\rangle = 1/\sqrt{2}\left(e^{i\phi_0}\,|0_\mathrm{s}0_\mathrm{m}\rangle + e^{i\phi_1}\,|1_\mathrm{s}1_\mathrm{m}\rangle\right). \tag{3.7}$$

The second CNOT gate disentangles the hybrid spin system, leaving the sensor spin in one of its eigenstates, and the memory spin in a superposition

$$|\Psi\rangle = 1/\sqrt{2}\left(|0_\mathrm{s}\rangle \otimes (e^{i\phi_0}\,|0_\mathrm{m}\rangle + e^{i\phi_1}\,|1\rangle_\mathrm{m})\right). \tag{3.8}$$

When comparing the state before (eq. 3.5) and after (eq. 3.8) the sensing step, it can be seen that a phase was added to the superposition state, which is dependent on the

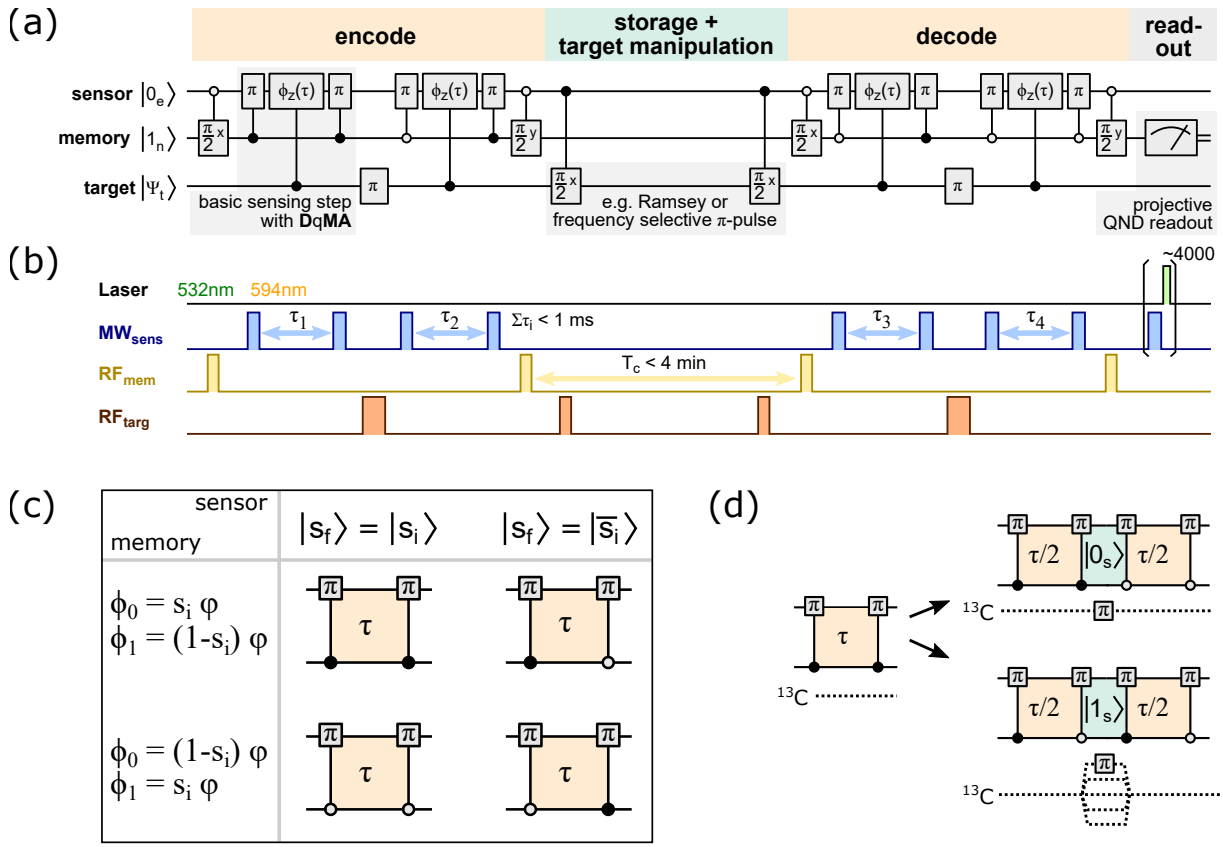

Figure 3.2.: (a) Shows a wire diagram of the spin detection (via a Ramsey measurement) sequence that fully utilizes the NV center electron spin as a sensor, and the ^{14}N nuclear spin as a memory. The sequence is similar to the correlation spectroscopy sequence (see sec. 1.7.6). It is split in four parts: encoding, storage and target manipulation, decoding and readout. The sequence is explained in detail in sec. 3.1.2. (b) shows the sequence in a pulse scheme representation. (c) Four different sensing steps are possible, characterized by the condition of the π pulses on the sensor spin. Steps in the left column do not alter the sensor spin state ($|s_f\rangle = |s_i\rangle$), while the ones on the right invert it ($|s_f\rangle = |\overline{s_i}\rangle$). The different rows add the phase either to the $|0\rangle$ ^{14}N spin state (ϕ_0), or the $|1\rangle$ state (ϕ_1). (d) Two basic sensing steps, in conjunction with an inversion pulse on the target spins, can be combined to an echo-type sensing step. This can be used to further restrict the origin of the phase ϕ to the desired target spins (see appendix B.4).

momentary magnetic field. After the second CNOT gate, the sensor spin is returned to an eigenstate.

In general, this leaves room for four different kinds of sensing steps, that either change the sensor spin state or not, and add the phase to the $|0\rangle$ or $|1\rangle$ memory state (see fig. 3.2(c)). The encoding part of the detection sequence continues with a second sensing step, where one CNOT gate has a changed conditional state. This causes the $|0\rangle$ memory state to accumulate a phase ϕ_1, and the $|1\rangle$ state ϕ_0. Since afterwards both memory states possess the same phase $\phi_0 + \phi_1$, it can be canceled out by adding a global phase, thus removing any information about the magnetic field (similar to a Hahn echo sequence (see sec. 1.7.4)). However, by manipulating the target spins in between the two sensing steps, their magnetization can be flipped. This causes an effective phase accumulation of $2 \cdot \phi_0$ on state $|0\rangle$, and $2 \cdot \phi_1$ on $|1\rangle$ (assuming the phase is only accumulated due to the target spins). The encoding part is finalized by a $\pi/2$ pulse on the memory spin, 90° phase shifted to the initial one, transferring the x-component of the memory spin to its quantization axis. By adding a global phase, it is clear, that only the phase difference $\Delta\phi = \phi_1 - \phi_0$ can be measured

$$|\Psi\rangle = e^{-(\phi_0+\phi_1)/2} |0\rangle \otimes (e^{i\Delta\phi/2} |0\rangle + e^{-i\Delta\phi/2} |1\rangle). \tag{3.9}$$

During the following storage and target manipulation part, only the target spins are manipulated, while the information about the target spin magnetization is saved on the long-living component (the z-component) of the memory spin, for up to 240 s (see fig 3.1). In the case of a Ramsey sequence, the free evolution time of the target spins can therefore be prolonged up to this timescale. The decoding part is essentially the same as the encoding part, effectively correlating the phase from the first two and the last two sensing steps. Target manipulation during the storage time changes the correlation. Finally, the x-component of the memory spin is again transferred to the z-component, with subsequent readout of the z-component expectation value $\langle I_z \rangle$ via single-shot readout (SSR) [15].

3.2. Characterization of the combined sensor, memory and target spin system

In the previous section 3.1.2, a detection sequence using the entangled sensors and memory spin system, was introduced. To evaluate the capabilities in terms of single spin detection, we use the diamond crystal described in appendix B.1 to detect weakly coupled ^{13}C nuclear spins. The experimental setup is described in sec. 1.5. The goal is to spectroscopically investigate a single nuclear spin in a test-bed environment in order to gain knowledge about future applicability of the sequence in single spin NMR of spins in liquids or solids outside the diamond. We therefore search the diamond crystal for an NV center coupled

to a ^{13}C spin, with a hyperfine coupling of about 1 kHz (the limit for single spin detection is given by $\sim 1/T_2^{\text{sens}}$).

3.2.1. The reduced three spin Hamiltonian

In order to better understand the system comprised of a hybrid, two spin quantum sensor and the target spin(s), we look at the Hamiltonian of the combined system

$$\hat{H} = \hat{H}^{\text{sens}} + \hat{H}^{\text{mem}} + \hat{H}^{\text{tar}} + \hat{H}^{\text{coupl}}. \tag{3.10}$$

The first three terms, $\hat{H}^{\text{sens}}$, $\hat{H}^{\text{mem}}$ and $\hat{H}^{\text{tar}}$ are the single spin Hamiltonians for the uncoupled sensor, memory and target systems, comprised of the respective Zeeman energies and the zero-field terms, where applicable. The hyperfine coupling of the spins is formulated in the fourth term $\hat{H}^{\text{coupl}}$. We only account for components of the hyperfine interaction along the quantization axis, since perpendicular terms can be neglected due to the high magnetic field, compared to the coupling ($\sim$16 MHz compared to $\sim$1 kHz). The components of the Hamiltonian can then be written as

$$\hat{H}^{\text{sens}} = D\hat{S}_z^2 + \tilde{\gamma}^{\text{sens}} B_z \hat{S}_z \tag{3.11}$$

$$\hat{H}^{\text{mem}} = C_q^{\text{mem}} (\hat{I}_z^{\text{mem}})^2 + \tilde{\gamma}^{\text{mem}} B_z \hat{I}_z^{\text{mem}} \tag{3.12}$$

$$\hat{H}^{\text{tar}} = \tilde{\gamma}^{\text{tar}} B_z \sum_{\text{samp}} \hat{I}_z^{\text{tar}} \tag{3.13}$$

$$\hat{H}^{\text{coupl}} = \hat{S}_z A_{zz}^{\text{mem}} \hat{I}_z^{\text{mem}} + \hat{S}_z \sum_{\text{samp}} A_{zz}^{\text{tar}} \hat{I}_z^{\text{tar}} \tag{3.14}$$

$$\tag{3.15}$$

with the sensor spin operator $\hat{S}_z$ and memory and target spin operators $\hat{I}_z^{\text{mem}}$ and $\hat{I}_z^{\text{tar}}$, respectively. $\tilde{\gamma}$ denotes the respective reduced gyromagnetic ratios (gyromagnetic ratio divided by 2π) of the sensor ($\tilde{\gamma}^{\text{sens}} = 28\,\text{GHz/T}$), the memory ($\tilde{\gamma}^{\text{mem}} = 3.076\,\text{MHz/T}$) and the target spins ($\tilde{\gamma}^{\text{tar}} = 10.705\,\text{MHz/T}$). The zero-field splitting parameters of the spin-1 systems are $D = 2.87\,\text{GHz}$ and $C_q^{\text{mem}} = -4.945\,\text{MHz}$, for sensor and memory spin, respectively.

3.2.2. Measuring the target hyperfine coupling parameters

We start of by measuring ^{13}C NMR spectra, by replacing the target spin Ramsey in fig. 3.2 with a radio frequency (RF) π pulse of varying frequency. When the pulse is on resonance, the memory spin population changes, resulting in a spectrum. Fig. 3.3(a) shows two spectra, the difference being the sensor spin state during storage and manipulation[1]. As explained in 3.1.2, by carefully choosing the conditions of the CNOT gates, the sensor

[1]The function used for fitting is explained in sec. 1.7.2

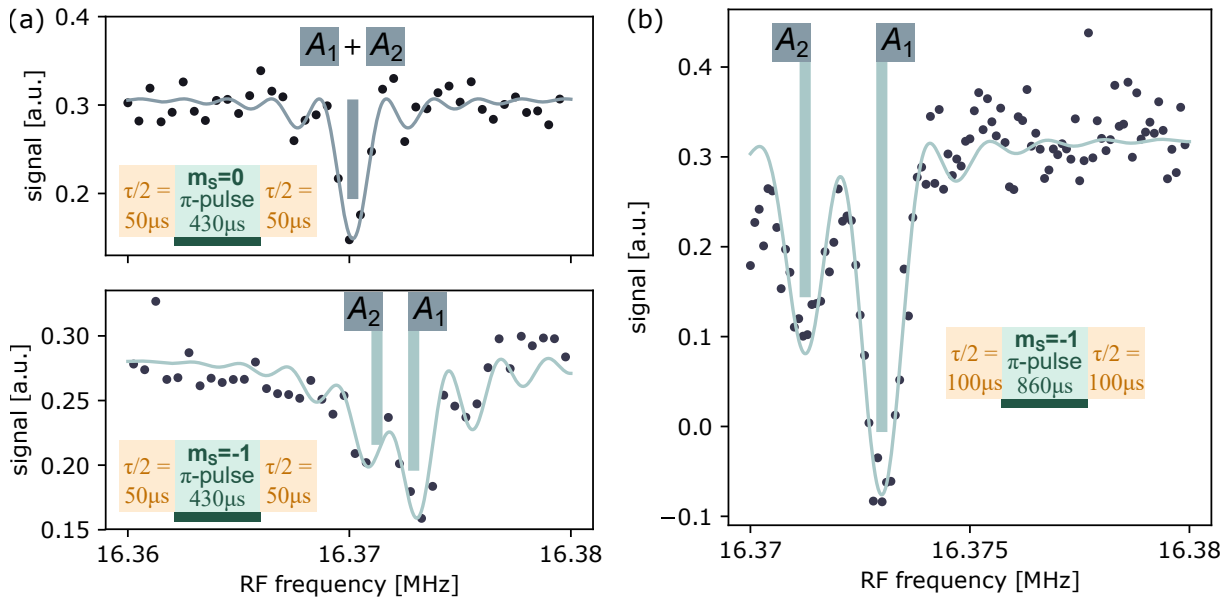

Figure 3.3.: (a) Shows two ^{13}C NMR spectra recorded with the detection sequence introduced in sec. 3.1.2. The inset shows the schematic pulse sequence, with the two orange parts denoting the encoding and decoding, respectively, and the green part representing the target manipulation. In this experiment, the Ramsey sequence from fig. 3.2(a) was changed to an RF pulse of variable frequency. The length and amplitude of the pulse were set to perform a rotation of π. In the upper graph, the sensor state during the RF manipulation was set to be $m_s = 0$, in the lower it was set to $m_s = -1$. The resonance in the upper graph is at the bare ^{13}C Larmor frequency, while splitting in two in the lower graph. The fit is an overlay of the signal from two ^{13}C nuclear spins (see text), the thick lines denote the respective resonances. In (b), the amplitude of the driving RF field was halved, and the duration of the pulse was doubled. As can be seen, this increases the spectral resolution, and hence the two signals can be distinguished better.

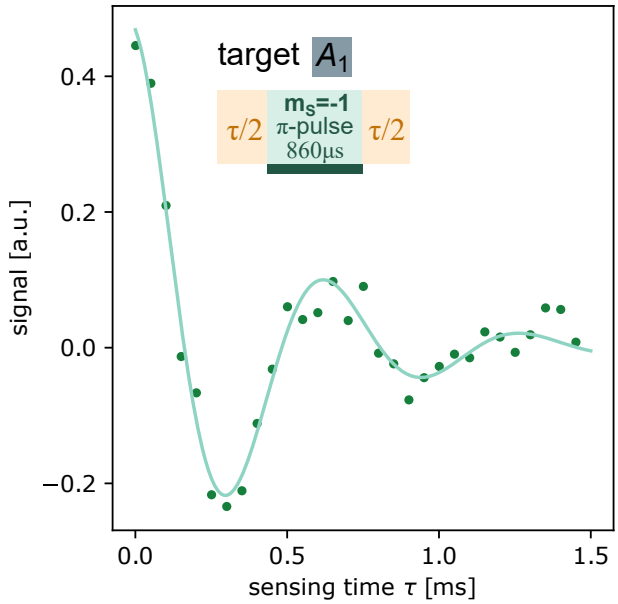

Figure 3.4.: Evolution of the $\langle I_z \rangle$ expectation value of the memory spin (signal) with an RF pulse resonant on target A_1, depending on the overall phase acquisition time during encoding and decoding. The fit reveals a parallel hyperfine coupling of $A_{zz} = 2.8\,\text{kHz}$.

spin can be in its $|m_s = 0\rangle$ or $|m_s = -1\rangle$ state during storage. For $|m_s = 0\rangle$, the ^{13}C target spins' resonance frequency is uninfluenced by the hyperfine interaction. Therefore, all target spins contributing to the signal overlap at the pure Larmor frequency. When initializing the sensor to $m_s = -1$, this degeneracy is lifted, the resonance of every spin shifted by its respective hyperfine interaction A_{zz}. The spectrum in fig. 3.3(a) can be explained by contributions of two (A_1 and A_2) target spins. Fig. 3.3(b) shows a hyperfine split spectrum of the same spins, recorded with longer duration of the RF π pulse. This results in a higher spectral resolution, showing a parallel hyperfine splitting of the target spin A_1 of $A_{zz} = 2.8\,\text{kHz}$. In order to verify, that spin A_1 is in fact a single ^{13}C nuclear spin, we fix the RF frequency on resonance, and vary the overall phase accumulation time, between the two CNOT gates of all four sensing steps. The accumulated phase and the final memory $\langle I_z \rangle$ expectation value goes according to

$$\Delta\phi = A_{zz} \cdot \tau \tag{3.16}$$

$$\langle I_z \rangle = \cos\left(A_{zz} \cdot \tau\right) \tag{3.17}$$

The measurement results can be seen in fig. 3.4. Since the parallel hyperfine interaction determined in figs. 3.3 and 3.4 are the same, we can conclude to observe the signal of a single spin. This target spin will be referred to as A1. Another NV center with an even weaker coupled ^{13}C spin was found in the same way. The target spin, referred to as B1 has a coupling of $-1.8\,\text{kHz}$, the spectrum can be seen in appendix B.2.

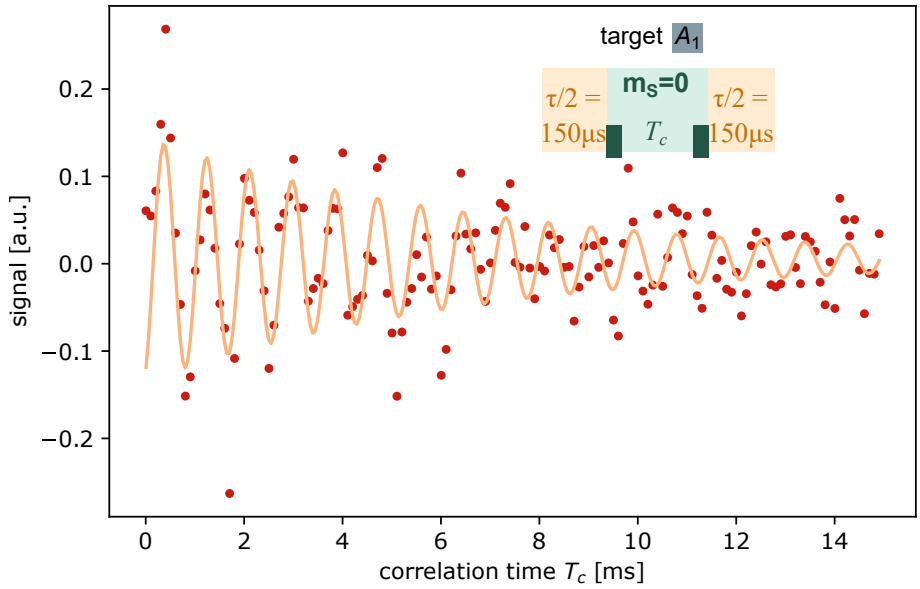

Figure 3.5.: (a) Shows the coherent Ramsey oscillations of ^{13}C target spin A_1. The measurement sequence is as in fig. 3.2(a), with the CNOT gates chosen to set the sensor spin to its $m_s = 0$ state during the target Ramsey sequence. The total phase acquisition time was set to 300 μs, to obtain a high signal from target A_1 (compare fig. 3.4). The decay time of the signal is $T_2^* = (6.85 \pm 1.20)$ ms. It is limited by the targets coupling to the sensor spin, and its T_1^{sens} time of (6.4 ± 0.6) ms.

3.2.3. Sensor relaxation effects on memory and target spins

In order to understand the mutual influence between sensor, memory and target spins, we again look at the spin lifetimes. At room-temperature, the NV center sensor spin's longitudinal relaxation (T_1^{sens}) is around 5 ms, limited by coupling to local phononic modes via spin-orbit coupling [70]. The NV center used in this experiment has a T_1^{sens} time of (6.4 ± 0.6) ms, as can be seen in fig. 3.1(a). The close relation of this value to the T_2^{mem} is visible. Looking closely at the Hamiltonian (eq. 3.11), a qualitative explanation can be given. Since only the hyperfine component along the quantization axis is considered, the sensor spin's influence on the memory and target spins can be considered as a fluctuating magnetic field, with a correlation time of T_1^{sens} . In case of the memory spin, the amplitude of this fluctuation is quite large (2.16 Mhz), while it is smaller for the target spins ($\sim$1 kHz). Therefore the memory spin dephasing due to a random sensor spin flip is instantaneous, compared to the timescale of the measurement (the timescale of the dephasing is $1/A_{zz} \sim 0.5\,\mu$s, compared to the T_1^{sens} time of 6 ms). Even though the coupling of the target spin is orders of magnitude smaller than that of the memory spin, its coherence time $T_2^* = (6.85 \pm 1.20)$ ms is still limited by the sensor's T_1^{sens} time (see fig. 3.5).

A more quantitative explanation of this effect can be gained by a master equation approach. Since the memory is not needed to model the effect of the sensor on the target,

and vice versa, we model a two spin system, one electron and one nuclear spin. The state of the system can be expressed by the density matrix $\rho = \rho_\mathrm{e} \otimes \rho_\mathrm{n}$, with the sensor and target spin density matrix ρ_e and ρ_n, respectively. The system evolution, including relaxation effects, then behaves like

$$\begin{aligned}\dot{\rho}(t) = &- i2\pi[\hat{H}, \rho(t)] \\ &+ \sum_j L_j \rho L_j^\dagger - \frac{1}{2}\left(L_j^\dagger L_j \rho + \rho L_j^\dagger L_j\right).\end{aligned} \tag{3.18}$$

The Lindblad operators L_j describe the stochastic decay of the sensor spin state. The depolarization of the sensor spin, in the regime of high temperature ($E/k_\mathrm{B}T = 0.014 \ll 1$) can be expressed by the depolarizing quantum operation [117]

$$\mathcal{E}(\rho_\mathrm{e}) = \left(1 - \frac{\Delta t}{T_1^\mathrm{sens}}\right)\rho_\mathrm{e} + \frac{\Delta t}{T_1^\mathrm{sens}}\frac{\mathbf{1}_\mathrm{e}}{3}, \tag{3.19}$$

for short time-steps $\Delta t \ll T_1^\mathrm{sens}$. The operator sum representation is

$$\begin{aligned}\mathcal{E}(\rho_\mathrm{e}) &= \sum_k E_k \rho_\mathrm{e} E_k^\dagger \\ &= \left(1 - \frac{\Delta t}{T_1^\mathrm{sens}}\right)\rho_\mathrm{e} + \frac{\Delta t}{3T_1^\mathrm{sens}} \sum_{n,m=-1}^{1} |n\rangle\langle m|\,\rho_\mathrm{e}\,|m\rangle\langle n|,\end{aligned} \tag{3.20}$$

and the corresponding Lindblad operators are

$$L_{j=3m+n+5} = \frac{1}{\sqrt{3T_1^\mathrm{sens}}}\,|m\rangle\langle n| \otimes \mathbf{1}_\mathrm{n}, \tag{3.21}$$

with m, n being the sensor spin eigenstates $m_s = -1, 0, 1$, and $j = 1, ..., 9$. The influence of sensor spin depolarization on target spin coherence can then be reconstructed by solving eq. 3.18 numerically (by using the QuTiP framework for Python [118]), with the initial state $\rho_\mathrm{e} = |0\rangle\langle 0| \otimes |x\rangle\langle x|$. After a time t, the remaining coherence can be quantized by the value $\langle\sigma_x\rangle = \mathrm{Tr}\left\{\mathrm{Tr}_\mathrm{e}\left[\rho(t)\right]\sigma_x\right\}$. By determining the decay time T_2^* for different coupling strengths, we can differentiate between regions of strong and weak coupling, see fig. 3.6. The region of strong coupling, set by $A_\mathrm{zz} > 1/T_1^\mathrm{sens}$, has a fixed coherence time of

$$T_2^* = 3T_1^\mathrm{sens}/2. \tag{3.22}$$

This can be understood by looking at the depolarizing quantum operator from eq. 3.19. The decay out of state $m_s = 0$ happens with the rate $2/(3T_1^\mathrm{sens})$, while the mixed state $\mathbf{1}_\mathrm{e}$ is populated with the rate $1/T_1^\mathrm{sens}$. For strongly coupled spins, decoherence occurs instantly compared to the timescale of T_1^sens , upon a spin flip from $m_s = 0$ to $m_s = \pm 1$. The prefactor 3/2 stems from the fact, that coherence of the target spin is destroyed

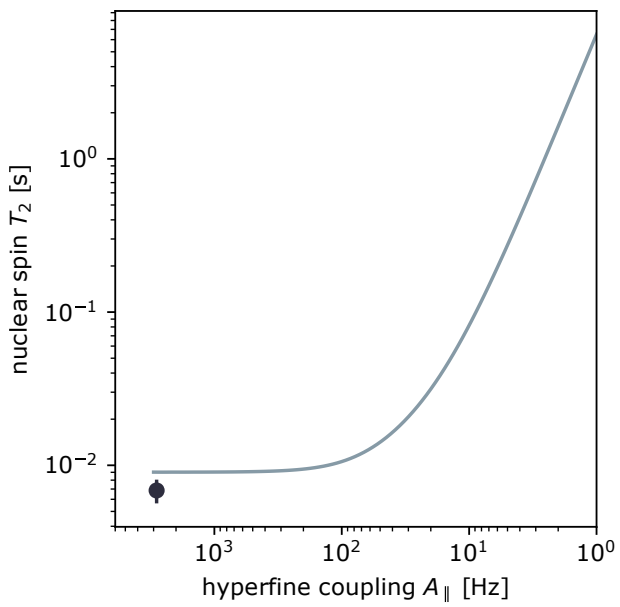

Figure 3.6.: Target spin T_2 over hyperfine coupling strength without dissipative decoupling, by numerically solving the Master equation (eq. 3.18) with an assumed sensor decay time of $T_1 = 6\,\mathrm{ms}$. Two different regimes can be seen: The regime of strong coupling, where $A_{zz} > 1/T_1$, and the weak coupling regime $A_{zz} < 1/T_1$. For strong couplings, the target spin coherence is limited by $3T_1/2$, for weak couplings the coherence time increases according to $T_2 \propto A_{\mathrm{zz}}^{-2}$. The plotted measurement point corresponds to the measurement from fig. 3.5

by two consecutive spin flips from $m_s = 0$ to $m_s = \pm 1$, and back, while the measured polarization is not. This is verified by measurements on the memory spin (see fig. 3.1). The weakly coupled regime is set by $A_{\mathrm{zz}} \ll {}^{1}/_{T_1^{\mathrm{sens}}}$. Here, only a tiny random phase

$$\delta\phi \sim A_{\mathrm{zz}} T_1^{\mathrm{sens}} m_{\mathrm{s}} \tag{3.23}$$

is added to the target spin superposition state by a sensor spin flip. Since this phase is much smaller than 2π, the phase undergoes a random walk, with its uncertainty being

$$\sigma_\phi \propto \delta\phi \sqrt{t/T_1^{\mathrm{sens}}}. \tag{3.24}$$

This results in a scaling of T_2^* with the hyperfine coupling strength of

$$T_2^* \propto T_1^{\mathrm{sens}}/\delta\phi^2 \propto (T_1^{\mathrm{sens}})^{-1} \cdot A_{\mathrm{zz}}^{-2}. \tag{3.25}$$

As can be seen in fig. 3.6, the motional averaging regime starts with a coupling of around 50 Hz, corresponding to a distance of 15 nm between the sensor and a hypothetical proton spin. Hence, in previous NMR experiments detecting proton spins on the surface of the diamond, the spectral linewidth was limited by the sensor [33, 35, 36, 69].

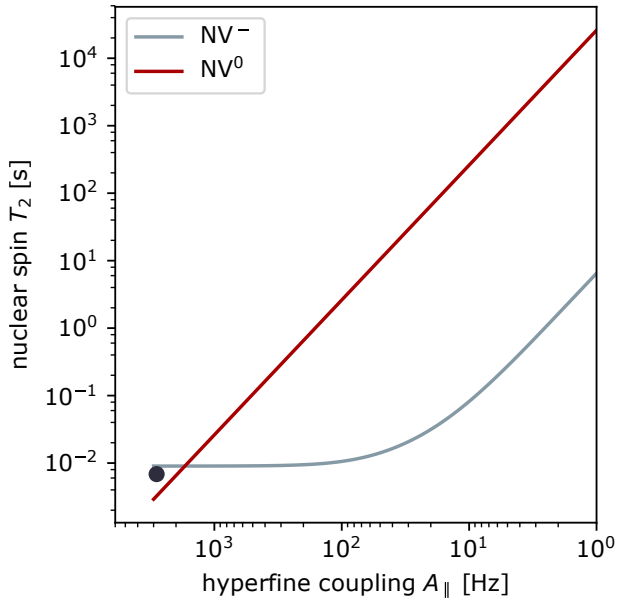

Figure 3.7.: Target spin T_2 time over hyperfine coupling strength with the sensor ionized to the neutral charge state NV^0. Again, the Master equation from eq. 3.18 was solved numerically, but for a much shorter sensor T_1 time of $13\,\mu$s. For comparison, the previous calculated behavior for the negative charge state is included.

3.3. Decoupling by ionization to NV^0

In order to circumvent the deleterious effects of the sensor spin on the target spins, one has to look at eq. 3.25 and eq. 3.22. Since decreasing the hyperfine interaction A_{zz} (by placing the target further away from the sensor) also strongly decreases the signal accumulated from the nuclear spin, we concentrate on T_1^{sens} . In principle, the coherence time can be increased by increasing T_1^{sens} , for example by cooling the diamond to cryogenic temperatures [70]. This would, however, restrict possible applications of NMR with NV centers to low temperatures. Decreasing T_1^{sens} prolongs the coherence of a weakly coupled target spin in the motional averaging regime. This can be done for example by very fast ionization and recombination of the electron spin [104]. Another possibility intrinsic to NV centers in diamond is the neutral charge state. In its ground state, NV^0 is comprised of an orbital, as well as an electron spin doublet [119]. It was shown, that this leads to fast decoherence of the ^{14}N nuclear spin [54], which can be modeled by a fast fluctuation $S = 1/2$ electron spin with a lifetime of $T_1^{NV^0} \approx 13\,\mu s$[2]. The same calculation as in sec. 3.2.3 can be used to calculate the target spin T_2^* times, which can be seen in fig. 3.7. For couplings stronger than $\approx 50\,$kHz, T_2^* is limited to around $20\,\mu$s, while for weaker couplings the same quadratic increase due to motional averaging as in fig. 3.6 can be seen. For couplings smaller than $\sim 1.7\,$kHz, target spin T_2^* for the neutral charge state

[2]This is an empirical value, that was chosen to reproduce the experimental results well. Ref. [54] reports $T_2 = 6\,\mu$s, which would result in $T_1 = 4\,\mu$s.

surpasses the value for the negative one.

3.3.1. Verification of the motional averaging effect

In order to verify the motional averaging effect on the target spin for the neutral charge state, a coupling smaller than for target A_1 ($A_{zz} = 2.8\,\text{kHz}$) is needed. We therefore change to target B_1, with a coupling of $A_{zz} = -1.8\,\text{kHz}$ (see 3.2.2 and appendix B.2). The measurement sequence from sec. 3.1.2 is varied slightly. After the encoding step, a 1 ms long laser pulse at a wavelength of 594 ms is used to ionize the NV center, with a probability of around 90% [55]. The following target Ramsey sequence is then performed in the neutral charge state (even though NV^0 has an electron spin $S = 1/2$, due to motional averaging, the target spin transition frequency is the pure Larmor frequency of ^{13}C nuclear spins). After the second $\pi/2$ pulse of the Ramsey sequence, the NV center is brought back to the negative charge state by a $1\,\mu s$ long laser pulse at a wavelength of 532 nm. The schematic pulse sequence is shown in fig. 3.8(a). The result of the Ramsey measurement can be seen in fig. 3.8(b). The decay can be fitted to $(7.8 \pm 1.3)\,\text{ms}$, as expected by the calculations. It should be noted, that in this method, the signal is decreased by the infidelity of the optical ionization ($\approx 90\%$) and recombination ($\approx 70\%$)

3.4. Decoupling by continuous weak excitation

As was shown in sec. 3.3, the increased NV center electron spin dissipation in the neutral charge state enables the prolongation of target spin coherence at a coupling of around 1.7 kHz. In this thesis however, the spins under investigation are coupled with $A_{\parallel} = 2.8\,\text{kHz}$ (A1) and $A_{\parallel} = -1.8\,\text{kHz}$ (B1). Hence, a different approach is needed, in order to prolong the coherence time of these spins. In ref. [104], the authors examined a weakly coupled ^{13}C spin ($A_{\parallel} \approx 3\,\text{kHz}$), similar to the ones in this work. In contrast to this work, they were able to selectively perform a single shot projective readout (SSR) of the target spin. Hence, they performed two measurements on the target spin, separated by a Ramsey pulse sequence, in order to probe the coherence. During this free evolution, they strongly illuminated the NV center far beyond the saturation of the optical transition, in order for the target spin to be decoupled from electron spin flips as well as changes in charge state by motional averaging. They reached coherence times of above 1 s, at room-temperature. The work in this thesis, however, concentrates on investigating a rather unknown system of one or a few targets. Since selective readout of a single spin, while intending to investigate several, is not feasible, we implemented the hybrid spin sensor, using the ^{14}N spin as a memory. In sec. 3.1.1, the properties of the memory spin were investigated, for the case of different charge states and illumination. The T_1^{mem} time for the negative charge state greatly surpasses the ones during illumination or the neutral charge state. Hence, strong

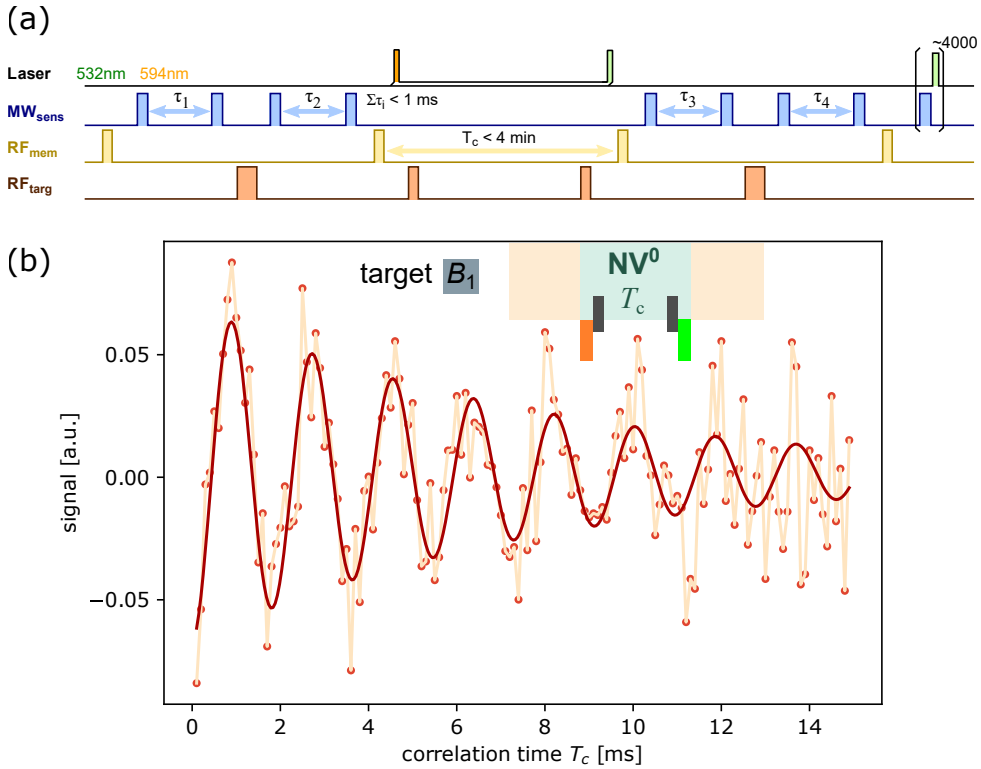

Figure 3.8.: (a) Shows the changed measurement sequence, to allow the probing of the ^{13}C target spin evolution while the NV center is switched to its neutral charge state. The change to fig. 3.2 lies in the application of an orange and green laser pulse before, respectively after the target spin manipulation period. The orange laser pulse ionizes the NV center, while the green laser pulse causes the recombination of NV^0 to NV$^-$. In (b), the Ramsey measurement for target spin B_1 can be seen, with the inset schematic representation of the measurement sequence. The fit of an exponentially decaying oscillation results in a T_2^* time of $T_2^* = (7.8 \pm 1.3)$ ms. The light orange line connects the measurement points, and is meant to guide the eye.

illumination, as shown by Maurer et al. [104], is not feasible, since it degrades the memory. The idea is to continuously reinitialize the electron spin to its $m_s = 0$ state by illuminating the NV center with low power orange laser light ($\lambda = 594\,\mathrm{nm}$).

3.4.1. Target spin T_2^* dependence on illumination power

When looking at eq. 3.25, since we are continuously initializing into $m_s = 0$, the hyperfine interaction $A_{\|}$ is ideally zero. However, two processes stand in the way of "infinite" T_2^*. First, a non-perfect initialization of the electron spin via optical excitation ($P(|0\rangle) \approx 98\%$) still adds small random phases to the superposition state of the target spin upon a spin flip to $m_s = \pm 1$. Second, although illumination at 594 nm has a near optimum ratio between optical excitation rate and ionization rate, the ionization rate increases quadratically with applied power [55]. Intuitively, there will be an optimum excitation power: if it is too low, the excitation degrades the target spin coherence, since it introduces wrongly initialized spin states. At high powers, the NV center gets ionized very fast, which causes decoherence on the target spin (see sec. 3.3) and depolarizes the memory spin. Furthermore, illumination at 594 nm only weakly causes the recombination to the negative charge state, so access to the memory is lost after ionization. The schematic measurement scheme can be seen in fig. 3.9(a). We record Ramsey oscillations for different laser powers (fig. 3.9(b)). The real and imaginary part of the Fourier transformation of the Ramsey signal in the time domain can be seen in fig. fig.3.9(c). The fit reveals a signal lifetime of 17.4 ms (for information on how the fit is performed, see appendix B.3) The qualitative behavior is as expected, with a maximum of the target T_2^* time at reasonable excitation power, see fig. 3.9(d). For target spin A1, a maximum coherence time of $T_2^* = (17.4 \pm 4.3)\,\mathrm{ms}$ is possible, which surpasses the limit set by the NV$^-$ spin T_1^{sens} lifetime.

3.4.2. Modeling the continuously excited system

In order to better understand the processes involved when decoupling the target spin from the NV center by continuous illumination, we expand the two spin model from sec. 3.2.3. For the target spin decoherence due to sensor spin depolarization (for NV$^-$, as well as NV^0), only the electronic ground state was considered. In order to implement the the optical illumination process, we furthermore need to consider the electronic excited state, as well as the metastable singlet state (see sec.1.4). Due to a ionization by two-photon absorption [54, 55], we also need to consider the neutral charge state with its fast fluctuating electron spin state. The complete level scheme can be seen in fig. 3.10. In order to reduce the complexity of the system, we reduce the number of energy levels. Due to the fast decay of the excited state ($\sim$ ns) into the ground or metastable state, it does not have to be considered. Instead, the spin dependent intersystem crossing (ISC) from

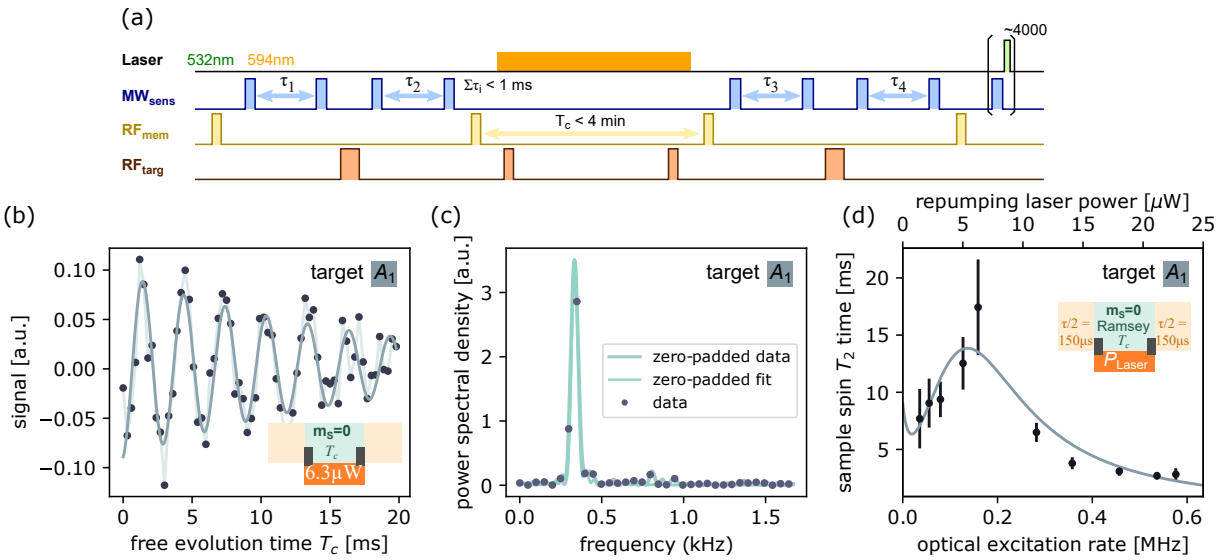

Figure 3.9.: (a) Shows the changed measurement sequence, to allow the probing of the ^{13}C target spin evolution during continuous weak excitation of the NV center. The change to fig. 3.2 lies in the application of a weak orange laser pulse during the target manipulation period. (b) Shows the target spin Ramsey experiment, with an applied orange laser power of 6.3 μW. The signal decays on a timescale of (17.4 ± 4.2) ms. The Fourier transform of the signal can be seen in (c). In addition, the zero-padded signal is shown, as well as the zero-padded fit, which shows an NMR resolution of a single spin of (18.3 ± 4.3) Hz. The dependence of the target T_2^* time on the applied laser power can be seen in (d). The fit is explained in sec. 3.4.2, and results in the conversion ratio between applied orange laser power and optical excitation rate.

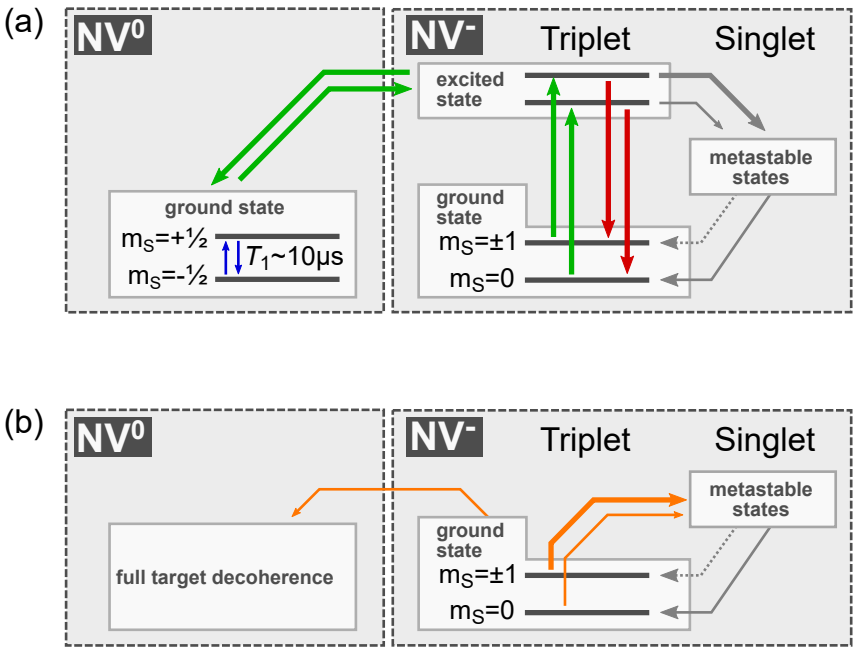

Figure 3.10.: (a) Shows the level scheme of the NV center, which is slightly reduced in complexity to explain the observed effects. The negative charged NV center can be excited with green or orange laser excitation (green lines), and decay by emitting a photon (red lines). The ISC to the singlet state is faster for the $m_s = \pm 1$ sublevels, than for $m_s = 0$. This results in an effective reduction of the fluorescence emitted by the $m_s = \pm 1$ sublevels. The metastable state then decays preferential to the $m_s = 0$ ground state, polarizing the sensor spin. By absorbing a second photon, the NV center can be ionized from its excited state to NV^0, where the $S = 1/2$ electron spin fluctuates on the order of $13\,\mu$s. For (b), the level scheme has been simplified in order to calculate the effect of the continuous excitation on the target spin. The excited state is omitted due to its short lifetime when compared to the sensor target coupling strength. It is replaced by a sensor spin state and excitation power dependent rate to the singlet state. The neutral charge state is implemented as instantaneous target spin decoherence. The thickness of arrows depicts the amplitude of the rate

excited to metastable state is modelled using different optical excitation rates for different $|m_s|$ states. The excitation rates therefore can be written as

$$\gamma_{\text{exc}} = P_{\text{Laser}} \cdot c_{\text{exc}} \tag{3.26}$$

$$\gamma_{\text{exc},m_s=0} = 0.14 \cdot \gamma_{\text{exc}} \tag{3.27}$$

$$\gamma_{\text{exc},m_s=\pm1} = 0.54 \cdot \gamma_{\text{exc}}, \tag{3.28}$$

with the applied laser power P_{Laser}, the laser power to excitation rate conversion factor c_{exc}, as well as the spin state dependent ISC probability 0.14 and 0.54 [47]. The metastable state decays to the triplet ground state with a decay time of 250 ns [47, 63]. In order to include the correct branching from metastable state to triplet ground states with different $|m_s|$ state, a variable branching ratio is implemented

$$\gamma_{\text{meta},m_s=0} = p_{\text{meta},m_s=0} \cdot \frac{1}{250\,\text{ns}} \tag{3.29}$$

$$\gamma_{\text{meta},m_s=\pm1} = \frac{1 - p_{\text{meta},m_s=0}}{2} \cdot \frac{1}{250\,\text{ns}}, \tag{3.30}$$

with the probability $p_{\text{meta},m_s=0} \approx 0.95$ of preferential decay into the $m_s = 0$ sub-level (it should be noted, that this value was fitted to the experimental data due to insufficient prior knowledge in literature). Ionization of the sensor occurs with a rate dependent on the square of the excitation rate

$$\gamma_{ion} = (P_{\text{Laser}} \cdot c_{\text{exc}})^2 \cdot c_{\text{ion}} = \gamma_{\text{exc}}^2 \cdot c_{\text{ion}} \tag{3.31}$$

$$\tag{3.32}$$

with the ionization rate conversion factor c_{ion}. Since ionization in our case means immediate loss of memory access, instead of adding the whole NV^0 subspace, we simulate this by instantaneous decoherence of the target spin. The reduced system can be seen in fig. 3.10(b).

Summarizing, the model incorporates the three unknown empirical values c_{exc}, $p_{\text{meta},m_s=0}$ and c_{ion}. By varying these values and fitting the resulting coherence time of target spin A1 to the experimentally obtained values from fig. 3.9(d), we obtain

$$c_{\text{exc}} = 2.5 \cdot 10^5 \frac{\text{excitations}}{\text{s} \cdot \mu\text{W}} \tag{3.33}$$

$$p_{\text{meta},m_s=0} = 0.96 \tag{3.34}$$

$$c_{\text{ion}} = \frac{1}{7} \cdot 10^{-8} \frac{\text{ionizations}}{\text{excitations}^2}. \tag{3.35}$$

The resulting simulated lifetimes are represented by the continuous line in fig. 3.9.

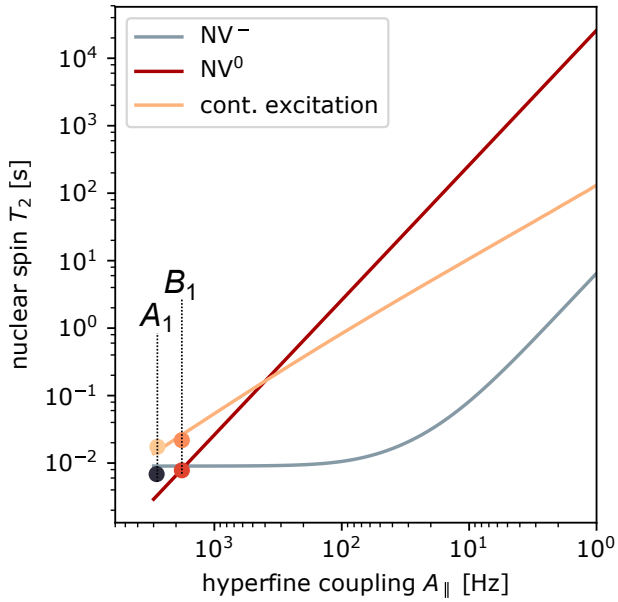

Figure 3.11.: Target spin T_2 time over hyperfine coupling strength with the sensor continuously excited weakly by low power orange laser illumination. The Master equation was solved according to sec. 3.4.2. The scaling for the bare NV$^-$ and NV^0 charge state are shown for comparison. The measurements shown in the previous sections are included as measurement points.

3.4.3. Scaling of the continuous excitation approach with hyperfine coupling strength

Now that a viable model for dissipative decoupling by weak reinitialization of the sensor spin exists, the dependence of the target spin T_2^* on the hyperfine coupling strength $A_\parallel$ can be calculated, as has been done for pure NV$^-$ (fig. 3.6) and NV^0 (fig. 3.7). For a given value for the hyperfine coupling, the dependence of the T_2^* time on the excitation power is calculated. In fig. 3.11, the T_2^* time for the optimum excitation power is plotted against the hyperfine coupling $A_\parallel$. In order to verify these results, we perform T_2^* measurements on target B1 ($A_\parallel = -1.8\,\text{kHz}$), at the optimum excitation power (fig. 3.12). The fit to the data (for information on the fit, see appendix B.3) reveals a coherence time of $(23.8 \pm 2.9)\,\text{ms}$, and hence a linewidth in the Fourier transformed spectrum of $(13.3 \pm 1.6)\,\text{Hz}$.

3.5. Nanoscale nuclear magnetic resonance with chemical resolution

The NV center has been used previously to detect not only nuclear spins intrinsic to, but also outside the diamond [33, 35, 69]. However, except being able to distinguish between different nuclear spin species, e.g. ^{1}H or ^{19}F [36], the achievable spectral resolution was

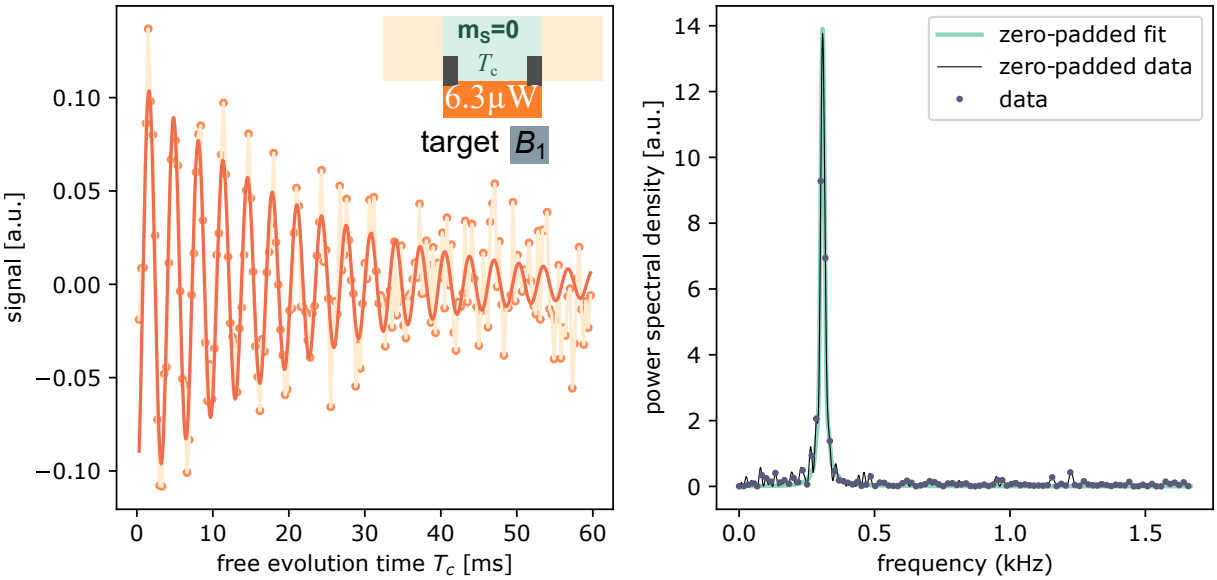

Figure 3.12.: For this measurement, target spin B_1 was used, with a hyperfine coupling of $A_{zz} = -1.8\,\text{kHz}$. (a) Shows the Ramsey experiment with an applied orange laser power of $6.4\,\mu\text{W}$, which should provide optimum performance. The signal decays on a timescale of $T_2^* = (23.8 \pm 2.9)\,\text{ms}$. For (b), the signal was Fourier transformed. The fit reveals a FWHM linewidth of $(13.3 \pm 1.6)\,\text{Hz}$. The measurement sequence is the same as in fig. 3.9(a).

hitherto not sufficient to resolve the chemical structure of the molecules comprising the nuclear spin signal. This structure information can be encoded in the so called chemical shift, or in couplings among different nuclear spins [114–116]. While the coupling between nuclear spins in fluids is quite weak (f)$\sim 10\,\text{Hz}$), the chemical shift is a quantity relative to the Zeeman splitting of the nuclear spins. At the maximum magnetic field of 3 T of the superconducting magnet used in this thesis, the proton Zeeman energy is around 120 MHz, with a corresponding proton chemical shift of up to 13 ppm, or 1.5 kHz.

Even though this chapter introduced the hybrid spin sensor as a means to detect and spectroscopically investigate single nuclear spins, it can be applied readily for the detection of ensembles of spins outside the diamond. The same diamond as described in appendix B.1 was implanted with $^{15}\text{N}^+$ ions with a kinetic energy of 5 keV. By further annealing the crystal at a temperature of 950 °C, NV centers formed close to the surface, with an expected depth of $\sim 10\,\text{nm}$. Samples containing proton and fluorine nuclear spins with adequate chemical shifts were put on the diamond surface, in liquid as well as in solid form.

When increasing the magnetic field to 3 T, the NV center resonance frequency is shifted up to 90 GHz. Since microwave (MW) frequencies that high cannot be transmitted using coaxial cables, hollow MW waveguides are necessary. By employing a hollow waveguide to coplanar waveguide transition [6], the MW field can be spatially confined, to manipulate the NV center electron spins. The NMR transition frequencies of protons and fluorine are

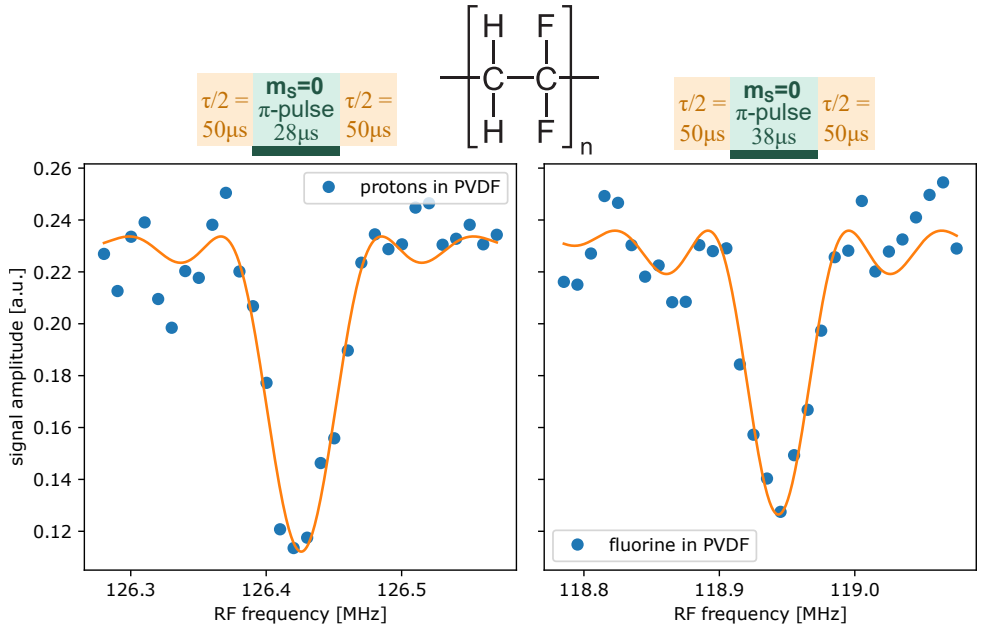

Figure 3.13.: NMR spectra of fluorine and proton spins in PVDF. The measurement sequence is the same as in sec. 3.2. The RF π pulse was performed as fast as possible, resulting in broad lines. Since fluorine and protons spins have the same abundance in PVDF (see inset of the chemical structure), both peaks exhibit the almost same amplitude (small differences are due to the slight difference in the gyromagnetic ratio.)

at around 120 MHz, which can be applied by a 50 μm (or 20 μm) copper wire.

3.5.1. NMR on liquid samples

In order to characterize the nuclear spin sample, a measurement using the implanted NV centers close to the surface was performed, as was in sec. 3.2. The first sample under study was polyvinylidene fluoride (PVDF), a compound containing fluorine, as well as proton nuclear spins. The spectrum of PVDF can be seen in fig. 3.13. Due to the same abundance of proton and fluorine spins, the signal amplitude is almost the same (small differences arise due to the slightly different gyromagnetic ratios).

High spectral resolution, however, is not as easy as with intrinsic ^{13}C nuclear spins. Due to the spatial diffusion of the molecules outside the diamond, the detected nuclear spin bath suffers from additional polarization decay. Two arrangements are made to counteract this effect. First, the compounds used to detect the chemical shift of nuclear spins are very viscous. This slows down the diffusion, and hence the additional polarization decay. Secondly, NV centers deeper inside the diamond are chosen ($\sim 30\,\text{nm} - 50\,\text{nm}$), since the volume they detect is larger. This increases the distance molecules can diffuse, until they are out of detection range, and hence the detection time.

The compound used for proton NMR is liquid polybutadiene. By applying a Ram-

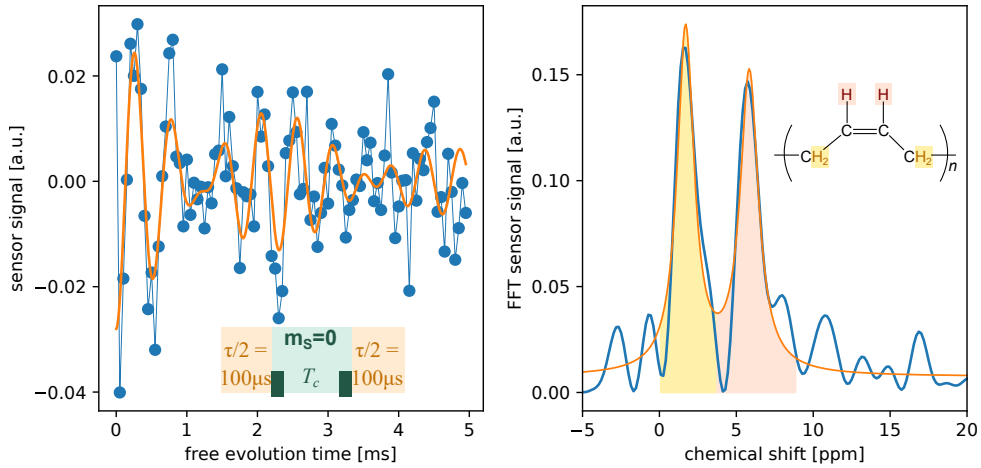

Figure 3.14.: Ramsey measurement on an ensemble of proton nuclear spins in polybutadiene. Left shows the signal oscillations in the time domain, as in fig. 3.5. The oscillation shows a clear superposition of two frequencies. The Fourier transform on the right shows two separate frequencies, corresponding to two differently bound proton spins in the molecule (see inset).

sey detection scheme, as was done in fig. 3.5, the NMR spectrum can be obtained with the highest possible spectral resolution. The measurement can be seen in fig. 3.14. The Fourier transform clearly shows two separate signals stemming from chemically different protons in he polybutadiene molecule, with a splitting of 4.1 ppm, and a frequency resolution of 1.4 ppm.

3.5.2. Versatility of the detection sequence demonstrated on solid state NMR

In order to mitigate the effect of translational diffusion of sample molecules, solid compounds can be used. When observing the decay of the stochastic polarization of protons in poly(ethyl 2-cyanoacrylate) (see fig. 3.15(a)), a slow decay on a timescale of (97.7 ± 9.6) ms is visible. A Ramsey experiment on the solid state spins, however, reveals a drawback of solid state NMR spectroscopy. Due to the fixed relative position of nuclear spins in solids, the dipolar interaction is not averaged out as in liquids, but broadens the resonance lines [120]. In classical solid state NMR, techniques that mitigate this effect exist, e.g. magic angle spinning or homonuclear decoupling sequences. In order to show the versatility of the entanglement based detection sequence and its compatibility with known NMR sequences, we perform the MREV-8 homonuclear decoupling sequence on the solid proton spin sample [120]. It consists of a train of $\pi/2$ pulses around different axis separated by free evolution times, inside the two $\pi/2$ pulses comprising the Ramsey sequence (see fig. 3.16(a)). Due to the effective Hamiltonian that is created by the sequence, the nuclear spin only evolves for a reduced free evolution time $\tau_{\text{red}} = c_{\text{red}} \cdot \tau$, with $c_{\text{red}} = 0.46$ for our

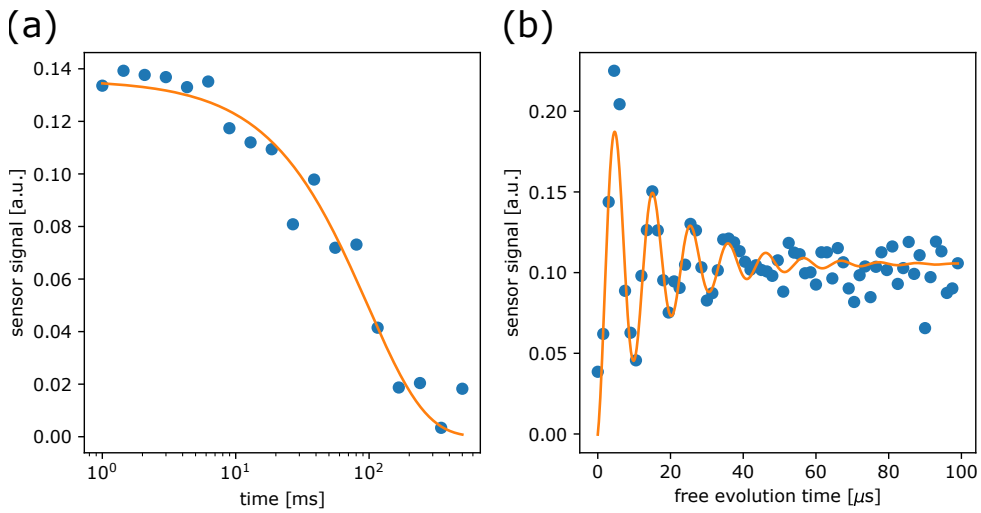

Figure 3.15.: Nanoscale proton NMR on a solid sample. (a) Shows the magnetization decay of proton spins in a solid sample of poly(ethyl 2-cyanoacrylate) on the diamond surface. As expected, the depolarization occurs on a longer timescale than with liquid samples, due to the absence of spatial diffusion of the molecules. In (b), a Ramsey measurement on the proton spins is performed. Contrary to the long T_1 lifetime, it decays on a much smaller timescale of $(16.8 \pm 2.0)\,\mu$s.

experiment[3]. By increasing the number of repetitions of the MREV-8 sequence, the free evolution of the nuclear spins can be observed, unperturbed by their internuclear coupling (see fig. 3.16(b)). The signal, already corrected for the evolution under an average Hamiltonian, consists for 275 μs, and thus around 17 times longer than in the case of the Ramsey sequence. This corresponds to a decrease in linewidth by the same factor, as can be seen in the fast Fourier transform (FFT) in fig. 3.16(b).

3.6. Conclusion

In NMR experiments, due to the weak coupling to the environment, the lifetime of nuclear spins is usually quite long (up to seconds), which enables the analysis of chemical structures of molecules. In NMR experiments with the NV center as a sensor, however, two features limit the achievable spectral resolution. Previous experiments either used dynamical decoupling (DD) sequences to create a spectral filter function for the noise due to stochastic nuclear spin polarization [20, 31, 32] or a correlation spectroscopy approach, where a free evolution period of the nuclear spins induces frequency selectivity [84–86]. The spectral filter function for DD sequences has a FWHM of $1/\tau$, with the total evolution time τ. The resolution is thus limited to $\sim 1/(\pi T_2^{\text{sens}})$. For the correlation spectroscopy, two phase accumulation times, separated by a variable evolution time τ record the tran-

[3]The correction factor depends on the decoupling sequence, as well as the ratio between the duration of the $\pi/2$ pulses and the free evolution times [120].

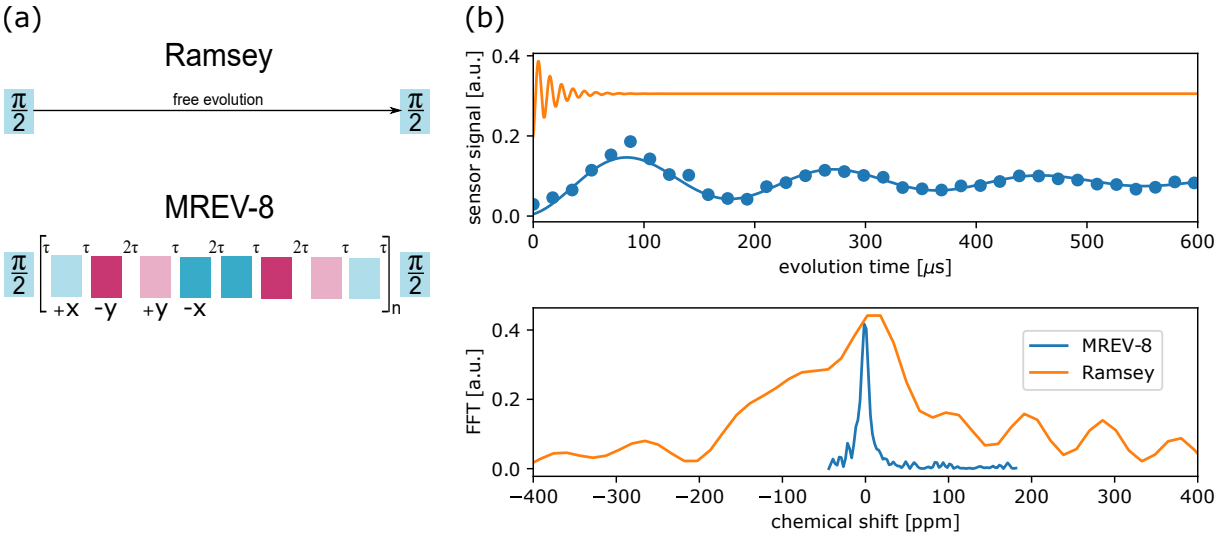

Figure 3.16.: Homonuclear decoupling on a solid sample of proton spins. (a) compares the Ramsey sequence, to the MREV-8 homonuclear decoupling sequence. Here, in addition to the two $\pi/2$ pulses, eight $\pi/2$ pulses of different phase (and thus rotation axis) are performed, separated by waiting times τ and 2τ. This sequence creates an average Hamiltonian for the nuclear spins, where internuclear coupling (i.e. coupling between nuclear spins manipulated by the pulses) is removed, while keeping the evolution due to an external magnetic field, albeit with a correction factor $c_{\mathrm{red}} = 0.46$ (for the experiment done in this work). (b) shows the improvement in coherence time due to the decoupling. The upper panel shows the oscillation of the nuclear spin state over time (blue), with the fit of the Ramsey signal from fig. 3.15(b) as comparison (orange). The lifetime is increased 17-fold to 275 μs

.

sient magnetic field. During the free evolution time, the phase is transferred to the sensor spin polarization. By varying the free evolution time, the time dependent behavior of the magnetic field can be observed. The spectral resolution is thus set by $1/(\pi T_1^{\text{sens}})$. In this chapter, we extend the NV center electron spin sensor to a two spin hybrid quantum sensor. By using the polarization of the nitrogen nuclear spin of the NV center as a memory (as the polarization of the sensor is used in correlation spectroscopy), the spectral resolution can be extended to $1/(\pi T_1^{\text{mem}})$, which is on the order of $\sim 1/4\,\text{min}$ instead of $\sim 1/5\,\text{ms}$. Instead of using SWAP gates between sensor and memory spin [121], we devised a versatile detection sequence that uses entanglement between sensor and memory spin for magnetic field dependent phase accumulation. Using a memory spin furthermore enables the free usage of the sensor spin polarization during free evolution. The hyperfine gradient produced by the sensor can be switched on demand.

The memory spin coherence time T_2^*, however, is limited by dissipative coupling to the sensor spin. When investigating single nuclear spins, the coupling between sensor and target spins has to be significant (at least $\sim 100\,\text{Hz}$). This, however, opens the same dissipative coupling of the target spins to the environment as for the memory spin, thus limiting the target spin coherence time. In this chapter, we use two weakly coupled ^{13}C target spins to demonstrate this effect. Their hyperfine coupling is on the order of $\sim 1\,\text{kHz}$. By either using the neutral charge state of the NV center or continuous weak optical excitation, the deleterious effect of sensor mediated decoherence can be hindered, reaching a target nuclear spin lifetime of $(23.8 \pm 2.9)\,\text{ms}$ and a concomitant spectral resolution of $(13.3 \pm 1.6)\,\text{Hz}$.

The hybrid quantum sensor can also be used for the detection of nuclear spins outside the diamond. NV centers about 40 nm below the surface were created by ion implantation. The transient magnetic field due the statistical magnetization of proton spins in polybutadiene can be detected similar to the magnetization of ^{13}C spins within the diamond. By utilizing the long memory spin lifetime, an NMR spectrum with a resolution of $\sim 100\,\text{Hz}$ could be recorded. The resolution is sufficient to distinguish the signal by protons bound to a sp^3 and a sp^2 hybridized carbon atom. In contrast to the measurement of single ^{13}C spins, the mutual interaction between the sensor and one proton spin is on the order of $\sim 1\,\text{Hz}$. The dissipative coupling thus has no negative effect on the target spin coherence time (see fig. 3.6), even for no decoupling scheme applied. In fig. 3.17 the possible positions of different nuclear spins with a coupling strength of $A_{\parallel} = 1.8\,\text{kHz}$ can be seen, the same coupling as for target spin B1 in this chapter. Thus, a NV center positioned 5 nm below the surface could in principal detect single proton spins (or molecules with multiple, but few proton spins) up to 10 nm above the surface. Under these conditions, the techniques developed in this chapter could be of pivotal importance to gain spectral (and therefore structural) information about said molecule.

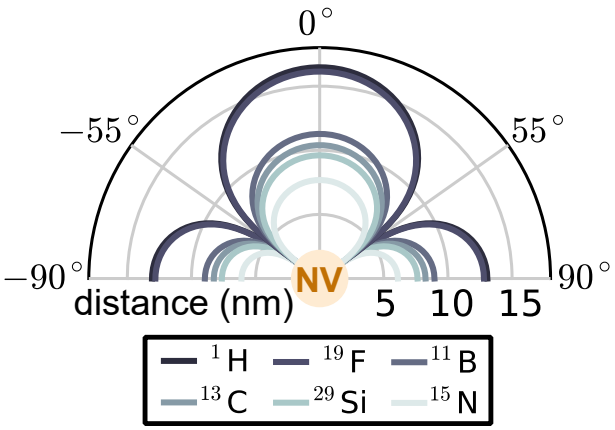

Figure 3.17.: Position of different nuclear spin species with 1.8 kHz coupling to the NV center, the same as for the ^{13}C spin B1 used in this work.

4. High-resolution spectroscopy of single nuclear spins via sequential weak measurements

In the previous chapter, the extraordinary capabilities of the nitrogen-vacancy center (NV center) in diamond as a sensor for nanoscale nuclear magnetic resonance (NMR) were shown. One drawback, however, is the data acquisition time. A measurement as is done in sec. 3.5, usually takes a few hours. As explained in sec. 1.7, measurements of AC magnetic fields with the NV center are performed in-situ, meaning that the read-out of the sensor spin already contains amplitude, as well as frequency information. This means that parameters in the pulse sequence used for detection are varied, and the individual read-out results in dependence on the parameter can be used to reconstruct the unknown signal. For the correlation spectroscopy sequence (see sec. 1.7.6), for example, this means that the free evolution time T between the two dynamical decoupling (DD) sequences is varied. For each value, the measurement is performed repetitively to accumulate a an adequate signal-to-noise ratio (SNR). The total of all measurements $[S(T)]$ then represents the time-evolution of the signal, the spectrum can be obtained by Fourier transform [84–86]. The full width at half maximum (FWHM) of the fourier spectrum can be as good as

$$\delta\nu = \frac{1}{T_{\max}}, \tag{4.1}$$

if not limited by the signal coherence. It can therefore be clearly seen, that for spectral resolutions as achieved in NMR spectroscopy, the free evolution time needs to be increased to $\sim 100\,\mathrm{ms}$. Consequently, the NV center is read out more infrequently, hence drastically increasing the measurement duration.

Recently, heterodyne detection methods using quantum sensors (coined quantum heterodyne detection (Qdyne)) have been developed [122–124]. By synchronizing subsequent measurements with a classical clock (i.e. a device that controls the timing of the experiment), the result of every single read-out can be attributed to one point in time t. By analyzing the measurement results $[S(t)]$, for example by calculating the auto-correlation function or the Fourier transform, the AC magnetic field can be reconstructed. In this chapter, the Qdyne technique is applied to the detection of single target nuclear spins. It

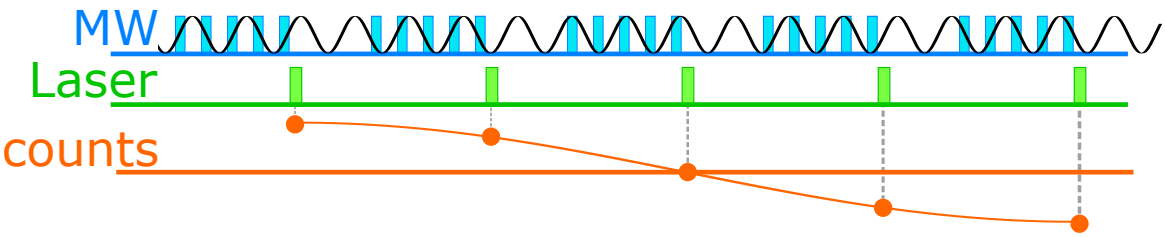

Figure 4.1.: The Qdyne detection scheme to detect oscillating magnetic fields (shown as an oscillating black line). A DD sequence is performed on the NV center electron spin (repeated blue rectangles). The sensor therefore accumulates a phase depending on the frequency, as well as the relative phase between the AC magnetic field and the sequence. This phase is transferred to the sensor spin quantization axis, and read out with a short green laser pulse and fluorescence collection. Subsequent measurements result in slightly different accumulated phases (and thus a different amount of photons), due to the coherent evolution of the AC field in-between measurements. The time evolution of the amount of photons can be used to reconstruct the AC signal with very high precision.

will be shown, that the subsequent measurements of the NV center sensor spin constitute measurements of the target spin with changing basis. To circumvent the resulting stochastic collapse of the spin state of the target spin, we perform weak measurements [125]. A quantum dynamics phase transition from coherent trapping to coherent free evolution is observed when varying the parameters of the measurement. The results in this chapter are published in [5].

4.1. Quantum heterodyne detection of classical magnetic fields

In this section, the basics of the Qdyne methods are demonstrated by detecting an artificially generated oscillating magnetic field. The method is schematically shown in fig. 4.1. By performing DD sequences on the NV center electron spin, it accumulates a phase from an oscillating magnetic field that satisfies the resonance condition

$$f \approx \frac{1}{2\tau}, \tag{4.2}$$

with the DD inter-pulse spacing time τ. The width of the resonance is approximately $\frac{1}{N_p \cdot \tau}$, N_p being the number of π pulses performed in the sequence [33, 83]. While previous measurements summed up the photons from every read-out of the sensor spin, for Qdyne the detected photons are recorded including information about the time of arrival.

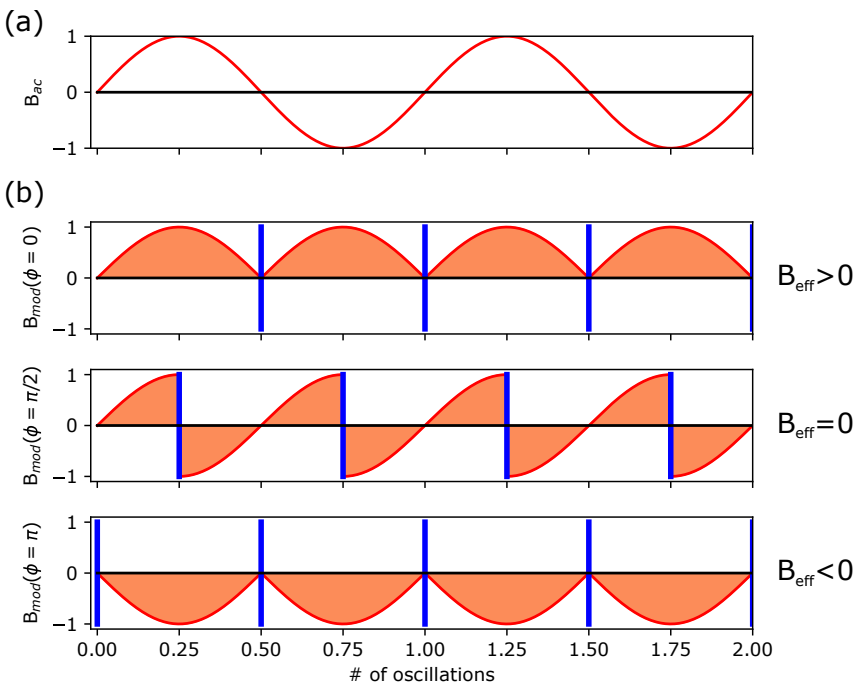

Figure 4.2.: In (a), an exemplary AC magnetic field is shown. This field is transformed to a modulated magnetic field, by the application of a dynamical decoupling sequence on the sensor spin, and inversion of the oscillating field with the π pulses of the sequence. (b) Shows the modulated field B_{mod} for different phases ϕ between the AC magnetic field, and the first π pulse. The blue bars denote the π pulses of the DD sequence. The effective magnetic field (the average magnetic field during the sequence) changes with ϕ.

4.1.1. Phase dependence of AC magnetic field detection

In sec. 1.7.5, the capabilities of DD sequences to detect oscillating magnetic fields were introduced. There, the two $\pi/2$ pulses encapsulating the DD sequence are in phase (hence the rotation of the spin is around the same axis), the detected amplitude is proportional to B_{rms}^2, and therefore not sensitive on the sign of the magnetic field [33, 36]. For the Qdyne detection, however, the DD sequence ends with a $\pi/2$ pulse 90 degree phase shifted to the first one. While the first $\pi/2$ pulse rotates the sensor spin from the $|0\rangle$ to the $|x\rangle = 1/\sqrt{2}\,(|0\rangle + |1\rangle)$ state (rotation about the y-axis), the second pulse rotates the $|y\rangle = 1/\sqrt{2}\,(|0\rangle + i\,|1\rangle)$ state to $|\pm 1\rangle$, and the $|-y\rangle = 1/\sqrt{2}\,(|0\rangle - i\,|1\rangle)$ state to $|0\rangle$. The readout then is

$$\langle \sigma_z \rangle = \frac{1}{2}\sin(\alpha) = \frac{1}{2}\sin\left(\int_0^{n\tau} B_{\text{mod}}(t)dt\right) = \frac{1}{2}\sin(B_{\text{eff}} \cdot n \cdot \tau), \tag{4.3}$$

where α is the quantum mechanical phase that is accumulated during the DD sequence, caused by a modulated magnetic field B_{mod}. This field can be obtained by inverting the sign of the actual oscillating magnetic field with the π pulses of the DD sequence. The effective magnetic field B_{eff} is the time average of the modulated magnetic field B_{mod}. In

fig. 4.2, the connection between the AC magnetic field and the modulated magnetic field are shown, depending on the initial phase ϕ of the oscillating signal

$$B_{\mathrm{AC}} = B_{\mathrm{amp}} \cdot \sin(2\pi f t + \phi), \tag{4.4}$$

with the amplitude of the magnetic field B_{amp}. The effective field can be written as ([122, 123])

$$B_{\mathrm{eff}} = \frac{2B_{\mathrm{amp}}}{\pi} \cos(\phi), \tag{4.5}$$

and the accumulated phase on the sensor spin

$$\alpha = B_{\mathrm{eff}} \cdot n \cdot \tau = \frac{2B_{\mathrm{amp}} n\tau}{\pi} \cos(\phi), \tag{4.6}$$

with the number of π pulses n, and the inter pulse spacing τ. The fluorescence readout then gives

$$\langle \sigma_z \rangle = \frac{1}{2} \sin\left(\frac{2B_{\mathrm{amp}} n\tau}{\pi} \cos(\phi)\right), \tag{4.7}$$

or in the case of small signals

$$\langle \sigma_z \rangle = \frac{1}{2} \frac{2B_{\mathrm{amp}} n\tau}{\pi} \cos(\phi) = \Phi \cos(\phi), \tag{4.8}$$

with the sensor signal amplitude $\Phi = \frac{B_{\mathrm{amp}} n\tau}{\pi}$

4.1.2. Correlations of sequential measurements

In fig. 4.1, sequential measurements of a coherently oscillating magnetic field are shown. Since the individual measurements are performed with a fixed but arbitrary separation in time, they are not synchronized to the detected field. The shift of the phase of the field between two measurements changes the sensor spin expectation value from eq. 4.8

$$\langle \sigma_z \rangle = \Phi \cos(\phi) = \Phi \cos(2\pi f T_m) = \Phi \cos((2\pi f T) \cdot m), \tag{4.9}$$

with T_m being the beginning of the $m+1$ measurement, the iterator m of the measurements, and T the duration of one measurement (including initialization, DD and readout). Consequently, the readout oscillates with the number of measurements, with the abstract frequency

$$f_{\mathrm{m}} = 2\pi f T. \tag{4.10}$$

Since one readout of the sensor spin only results in ~ 0.1 photons and the oscillating field does not necessarily start with phase $\phi = 0$ at the first measurement, we calculate the auto-correlation function of the measurement results R_m

$$C(N) = \langle R_m R_{m+i} \rangle = \sum_m R_m \cdot R_{m+N} \tag{4.11}$$

$$= \sum_m \Phi \cos(2\pi f T m) \cdot \Phi \cos(2\pi f T (m+N)) \tag{4.12}$$

$$= \sum_m \Phi^2 \{\cos(2\pi f T N) + \cos(2\pi f T (2m+N))\} \tag{4.13}$$

$$= m_{\text{total}} \Phi^2 \cos(2\pi f T N) + \sum_m \Phi^2 \cos(2\pi f T (2m+N)). \tag{4.14}$$

If the oscillation is well sampled and the number of total measurements m_{total} is large, the last sum can be set to zero, resulting in

$$C(N) = m_{\text{total}} \Phi^2 \cos(2\pi f T N). \tag{4.15}$$

Even though a single readout of the sensor results in negligible information, an oscillation should be visible in the correlation function.

4.1.3. Spectroscopy on a 3 MHz oscillating signal

In order to prepare the use of Qdyne to detect nuclear spins, it is tested on a classical magnetic field, as in refs. [122, 123]. The experimental setup used in this chapter, including the source of the field can be seen in appendix C.1. Since the highest frequency that can be detected by DD spectroscopy depends on the maximum achievable Rabi frequency

$$f_{\text{max}} \lesssim 2\pi \Omega_{\text{Rabi}}, \tag{4.16}$$

the maximum applicable magnetic field does too. Therefore, the experiments were carried out at a bias magnetic field of $\sim 2500\,\text{G}$. This shifts the ^{13}C Larmor frequency to

$$\nu_0 = \tilde{\gamma}_{^{13}\text{C}} \cdot B_z \approx 10.705\,\text{MHz/T} \cdot 0.25\,\text{T} \approx 2.7\,\text{MHz}. \tag{4.17}$$

The generated AC magnetic field was set to a frequency of 3 MHz, near the expected ^{13}C Larmor frequency, and guided through the same wire as the microwave (MW) radiation used to manipulate the electron spin. The signal generator producing the AC magnetic field was set to a power of 0 dBm, weak enough as to not show any effect in pulsed optically detected magnetic resonance (ODMR) measurements. The inter-pulse spacing was set to 166.6 ns, the duration of one π pulse was 73.57 ns. The correlation function after two million measurements (which took around 15 s), as well as its Fourier transform can be seen in fig. 4.3. The FWHM of the peak can be fitted to be 4 mHz. This corresponds to a

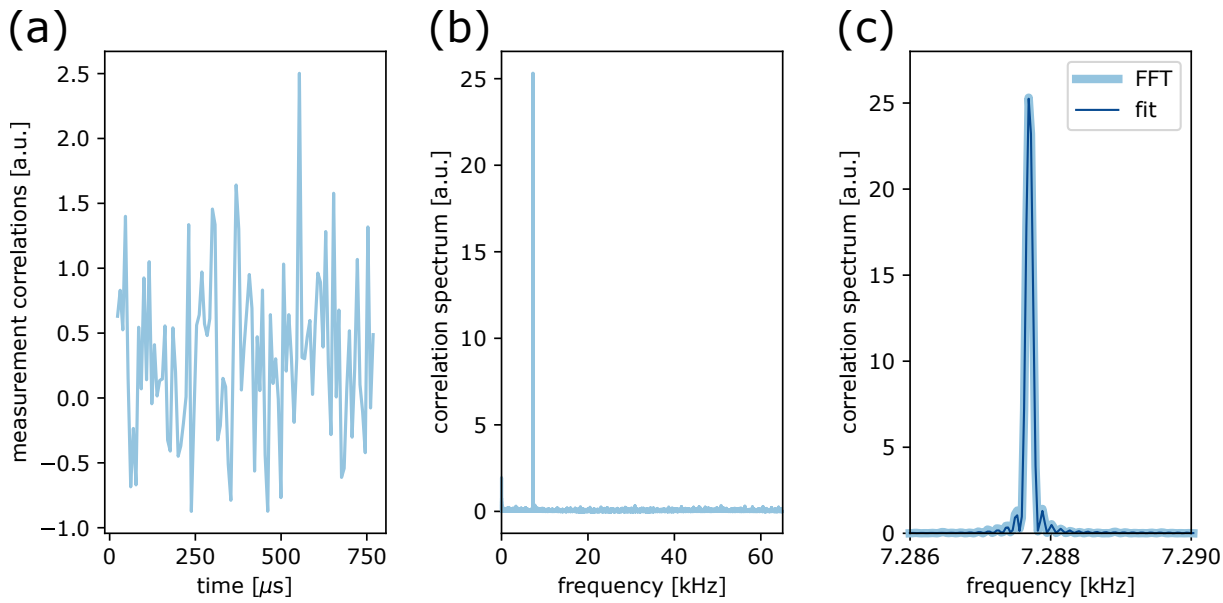

Figure 4.3.: Qdyne measurement of an AC magnetic field. After about 15 s of data accumulation, the calculated auto-correlation function in (a) does not show any clear oscillation (only a small excerpt of the correlation is shown). The Fourier transform thereof, however, shows a clear signal in (b). After zoom-in and fitting, the linewidth of the signal can be determined to be 4 mHz in (c). The fit was done as described in sec. B.3, hence this linewidth is the actual linewidth of the signal, which is broadened by an insufficient signal accumulation time of 15 s in (c).

relative frequency determination accuracy of $\Delta f/f \sim 10^{-9}$, which is on the order of the stability of an oven controlled quartz oscillator (OCXO), which is used as a time base for generating the AC magnetic field.

4.2. From a classical signal to a quantum-mechanical spin

When applying the Qdyne technique for the detection of single spins, the quantum nature of the target needs to be considered. The Hamiltonian of the coupled system is

$$\hat{H} = D\hat{S}_z^2 + \tilde{\gamma}_\mathrm{e} B_z \hat{S}_z + \tilde{\gamma}_{^{13}\mathrm{C}} B_z \hat{I}_z + A_{zz}\hat{S}_z\hat{I}_z + A_{zx}\hat{S}_z\hat{I}_x, \tag{4.18}$$

with the reduced gyromagnetic ratios of the electron and nuclear spin $\tilde{\gamma}_\mathrm{e}$ and $\tilde{\gamma}_\mathrm{n}$, and the hyperfine components A_{zz} and A_{zx}. In the secular approximation, other hyperfine terms can be neglected. One measurement in the Qdyne technique constitutes three distinct building blocks (see fig. 4.4): A dynamical decoupling sequence, a free evolution time and a measurement of the sensor spin state. The DD sequence performs a gate similar to a controlled phase gate (CPHASE gate) on the sensor spin (adding a target spin state

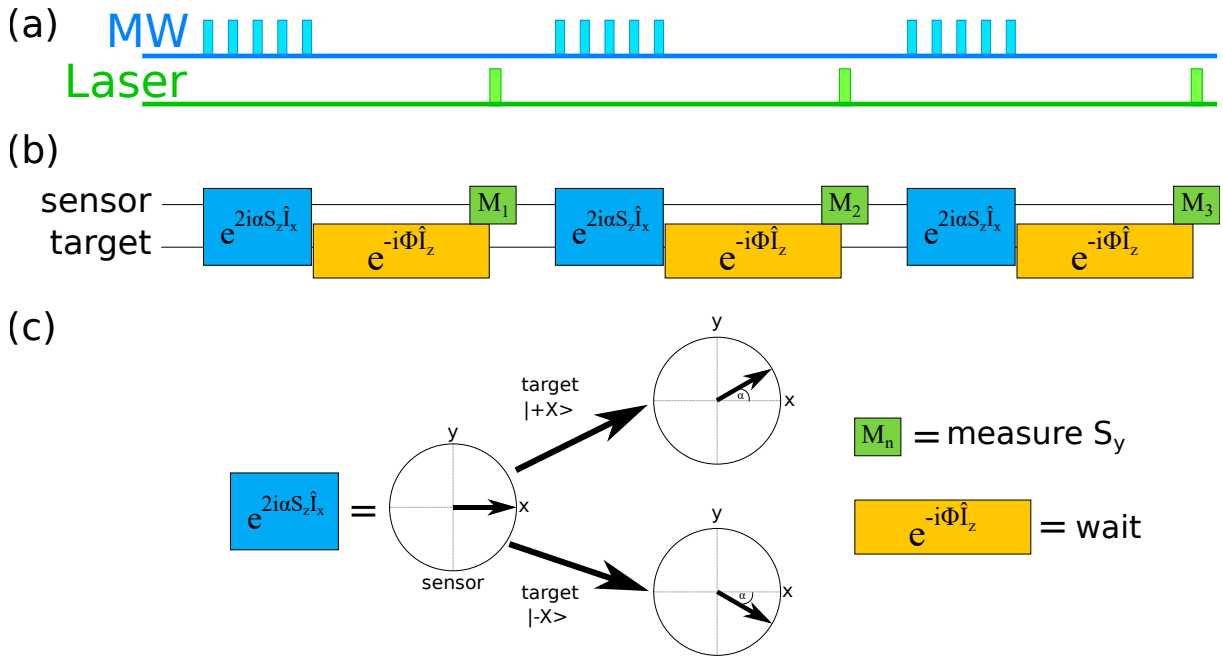

Figure 4.4.: (a) Shows the schematic pulse sequence for the Qdyne technique, as shown in fig. 4.1. In (b) the equivalent quantum mechanical operations performed during the sequence on the target spin are shown. It consists of a repetition of a CPHASE gate (blue), free evolution of target spin (orange) and sensor readout (green). (c) The CPHASE gate rotates the sensor spin state around the z-axis, dependent on the target spin state ($|-X\rangle$ or $|+X\rangle$), the free evolution is implemented by waiting, and the measurement is performed of the y-component of the sensor spin (by performing a $\pi/2$ pulse around the x-axis prior to laser excitation and fluorescence collection).

dependent phase on the sensor spin state)[1] (see refs. [20, 31, 32, 126]).

$$\hat{U}_{\mathrm{DD}} = e^{2i\alpha\hat{S}_z\hat{I}_x}. \tag{4.19}$$

Between the end of one DD sequence, and the beginning of the next, the target spin undergoes free evolution according to

$$\hat{U}_{\mathrm{free}} = e^{i\Phi\hat{I}_z}, \tag{4.20}$$

with the phase shift $\Phi = 2\pi\bar{\nu}t$ and the hyperfine modified Larmor frequency

$$\bar{\nu} = \nu_0 + A_{zz}/2. \tag{4.21}$$

It should be noted, that the time t should encompass the complete time between two measurements. In addition to the actual readout time, the free evolution can be prolonged at will, therefore setting Φ. The scheme of the measurement can be seen in fig. 4.4. Starting

[1] A CPHASE gate nominally adds a phase of π, while the gate introduced here adds a variable phase α.

with a sensor spin initialized to $|x\rangle$, and the target spin in an arbitrary superposition $|\phi\rangle = a\,|{+X}\rangle + b|{-X}\rangle$, the DD sequence transforms the state to

$$|\phi\rangle = (a\,|{+\alpha}\rangle \otimes |{+X}\rangle) + (b\,|{-\alpha}\rangle \otimes |{-X}\rangle)\,, \tag{4.22}$$

with $|{\pm\alpha}\rangle = e^{i\pm\alpha\sigma_z}\,|x\rangle$. Especially, for $\alpha = \pi/2$, $|{\pm\alpha}\rangle = |{\pm y}\rangle$. The sensor spin is then measured along the y-axis (measurement of $\hat{S}_y$). The probabilities of the two measurement outcomes $R_m = \pm 1$ depend on the complex amplitudes a and b of the initial nuclear spin state, and therefore constitutes a measurement of $\hat{I}_X$. For $\alpha = \pi/2$, the state is

$$|\phi\rangle = (a\,|{+y}\rangle \otimes |{+X}\rangle) + (b\,|{-y}\rangle \otimes |{-X}\rangle)\,. \tag{4.23}$$

Therefore, a measurement of the sensor spin along the y axis, measures the target spin projectively along the X axis. Afterwards, the target spin is consequently in the state $|{\pm X}\rangle$, depending on the measurement outcome $R_m = \pm 1$. Due to the free precession between two measurements, the resulting state rotates around the Z-axis by an angle Φ. For $\Phi = \pi/2$ and $\alpha = \pi/2$, the target spin is consequently always measured in a basis shifted by $\pi/2$ to its initial state. Since measurements along these basis do not commute, subsequent measurement results are uncorrelated. For $\alpha < \pi/2$, the target spin state after the measurement can be obtained by projection of the state from eq. 4.22 onto the sensor spin basis state corresponding to the measurement result $R_m = \pm 1$

$$|\phi\rangle_m = |{\pm y}\rangle\,\langle{\pm y}|\,|\phi\rangle\,. \tag{4.24}$$

The target spin state is therefore rotated by an angle $\pm\alpha$, depending on the measurement result R_m. This effect is called measurement back-action.

For the limit $\alpha \to 0$ of very weak measurements, and therefore no measurement induced dephasing of the target spin state, the correlation of two measurements becomes

$$C(N) = \langle R_m R_{m+N}\rangle = \sin^2\alpha\cos(N\Phi), \tag{4.25}$$

similar to eq. 4.15. In this case, the spin precession frequency Φ (in units of angle per measurement) can be determined without influence of the measurement. By taking the measurement back-action into account, we obtain the general form of the correlation function

$$C(N) = \sin^2\alpha\left(C_+\eta_+^N + C_-\eta_-^N\right)/2, \tag{4.26}$$

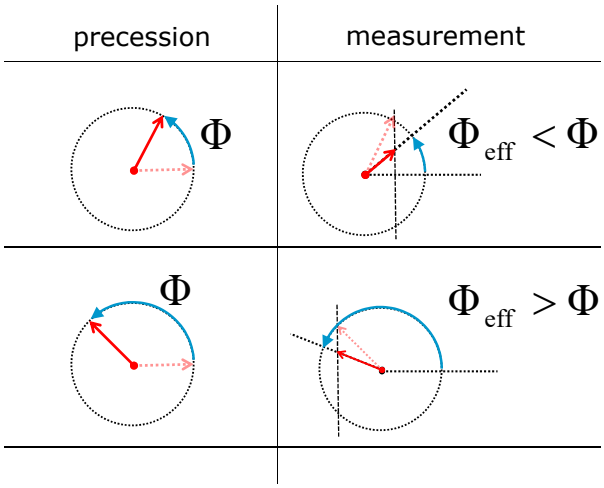

Figure 4.5.: Schematic representation of the frequency drag effect due to sequential weak measurements. In the precession stage, the target rotates from an initial state (faint red arrow), to a final state (red arrow) by an angle Φ. The measurement on the sensor spin (right column) then projects the target from the state represented by the faint red arrow onto the state represented by the red arrow. As can be seen, the effective rotation Φ_{eff} differs from the actual precession Φ. Φ_{eff} is smaller than Φ for $\Phi < \pi/2$, and larger for $\Phi < \pi/2$.

with

$$C_{\pm} = 1 \pm \frac{\mu \cos(\Phi)}{\sqrt{\mu^2 \sin^2 \Phi}} \tag{4.27}$$

$$\eta_{\pm} = \left(\cos \Phi \pm \sqrt{\mu^2 - \sin^2 \Phi}\right) \cos^2 (\alpha/2) \tag{4.28}$$

$$\mu = \tan^2(\alpha/2), \tag{4.29}$$

where μ can be regarded as the measurement strength (for $\alpha \leq \pi/2$). The derivation is performed in appendix C.2. The behavior of the correlation function can be separated in two regimes, depending on μ. For $\mu^2 < \sin^2 \Phi$, the measurement can be regarded as weak. The correlation function decays with an effective decay of

$$\gamma_{\text{eff}} = -\frac{1}{2} \ln(\cos \alpha) \tag{4.30}$$

per measurement cycle. Since this decay only acts along the Y-axis, the correlation function oscillates with an effective frequency

$$\Phi_{\text{eff}} = \arccos \frac{\cos \Phi}{\sqrt{1 - \mu^2}}. \tag{4.31}$$

Therefore, depending on the angle Φ being smaller or larger than $\pi/2$, the oscillation frequency is either dragged towards 0 or π. This behavior is shown schematically in fig. 4.5.

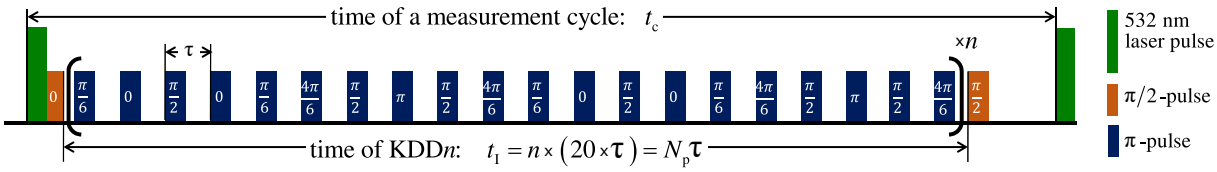

Figure 4.6.: Pulse representation of one measurement in the Qdyne scheme. The dynamical decoupling sequence used is Knill dynamical decoupling (KDD) [132]. The orange rectangles represent $\pi/2$ pulses, the respective inset denotes the axis of rotation. The first $\pi/2$ pulse rotates the sensor spin from its $|0\rangle$ state to the x-axis. The second $\pi/2$ pulse rotates the $|\pm y\rangle$ states of the sensor to its quantization axis. The blue rectangles denote π pulses, with the inset again representing the axis of rotation. One iteration of KDD consists of 20 π pulses, and can be repeated to an overall pulse number $20 \cdot n$.

For a rather strong measurement, $\mu^2 > \sin^2\Phi$, the correlation function is an exponential decay for $\cos\Phi > 0$, or an exponential decay with alternating sign for $\cos\Phi < 0$

$$\cos\Phi > 0 \rightarrow C(N) \propto e^{-N\gamma_{\text{eff}}} \tag{4.32}$$

$$\cos\Phi < 0 \rightarrow C(N) \propto (-1)^N e^{-N\gamma_{\text{eff}}} \tag{4.33}$$

In this case, the effective decay is

$$\gamma_{\text{eff}} = \min\left(-\ln|\eta_+|, -\ln|\eta_-|\right) \approx \frac{\sin^2\Phi}{2\tan^2(\alpha/2)}. \tag{4.34}$$

The spin is trapped along the X-axis, similar to the quantum Zeno effect [127, 128].

At $\mu^2 = \sin^2\Phi$ there is a phase transition between coherent oscillation and coherent trapping, due to the competition between free precession and measurement-induced dephasing [127–131].

4.3. Correlations of sequential weak measurements

In order to perform Qdyne detection on a single nuclear spin, we resort to the diamond sample used in the previous chapter (see appendix B.1). The isotopical enrichment of ^{12}C to 99.995% again causes a sparse ^{13}C environment, with single detectable target nuclear spins with coupling strengths of $\sim$ 1 kHz. All experiments are carried out at room-temperature, limiting the longitudinal relaxation time of the sensor spin to $\sim$ 5 ms. In fact, the T_1 time for this diamond sample is only around 2 ms, shorter than the relaxation time usually observed with single, non-implanted NV centers (see appendix C.3). We apply a static magnetic field along the N-V direction of the NV center of 2561 G, and choose the $|m_s = 0\rangle$ and $|m_s = -1\rangle$ subspace as the sensor qubit. Initialization in the state $|+x\rangle$ is done by initializing in $|m_s = 0\rangle$ and a subsequent rotation of $\pi/2$ around the

y axis. Due to the high Larmor frequency of the ^{13}C nuclear spins, and the small coupling, we chose the Knill dynamical decoupling (KDD) sequence [132], since it is robust against pulse errors. It consists of 20 equally spaced π pulses. The KDDn sequence therefore consists of $N_p = 20 \cdot n$ π pulses, and a total interaction time of $t_I = N_p \cdot \tau$. Analogous to the initialization, read-out of the sensor spin along the y-axis is done by a rotation of $\pi/2$ around the x-axis, and subsequent optical excitation and fluorescence readout. The collected photons are recorded corresponding to the index of the readout. As introduced in the previous section, each measurement can be described by two parameters: the free evolution Φ between two measurements, and the measuremen strength $\mu(\alpha)$. In the case of large external magnetic fields (compared to the coupling between sensor and target), the free evolution is

$$\Phi \approx (2\pi \left|\tilde{\gamma}_{^{13}\mathrm{C}} B_z - A_{zz}\right| t_c) \mod 2\pi, \tag{4.35}$$

with the cycle duration t_c. The conditional phase shift (and hence the measurement strength) is

$$\alpha \approx \frac{2A_{zx}}{\bar{\nu}} \left| \frac{\sin(N_p \pi \bar{\nu} \tau)}{\cos(\pi \bar{\nu} \tau)} \right| \sin^2\left(\frac{\pi \bar{\nu} \tau}{2}\right). \tag{4.36}$$

and especially if the DD sequence pulse spacing $\tau = \frac{1}{2\bar{\nu}}$

$$\alpha \approx 2N_p A_{zx} \tau = 2A_{zx} t_I \tag{4.37}$$

(see ref. [20, 31, 32, 126, 133]). The free evolution can be varied by adding a dead time before the readout laser pulse, as can be seen in fig. 4.6. By repeating the 20 π pulses of the DD sequence, the number N_p of the pulses and therefore the measurement strength can be varied.

4.3.1. Looking for a suitable ^{13}C candidate

We start off by looking for a NV center with a suitable ^{13}C spin in its environment. The ^{13}C Larmor frequency is derived of the NV center ODMR transition frequency to be $\nu_0 = 2.743\,189\,\mathrm{Hz} \pm 4\,\mathrm{Hz}$. We set the KDD inter pulse spacing to be $\tau = 1/(2\nu_0)$. A Qdyne measurement sequence with 40 to 200 π pulses is run on several NV centers until one showing a correlation signal is found. The phase shift of the free evolution (calculated by the assumed Larmor frequency ν_0) was set to $\Phi = \pi/2$. Around one in five NV centers searched show a visible correlation signal, as can be seen in fig. 4.7. In this case, the observed frequency of the correlation signal slightly deviates from the expected one, as it should oscillate with $\Phi/(2\pi)$. In order to determine the exact resonance frequency, the Qdyne measurement is repeated with slightly varying τ, with the nominal phase shift

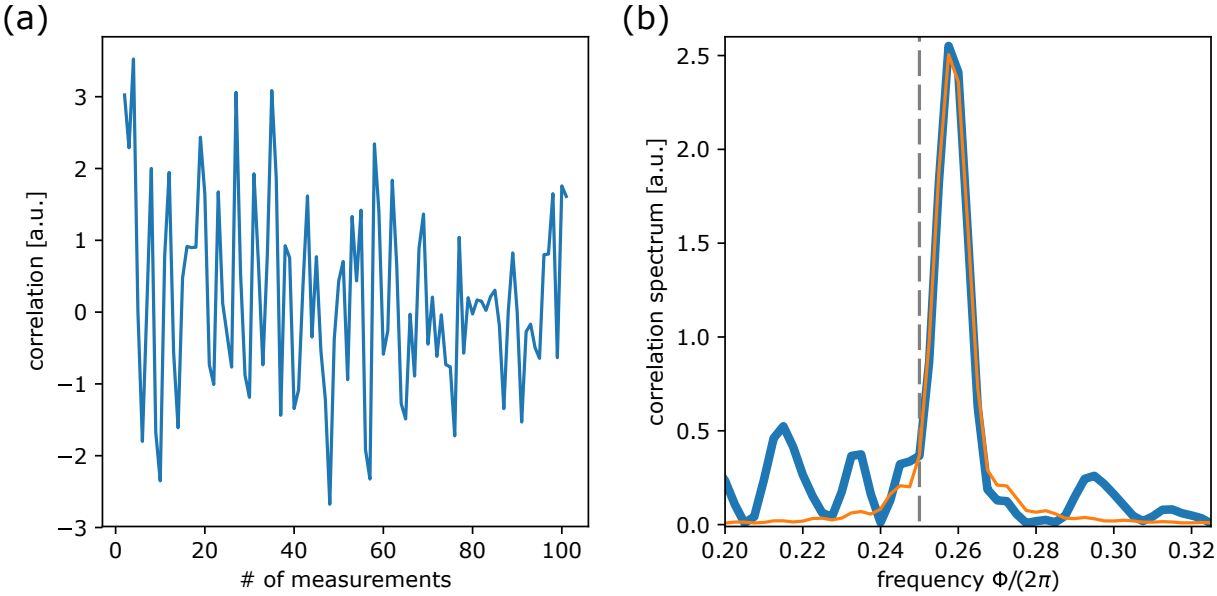

Figure 4.7.: (a) Correlation signal of sequential weak measurements on a ^{13}C target spin. The evolution time was calculated to induce a nominal shift of the target spin state by $\Phi_{\text{nom}} = \pi/2$ between two measurements, by assuming the bare ^{13}C Larmor frequency. The Fourier transform in (b) shows a clear deviation of the signal from the expected value ($\Phi/(2\pi) = 0.25$, denoted with a gray dashed line). This can be explained by a small detuning between the resonance frequency and the DD sequence due to hyperfine coupling between sensor and target.

Φ_{nom} set to be $\pi/2$ by choosing t_c according to $\Phi_{\text{nom}} = (\frac{\pi t_c}{\tau}) \mod 2\pi$. The results can be seen in fig. 4.8. The linear fit returns the resonance $\bar{\nu} = 2.743\,04\,\text{MHz}$, where the observed oscillation frequency indeed is $\Phi = \Phi_{\text{nom}} = \pi/2$.

4.3.2. Varying the measurement strength

Next, the dependence of the measurement back-action on the measurement strength is examined. We set the DD sequence resonant to the the ^{13}C nuclear spin, with an inter pulse spacing of $\tau = 0.182\,28\,\mu\text{s}$. In figure 4.9(a,b), the correlation results from two sets of measurements are shown. For (a), the DD sequence performed was KDD2, hence 40 π pulses were performed. In (b), a KDD5 sequence was used. When comparing the two measurements, two things are apparent: For weaker measurements, the signal amplitude is smaller (~ 0.05 compared to ~ 0.2), however, the decay in units of number of measurements is smaller. The results can be fitted by using eq. 4.26 in conjunction with eqs. 4.35 and 4.37. They can be reproduced by having a perpendicular target spin hyperfine coupling of $A_{zx} = 16\,\text{kHz}$. In retrospect, the state dependent phase accumulation of the sensor spin can be determined to be $\alpha = 0.0743\pi$ for KDD2, and $\alpha = 0.189\pi$ for KDD5. The precession frequency $\bar{\nu}$ can be determined by the fitted frequency in the Fourier transform of the correlation signal (fig. 4.9(c,d)). Since the measurement rate $\gamma_{\text{m}} = 1/t_c$

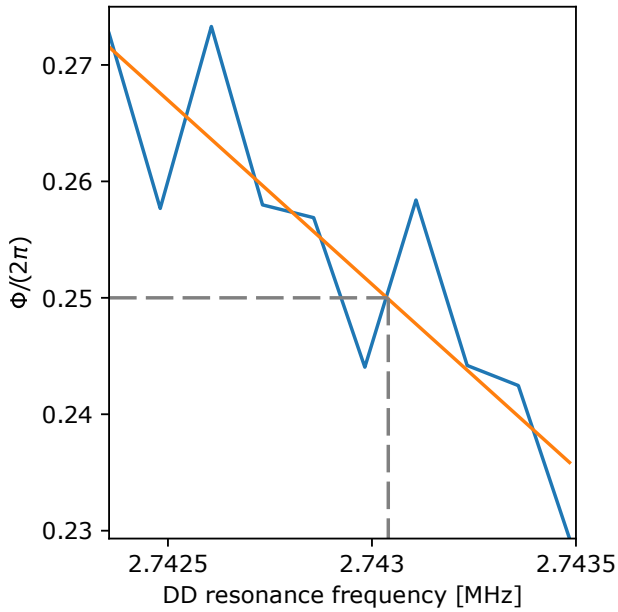

Figure 4.8.: Determination of the exact hyperfine modified Larmor frequency $\overline{\nu}$. The Qdyne measurement from fig. 4.7 was performed for different values of the DD inter-pulse spacing τ. The free evolution time after the DD sequence was chosen independently for every value of τ, to induce a nominal phase shift $\Phi_{\text{nom}} = (\frac{\pi t_c}{\tau}) \mod 2\pi = \pi/2$. The frequency $\Phi/(2\pi)$ of the measurement correlations (compare fig. 4.7(b)) are plotted over the DD resonance frequency $1/(2\tau)$. For a value of 2.743 04 MHz, the frequency of the measurement correlations equals the nominal value, $\Phi = \Phi_{\text{nom}}$, and therefore constitutes the exact resonance.

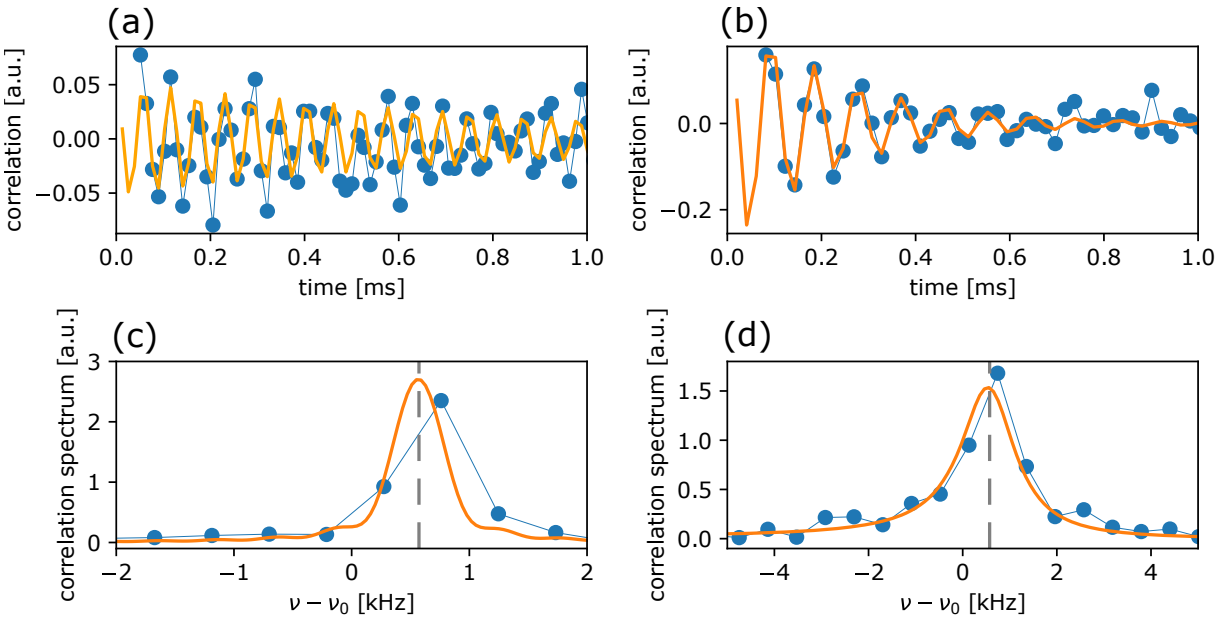

Figure 4.9.: (a) Shows the correlation of sequential weak measurements, with a KDD2 sequence as DD (blue dots, connected via a faint blue line for better visibility). The inter pulse spacing was set resonant to $\bar{\nu}$ (see fig. 4.8). The phase shift between two measurements was set to $\Phi \approx 0.44\pi (= 80°)$. (b) Is the same experiment, but with a KDD5 decoupling sequence. (c,d) Show the Fourier transform of the respective signal from (a,b). The frequency axis is referenced to the bare ^{13}C Larmor frequency (dashed gray line). Both measurements were fitted with eq. 4.26. The signal frequency $\bar{\nu}$ is shifted from the ^{13}C Larmor frequency by $A_{\parallel}/2 = 0.571\,\text{kHz}$.

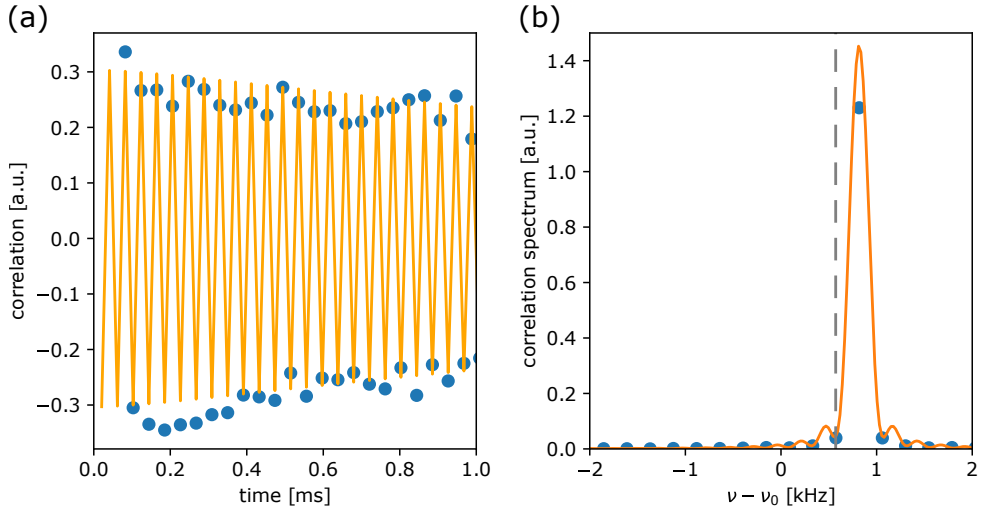

Figure 4.10.: (a) Shows a measurement similar to fig. 4.9(b), but with a free evolution time between measurements chosen to induce a phase shift of $\Phi = 0.989\pi$. For these parameters, the sequential measurements lock the target spin along the measurement axis, resulting in a slower decay of the correlation signal. Furthermore, as can be seen in (b), the signal frequency is shifted from the resonance frequency $\bar{\nu}$ (dashed gray line).

($\sim$ kHz) is much smaller than the actual Larmor frequency ($\sim$ MHz), the oscillation of the spin is strongly undersampled and appears at the frequency

$$\bar{\nu}_{\mathrm{us}} = \bar{\nu} \mod \gamma_{\mathrm{m}} \tag{4.38}$$

This ambiguity can be lifted by taking the spectral filtering of the DD sequence into account [122]. By this, the hyperfine modified precession frequency can be determined to be $\bar{\nu} = 2.743\,760\,\mathrm{MHz} = \nu_0 + 0.571\,\mathrm{kHz}$, with the bare ^{13}C Larmor frequency ν_0. From that, and eq. 4.21, the parallel hyperfine component can be determined to be $A_{\parallel} = 1.144\,\mathrm{kHz}$.

In fig. 4.10(a), compared to figs. 4.9(a,b), a phase shift of $\Phi = 0.989\pi$ was chosen. This tunes the system to the quantum Zeno regime described in eq. 4.32. As can be seen in the Fourier transform of the correlation signal (fig. 4.10(b)), the correlation signal is observed at a frequency of $\Phi_{\mathrm{eff}=}1/(2t_c)$ (an alternating signal). It is shifted by 246 Hz from the previously observed hyperfine modified Larmor frequency $\bar{\nu} \mod 1/t_c$ (see the difference between the dashed gray line and the peak fit in fig. 4.10(b)). This means, that the weak measurements coherently lock the spin along the measurement axis, mitigating its inherent precession in-between, similar to the quantum Zeno effect [127, 128].

4.4. Quantum dynamics phase transition

In this section, the phase transition in the quantum dynamics of the repetitively measured system is examined. As introduced in sec. 4.2, the correlation signal of sequential weak measurements undergoes a phase transition from coherent oscillation to coherent trapping at the boundary

$$\tan^4(\alpha/2) = \sin^2 \Phi. \tag{4.39}$$

In fig. 4.11(a), the observed frequency Φ_{eff} of the correlation function is plotted in dependence on the parameters Φ and α, according to eq. 4.31. Measurements were performed along the inset blue and orange lines, corresponding to the measurement strengths from sec. 4.3.2, $\alpha = 0.189\pi$ and $\alpha = 0.0743\pi$, respectively. The observed oscillation frequency of the correlation signal, depending on the free evolution Φ between two measurements is plotted in fig. 4.11(b). The frequency drag when approaching $\Phi = \pi$ is clearly visible, with a stronger effect for the higher measurement strength. Three different regimes can be observed: Small Φ results in an oscillation $\Phi_{\text{eff}} = \Phi$ as expected by the free evolution of the spin. A Φ chosen according to eq. 4.39 causes the effective frequency Φ_{eff} to be dragged away from Φ. When further approaching $\Phi = \pi$ (or $\phi = 0$, for that matter), the effective frequency $\Phi_{\text{eff}} = \pi$ becomes independent of Φ. The spin is therefore trapped by the measurement. Yet another view on the phase transition is given by the effective decay γ_{eff} of the correlation signal. It can be deduced from the spectral width of the correlation signal according to

$$\delta\nu = \frac{\gamma_{\text{eff}}}{2\pi t_c} \tag{4.40}$$

As can be seen in fig. 4.11(c,d), it behaves according to eqs. 4.30 and 4.34.

4.5. High resolution spectroscopy enabled by repetitive readout

For NMR spectroscopy, high spectral resolution is important for the identification of chemical structures in molecules [114–116]. When relying on the Qdyne technique for high resolution NMR on single or few spins, two obstacles were shown in sec. 4.3. First, while increasing the interaction time between sensor and target spins increases the observed signal, it also increases the dephasing due to measurement back-action. This results in broader spectral lines. Furthermore, the observed precession frequency of the target spins can be altered by the measurement. This effect might obscure frequency shifts due to the chemical environment and is therefore unwanted. In order to perform NMR measure-

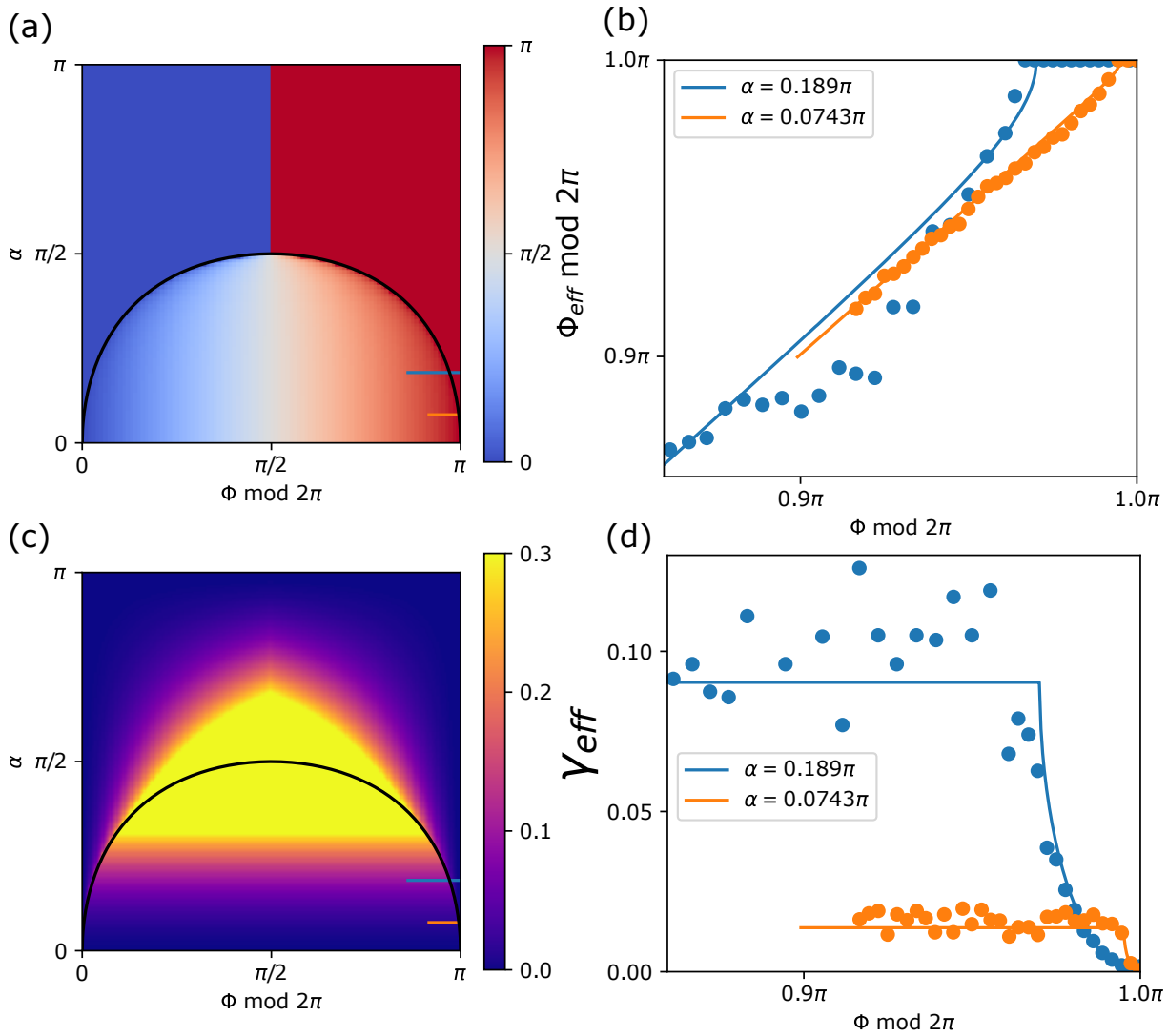

Figure 4.11.: The phase transition between coherent oscillation and quantum Zeno effect in a sequentially measured quantum system can be visualized in two different ways. (a) Shows the calculated observed oscillation frequency Φ_{eff} dependent on the phase shift Φ between measurements, and the measurement strength α. The phase boundary is shown by a black line. In (b) two measurement series are shown, for two different measurement strengths of $\alpha = 0.189\pi$ and $\alpha = 0.0743\pi$ (the measurement range is shown by the blue and orange inset lines in (a)). For every value of Φ, a Qdyne measurement was performed, and the oscillation frequency determined via fitting. The frequency drag effect is stronger, for a higher measurement strength. In (c), the effective decay of the correlations of subsequent measurement is used as a parameter to visualize the phase transition. It is calculated according to eqs. 4.30 and 4.34. In (d), the decay of the measured correlations from (b) was extracted from the fit and plotted over the phase shift Φ. As expected, the decay goes to zero, when the precession of the target spin between two measurements goes towards π.

ments on single spins, the approach seems straightforward: Decrease α, while choosing $\Phi \approx \pi/2$. One problem, however, that arises with decreasing measurement strength is the low correlation signal amplitude (see eq. 4.25). Since the infidelity of the spin readout is not considered in the theoretical derivation of the correlation function, the amplitude is further reduced when it is read out with a single laser pulse at room-temperature (see sec. 1.4).

In sec. 1.8, the usability of the nitrogen nuclear spin as a memory spin for readout enhancement was introduced. Since the memory spin state is not altered by the optical readout of the sensor spin, transferring the spin state from sensor to memory enables repetitive readout of the information. In ref. [15], a high magnetic field increased the lifetime of the memory spin under continuous readout so far, that single-shot readout was feasible, providing the maximum amount of information possible by a quantum measurement. This can then not only be used to read out the spin, but also to initialize it by subsequent post-selection. For the use with Qdyne detection, this is not feasible. The magnetic field used in the experiment is quite low, which strongly reduces the readout fidelity. Furthermore, the stochastic initialization of the memory by post selection renders many measurement runs useless. The most important reason, however, is the influence of optical excitation on the coherence of target spins [4, 104]. It is known from the previous section, that the target spins under study are only slightly influenced by optical excitation of the NV center however, this might change due to the increased excitation rate near saturation of the optical transition.

In ref. [134], a similar technique was developed, which can be used with an arbitrary number of readouts of the memory spin. By algorithmic initialization of the nitrogen nuclear spin, the necessity for a high fidelity, single-shot readout is not necessary. The initialization of the memory spin that is performed prior to every measurement in the Qdyne sequence can be seen in fig. 4.12(a). The optically initialized state of the sensor spin is transferred to the memory spin, leaving the memory spin in an eigenstate, while the sensor spin is mixed. Subsequent optical excitation reinitialized the sensor spin, while only causing negligible depolarization on the memory spin. Due to insufficient charge state initialization (see sec. 1.3), the procedure is done twice. After interaction between sensor and target spin via a DD sequence, the polarization of the sensor spin is transferred to the memory spin, which is then read out 40 times[2] (see fig. 4.12(b)).

For this experiment, the NV center used was changed and the ^{13}C Larmor frequency was measured with very high precision, with the method described in sec. 3. The result can be seen in fig. 4.13. A Lorentzian fit determines the ^{13}C Larmor frequency to be $\nu_0 = 2.740\,134\,\mathrm{MHz} \pm 0.39\,\mathrm{Hz}$.

The Qdyne correlation signal is shown in fig. 4.14(a,b) for two different measurement strengths (KDD5 and KDD10). Even though the correlation seems to decay quite rapidly

[2]This value was chosen empirically

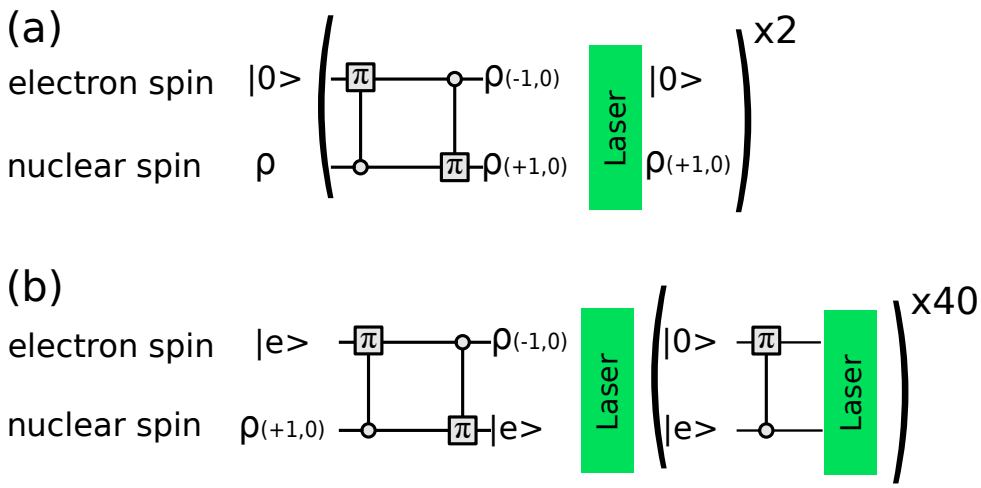

Figure 4.12.: (a) Pulse scheme for deterministic initialization of the nitrogen nuclear spin qubit. In order to transfer polarization from the initialized electron spin, a gate consisting of two CNOT gates is performed. This initializes the ^{14}N nuclear spin in its $m_i = 0$ and $m_i = +1$ manifold. A green laser pulse then reinitializes the electron spin to its $m_s = 0$ state. The whole procedure is repeated, due to insufficient charge state initialization of the NV center after a green laser pulse. (b) Pulse scheme for repetitive readout of the electron spin. Similar to the initialization, the electron spin state is transferred to the nuclear spin state after the dynamical decoupling sequence. Afterwards, a CNOT gate is performed on the electron spin, with subsequent readout. This procedure is repeated 40 times.

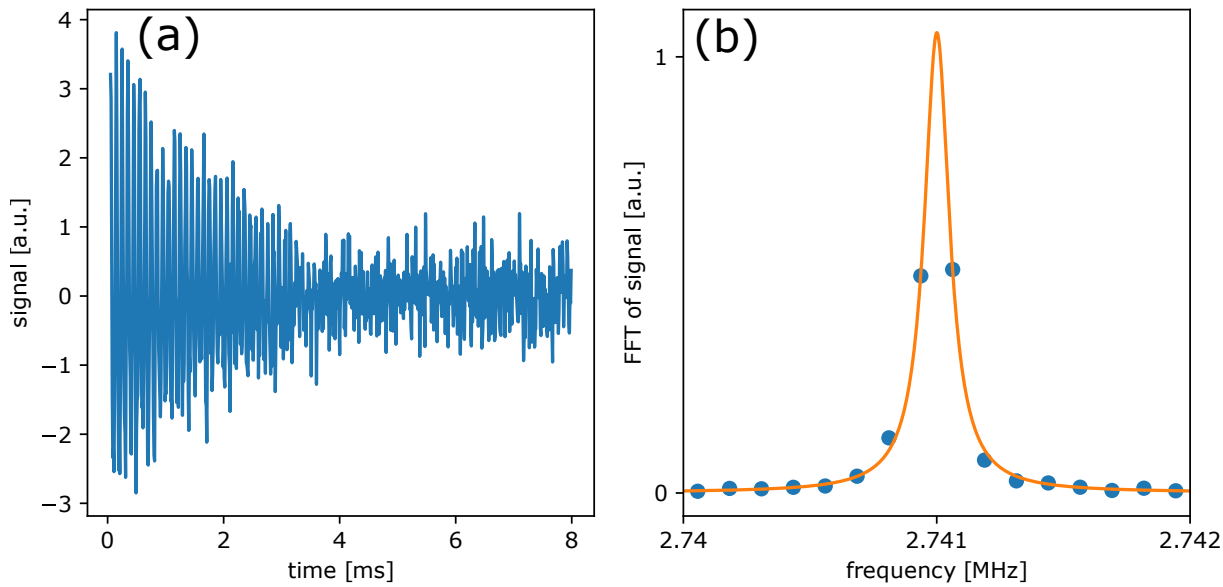

Figure 4.13.: Measurement of the exact ^{13}C Larmor frequency, with the method introduced in sec. 3.1.2. (a) Shows the ^{13}C Ramsey oscillation, due to a detuning between the RF pulses on the ^{13}C spins, and their Larmor frequency. The RF frequency was set to 2.730 133 MHz. In (b), the signal from (a) was Fourier transformed. The frequency axis was set so represent the actual Larmor frequency. It was fitted to be $\nu_0 = 2.740\,134\,\text{MHz} \pm 0.39\,\text{Hz}$.

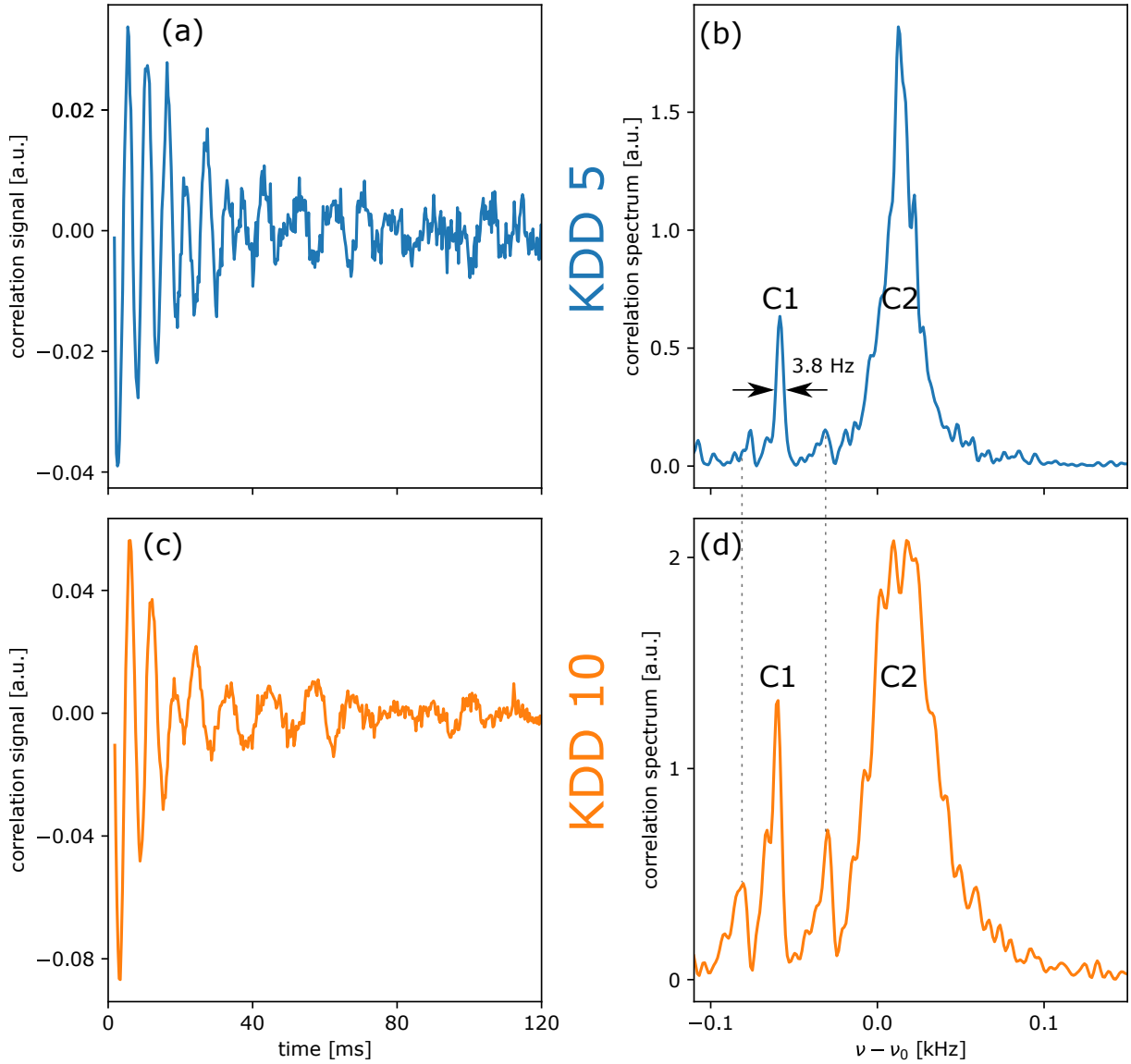

Figure 4.14.: Correlations of sequential weak measurements on a single spin with repetitive readout of the sensor. (a) Shows measurement correlations for a measurement with a KDD5 dynamical decoupling sequence. The decay in terms of number of measurements is similar to before, however, due to the overhead of the repetitive readout, the decay in time is much lower. Indeed, the Fourier transform in (b) shows two signals, of which the signal C1 is very narrow with a FWHM of $\Delta\nu = 3.8\,\mathrm{Hz}$. In comparison, (c,d) is measured with a KDD10 sequence, and hence twice the measurement strength. Both peaks, C1 and C2 broaden due to the larger measurement back-action, however, two additional peaks with smaller amplitude appear. In fact, they already seem to be visible in (b). The dashed lines are meant to guide the eye.

in terms of number measurements, the increased t_c due to the memory spin initialization and readout, causes the signal to persist longer in time. The Fourier transform of the measurements can be seen in (c,d). The measurement was performed with $\tau = 182.458\,\mathrm{ns}$, which results in a lock-in to $\nu = 2.740\,356\,\mathrm{MHz}$. Since the nominal phase shift between two measurements is $\Phi_{\mathrm{nom}} = (40/360) \cdot 2\pi$, the oscillation frequency $1/(4t_c)$ in the Fourier transform corresponds to the undersampled frequency $2.740\,356\,\mathrm{MHz}$. The frequency axis was transformed to show the signal shift from the measured Larmor frequency $\nu_0 = 2.740\,134\,\mathrm{MHz}$. While the signal denoted C2 shows a broad linewidth, C1 has a more narrow line. A Lorentzian fit reveals a FWHM of 3.8 Hz.

4.6. Comparison of sequential weak measurements to measurement-free evolution

As discussed in the introduction of this chapter, high spectral resolution can be achieved by different methods. The most straight forward way to observe the time evolution of a magnetic field with the NV center relies on the correlation of two measurements, separated by some free evolution time [135]. This method will be referred to as the Ramsey method. In order to not disturb the system under study, no measurement is performed during this time, which consequently increases the overall data acquisition time T^{D} for long evolution times. In order to emphasize the capability of the Qdyne method, the data acquisition time T^{D} is analyzed for both methods.

4.6.1. Data acquisition time for the Qdyne method

The correlation signal in case of the Qdyne method can be expressed as

$$C(N) = \sin^2\alpha \cdot e^{-\gamma_{\mathrm{eff}}N} \cdot \cos\left(2\pi N \nu_{\mathrm{eff}} t_c\right), \tag{4.41}$$

resulting from eqs. 4.25 and 4.30, for the case of the weak measurement regime. In order to compare to the Ramsey method, the measurement strength needs to be chosen to allow for a certain resolution $\Delta\nu$. According to eq. 3.1, the FWHM of the Fourier transform of an oscillating signal is $\Delta\nu = 1/(\pi\tau)$, with the signal lifetime τ. For the case of the above correlation signal, the linewidth can be expressed as

$$\Delta\nu = \frac{1}{\pi\tau} = \frac{\gamma_{\mathrm{eff}}}{(\pi t_c)}. \tag{4.42}$$

For small values of α, the effective decay constant can be written as

$$\gamma_{\text{eff}} = -\frac{1}{2}\ln(\cos\alpha) \approx -\frac{1}{2}\ln(1-\alpha^2) \approx \frac{\alpha^2}{2}, \tag{4.43}$$

resulting in a linewidth depending on the measurement strength

$$\Delta\nu \approx \frac{\alpha^2}{2\pi t_c}, \tag{4.44}$$

or, vice versa, a measurement strength depending on the desired frequency resolution

$$\alpha^2 = 2\pi t_c \Delta\nu. \tag{4.45}$$

The correlation function for small values of α can then be written as

$$C(N) = \alpha^2 \cdot e^{-\frac{\alpha^2}{2}N} \cdot \cos\left(2\pi N \nu_{\text{eff}} t_c\right). \tag{4.46}$$

Substituting α with above equation gives

$$C(N) = 2\pi t_c \Delta\nu \cdot e^{-\pi t_c \Delta\nu N} \cdot \cos\left(2\pi N \nu_{\text{eff}} t_c\right). \tag{4.47}$$

The calculation of the SNR of a Fourier transformed signal can be found in the appendix C.4. Since the experimental time-domain signal is not normalized, the signal amplitude needs to be multiplied by an additional factor ϵ^2

$$A_0 = 2\pi t_c \Delta\nu \epsilon^2, \tag{4.48}$$

which corresponds to the photon collection efficiency[3]. According to eq. C.24, the standard deviation of the time domain signal can be expressed as

$$\sigma_t = \epsilon/\sqrt{M}, \tag{4.49}$$

with the measurement repetitions M. This results in a SNR of

$$S/\delta S = \epsilon\sqrt{\pi t_c \Delta\nu M}, \tag{4.50}$$

according to eq. C.27. When substituting $t_c M$ with the total data acquisition time T^{D}, we can calculate the time an experiment takes

$$T^{\text{D,QDyne}} = \frac{\text{SNR}^2}{\epsilon^2 \pi \Delta\nu} \tag{4.51}$$

[3]In order to represent the photon signal, ϵ needs to be squared when considering the auto-correlation function.

4.6.2. Data acquisition time for the Ramsey method

The Ramsey method consists of an initial measurement (e.g. by DD), with duration t_I, a free evolution time t (which will be swept from 0 to T in steps of τ), and a second readout of duration t_I. Since there is no back-action during the free evolution time, the signal has the form

$$C(t) = \epsilon^2 4 \sin^2 \alpha \cos(2\pi\nu t), \tag{4.52}$$

with the measurement strength $\alpha = 2A_{zx}t_I$. Equation C.26 determines the signal amplitude in the Fourier transformed spectrum to be

$$S(\nu) = \frac{1}{2}\epsilon^2 N_{\mathrm{FT}} A_0 = 2\frac{T}{\tau}\epsilon^2 \sin^2 \alpha. \tag{4.53}$$

The noise from eq. C.24 is

$$\delta S = \frac{\epsilon}{\sqrt{M}}\sqrt{\frac{T}{2\tau}}. \tag{4.54}$$

By combination, the SNR is

$$S/\delta S = 2\sqrt{\frac{2MT}{\tau}}\epsilon \sin^2 \alpha. \tag{4.55}$$

By substituting the total data acquisition time $T^{\mathrm{D}} = \frac{MT^2}{2\tau}$ and the desired resolution $\Delta\nu = \frac{1}{\pi T}$, the SNR transforms to

$$S/\Delta S = 4\epsilon \sin^2 \alpha \sqrt{\frac{T^{\mathrm{D}}}{T}} = 4\epsilon \sin^2 \alpha \sqrt{\pi T^{\mathrm{D}} \Delta\nu}. \tag{4.56}$$

Consequently, the data acquisition time is

$$T^{\mathrm{D,Ramsey}} = \frac{\mathrm{SNR}^2}{16\epsilon^2 \pi \Delta\nu \sin^4 \alpha} = \frac{\mathrm{SNR}^2}{\epsilon^2 \pi \Delta\nu} \frac{1}{16 \sin^4 \alpha} = \frac{1}{16 \sin^4 \alpha} \cdot T^{\mathrm{D,QDyne}} \tag{4.57}$$

From this it is clear, that the Ramsey method is strongly outperformed by the Qdyne method in the regime of small α, and hence weakly coupled target spins. In ref. [135], the two measurements in the Ramsey scheme are suggested to always be strong measurements, which can in principle be performed even for weakly coupled target spins by repeating weak measurements. In these cases the measurement duration m_I, which was neglected in this calculation, needs to be taken into consideration.

4.7. Conclusion

One of the fundamental properties of quantum mechanics, is the measurement postulate. When measuring an observable of an arbitrary quantum mechanical state, the outcome will always be an eigenvalue of the measurement operator. The system is at the same time projected in the respective eigenstate. In conventional NMR, the free precession of an ensemble of nuclear spins can be measured by the induced current in coils surrounding the sample. Usually two subsets of coils are used, oriented perpendicular to each other. In terms of the measurement, the coils measure the overall spin expectation value in orthogonal directions, at the same time. Since orthogonal spin observables do not commute, this seems to violate the measurement postulate of quantum mechanics, on first sight. Due to a very weak interaction between measurement apparatus and one single nuclear spin, measurements are however very weak for each spin.

In this chapter, we investigate the transition between a projective measurement, as postulated, and weak measurements. By using NV centers in diamond as a spin sensor, we perform the Qdyne measurement technique, which resembles the quadrature detection done in NMR spectroscopy, to detect oscillating magnetic fields, as well as single nuclear spins. By varying the duration of the interaction time, the strength of the measurement can be chosen, which influences the amplitude of the detected signal, as well as the measurement back-action. We show, that by furthermore varying the separation of the measurements in time, the system can undergo a phase transition between a regime of free Larmor precession, and a Quantum Zeno regime. By choosing the parameters carefully, unperturbed observation of the coherent oscillations of single target spins is possible. Increasing the signal further, by use of repetitive readout of the electron spin, enables performing very weak measurements, resulting in an unperturbed target spin oscillation for $\sim 100\,\mathrm{ms}$, and a spectral resolution of $3.8\,\mathrm{Hz}$.

The advantage of Qdyne, compared to methods as for example described in chapter 3, can be easily understood. In previous works, measurement and free evolution of the nuclear spin were separated [4, 84, 85]. This however means, that for long free evolution times and hence high spectral resolution, measurements are performed rather scarcely. The interleaving of measurements and free evolution in the Qdyne technique offers a way of combining high spectral resolution with fast signal accumulation.

Appendices

A. Deterministic Charge State Control

This chapter of the appendix contains information about the experimental setup used for detecting the deterministic charge state switching, as well as tables of nuclear spin coupling parameters for ^{14}N and ^{15}N nuclear spins coupled to the nitrogen-vacancy center (NV center).

A.1. Experimental setup

For the experiments in this chapter, the microwave part of the experimental setup from sec. 1.5 is changed slightly. Since the gate voltage needs to be changed within one run of the measurement within a few microseconds, the output of the arbitrary waveform generator (AWG) previously providing the radio frequency (RF) pulses for nuclear spin manipulation is fed to a homebuilt CW voltage amplifier, and subsequently to the gate sructure. RF manipulation is realized by employing a second signal generator, fed into the RF amplifier. The setup can be seen in fig. A.1. For the creation of the surface gate structure, the diamond crystal was treted with a hydrogen plasma. This creates a conductive surface layer, and switches below NV centers to the positive charge state. The interdigitated capacitors were created by electron-beam lithography, and substituting the hydrogen surface termination in the respective regions with an oxygen termination. The oxygen terminated gaps have a width of 500 nm, and are non conducting. The hydrogen terminated areas are are connected to metal electrodes evaporated onto the diamond, which are wire-bond to the voltage amplifier generating the bias voltage. For more information, see reference [1].

A.2. Parameters of the charge state dependent Hamiltonian

Parameters for the charge state dependent NV center Hamiltonian can be seen in table A.2 The resulting ^{14}N nuclear magnetic resonance (NMR) transition frequencies can be seen in table A.2.

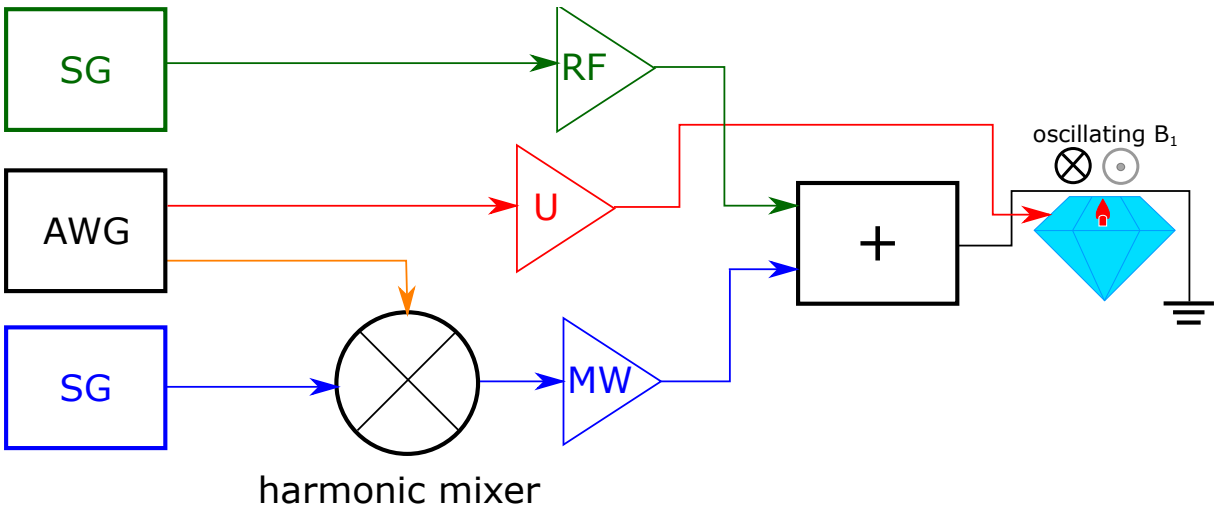

Figure A.1.: In order to provide fast manipulation of the surface gate voltage, the second output of the AWG is disconnected from the RF channel and fed into a CW voltage amplifier. This is then connected to the gate structure on the diamond surface. RF signal are created by a signal generator, connected to the RF amplifier.

quantity	symbol	value
zero-field splitting	D	2.87 GHz
reduced gyromagnetic ratios, electron spin	$\tilde{\gamma}_{\mathrm{e}}$	28.03 GHz/T
reduced gyromagnetic ratios, nuclear spins, ^{14}N	$\tilde{\gamma}_{\mathrm{n}}$	3.077 MHz/T
reduced gyromagnetic ratios, nuclear spins, ^{15}N	$\tilde{\gamma}_{\mathrm{n}}$	−4.316 MHz/T
hyperfine interaction parameters, ^{14}N, NV$^-$	$A_{\parallel}$, $A_{\perp}$	−2.172(2), −2.630(2) MHz
hyperfine interaction parameters, ^{14}N, NV^0	$A_{\parallel}$	6.06MHz
hyperfine interaction parameters, ^{15}N, NV$^-$	$A_{\parallel}$, $A_{\perp}$	3.047, 3.690 MHz
hyperfine interaction parameters, ^{15}N, NV^0	$A_{\parallel}$	8.484MHz
quadrupole splitting parameter, ^{14}N, NV$^-$	$C_q^{(-)}$	−4.945 MHz
quadrupole splitting parameter, ^{14}N, NV^0	$C_q^{(-)}$	−4.654 MHz

Table A.1.: Various parameters for the spin Hamiltonian presented in eq. (2.1). The hyperfine coupling constants for the ^{15}N spin are derived from the values of the ^{14}N spin taking into account the different gyromagnetic ratios $\tilde{\gamma}_{\mathrm{n}}$. The $A_{\parallel}$ value for ^{15}N agrees well with the measured result [50].

species	electron spin state	transition	frequency
^{14}N	$m_s = 0$	$m_i = +1$ to $m_i = 0$	6.390 MHz
^{14}N	$m_s = 0$	$m_i = 0$ to $m_i = -1$	3.500 MHz
^{14}N	$m_s = -1$	$m_i = +1$ to $m_i = 0$	4.228 MHz
^{14}N	$m_s = -1$	$m_i = 0$ to $m_i = -1$	5.662 MHz
^{15}N	$m_s = 0$	$m_i = -1/2$ to $m_i = +1/2$	2.028 MHz
^{15}N	$m_s = -1$	$m_i = -1/2$ to $m_i = +1/2$	1.019 MHz

Table A.2.: Nitrogen NMR transition frequencies for an applied magnetic field of 470 mT, as in the experiment.

B. Spectroscopy of small spin clusters assisted by a nuclear spin memory

This chapter contains supplementary information about the experiments from chapter 3.

B.1. The diamond sample

The diamond sample used in this experiment is a polished (111)-oriented slice from a larger high pressure and high temperature (HPHT) diamond crystal. The size is $2\,\mathrm{mm}\times 2\,\mathrm{mm}\times 88\,\mu\mathrm{m}$. The diamond is enriched with a ^{12}C concentration of 99.995%. It was irradiated with 2 MeV electrons at room-temperature to a fluency of $1.3 \times 10^{11}\,\mathrm{cm}^{-2}$, with subsequent annealing at 1000 °C. The isotopic purification of the carbon host material enables the detection of single, distinguishable ^{13}C nuclear spins, with coupling of a few kHz.

B.2. ^{13}C NMR spectra of target spin B_1

In order to validate the scaling of coherence times with coupling strength between NV center and nuclear spin, another defect with a weaker coupled ^{13}Cspin was searched for. A fitting candidate can be seen in fig. B.1. Although the spectrum seems to consist out of three coupled ^{13}C spins, the one with $A_{\parallel} = -1.8\,\mathrm{kHz}$ dominates the signal.

B.3. Fitting spectra

When Fourier transforming a time-domain signal of the form

$$S(t) = A_0 e^{-t/\tau} \cdot \cos(2\pi\nu t), \tag{B.1}$$

the resulting spectrum differs, depending on the sampling of the signal, as well as the cut-off of in the time-domain. For example, if the signal is sampled in infinitely small steps, and cuts of in in infinity, the resulting spectrum is of Lorentzian shape. Since these conditions are not experimentally feasible, the Fourier transform differs from the pure Lorentzian shape. Therefore, the fit on the signal happens in the time-domain.

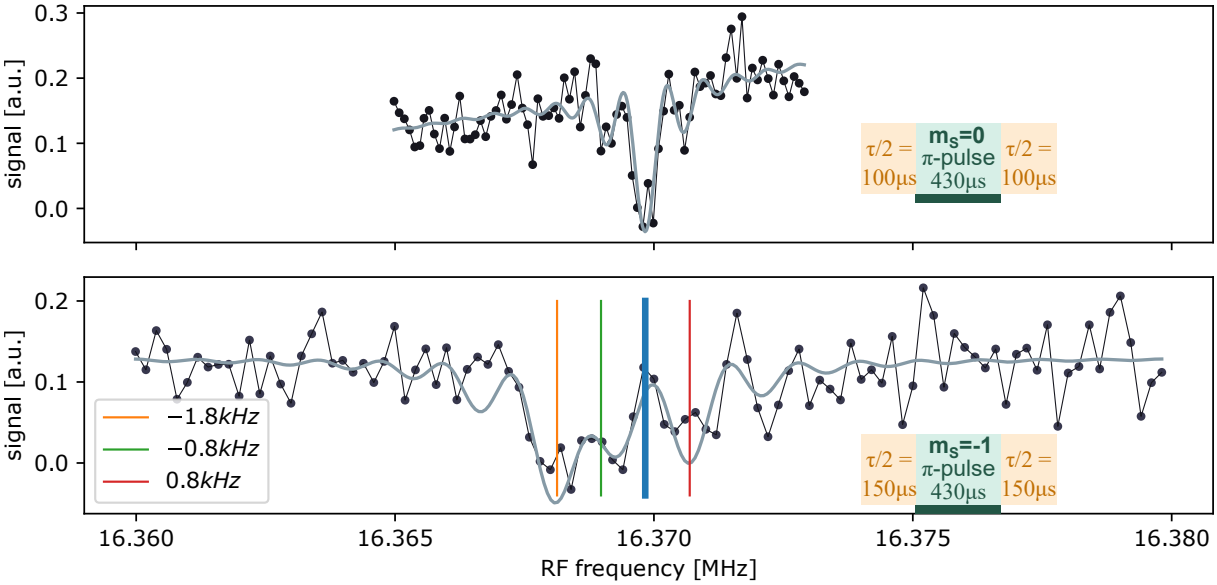

Figure B.1.: ^{13}CNMR spectra, without (upper panel) and with (lower panel) hyperfine interaction. The measurement is the same as in fig. 3.3.The four lines denote the fitted resonance frequency. The thick blue line is the bare ^{13}C Larmor frequency.

The corresponding fit in the Fourier transformed coordinates therefore exhibits the same properties, as the original signal.

B.4. Filter functions for entanglement based detection sequences

In sec. 1.7, the spectral filter functions for various spin manipulation sequences were calculated. In fig. B.2, the filter function for the sequence introduced in chapter 3.1.2 is shown. It can be seen, that the combination of two sensing steps to form the encoding or decoding part of the sequence is beneficial, since the susceptibility to noise is shifted towards higher frequencies. Furthermore, the overall amplitude is reduced.

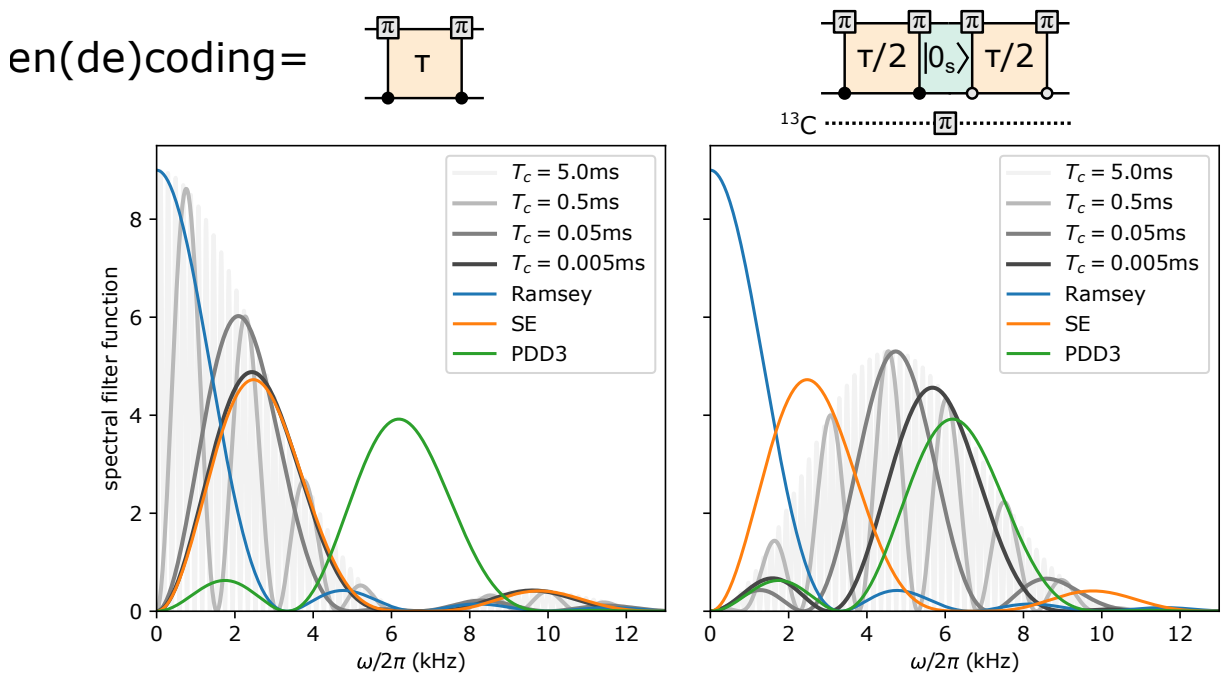

Figure B.2.: Spectral filter functions for entanglement based sensing sequences. The sequence introduced in sec. 3.1.2 consists of an encoding, a storage and manipulation and a decoding part. The en- or decoding part can consist of a single sensing step (left pane), or two sensing steps with an intermediate refocusing part. The filter function is calculated for a storage and manipulation part of variable length (T_c, gray lines). For comparison, well known sequences are shown for comparison (spin echo (SE) and periodic dynamical decoupling (PDD)).

C. High-resolution spectroscopy of single nuclear spins via sequential weak measurements

C.1. Experimental setup

The experimental setup for chapter 4 partly differs from the one introduced in sec. 1.5. For the detection of an AC magnetic field with the quantum heterodyne detection (Qdyne) method, the RF generation pathway is changed, according to fig.C.1. The RF signal needs to be generated by a signal generator, to provide a coherent signal independent of the measurement sequence. Since we want to detect weak signals, the RF amplifier is omitted as well. The diamond crystal used is the same as in chapter 3, see B.1.

C.2. Correlation function for subsequent weak measurements

For the weak measurements performed in the Qdyne sequence on single nuclear spins, the sensor spin is initialized in x, rotated by the controlled phase gate (CPHASE gate) gate, and afterwards measured along the y direction. The effect of this measurement on the nuclear spin can be characterized by the Kraus operators

$$\hat{M}_{\pm} = \left(e^{i\alpha\hat{I}_x} \pm e^{-i\alpha\hat{I}_x}\right)/2, \tag{C.1}$$

where $\pm$ denotes the measurement outcome $|\pm y\rangle$ of the sensor spin measurements. When expressing the initial state of the target spin with the density matrix $\hat{\rho}$, the probability for measuring one of the two possible output values $m_k = \pm 1$

$$P(\pm 1) = \mathrm{Tr}\left(\hat{M}_{\pm}\hat{\rho}\hat{M}_{\pm}^{\dagger}\right). \tag{C.2}$$

When the initial state $\hat{\rho}$ is fully unpolarized, the state after the measurement is $\hat{\rho}_{\pm} = 1/2 \pm \hat{I}_x \sin\alpha$. The component $\hat{I}_x \sin\alpha$ is called heralded initialization. When the measurement

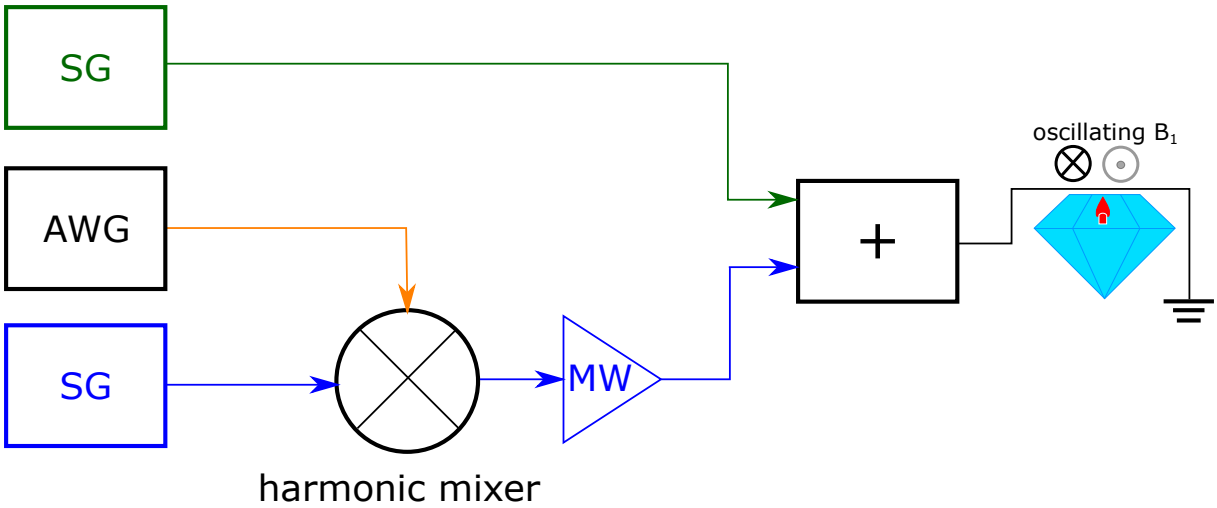

Figure C.1.: In order to detect an AC magnetic field with the Qdyne technique, the RF part of the experimental setup introduced in sec 1.5.2 is changed. Generation is done by a signal generator, providing a coherent signal independent of a running measurement. The RF amplifier is removed.

outcome is ignored, the state transforms to

$$\hat{\mathcal{M}}[\hat{\rho}] = \hat{M}_+\hat{\rho}\hat{M}_+^\dagger + \hat{M}_-\hat{\rho}\hat{M}_-^\dagger \tag{C.3}$$

$$= \hat{\rho}\cos^2(\alpha/2) + 4\hat{I}_x\hat{\rho}\hat{I}_x\sin^2(\alpha/2). \tag{C.4}$$

Thus, the polarization along the y and z axis is reduced (by a factor $\cos\alpha$), but the x component is unchanged. The following free precession can be expressed as

$$\hat{\mathcal{U}}[\hat{\rho}] = e^{-i\Phi\hat{I}_z}\hat{\rho}e^{i\Phi\hat{I}_z}. \tag{C.5}$$

Now, the correlation function can be written as

$$C(N) = \langle m_{k+N}m_k\rangle = \mathrm{Tr}\left[\hat{\mathcal{P}}\left(\hat{\mathcal{U}}\hat{\mathcal{M}}\right)^{N-1}\hat{\mathcal{U}}\hat{\mathcal{P}}[\hat{\rho}]\right], \tag{C.6}$$

with the heralded polarization operator $\hat{\mathcal{P}} = \hat{M}_+\hat{\rho}\hat{M}_+^\dagger - \hat{M}_-\hat{\rho}\hat{M}_-^\dagger$. One can furthermore describe the precession of the target spin polarization $\underline{I}$ by the transform

$$\mathcal{U} = \begin{pmatrix} I_x \\ I_y \\ I_z \end{pmatrix} = \begin{pmatrix} \cos\Phi & -\sin\Phi & 0 \\ \sin\Phi & \cos\Phi & 0 \\ 0 & 0 & 1 \end{pmatrix}\begin{pmatrix} I_x \\ I_y \\ I_z \end{pmatrix}, \tag{C.7}$$

and the measurement by

$$\mathcal{M}\begin{pmatrix} I_x \\ I_y \\ I_z \end{pmatrix} = \begin{pmatrix} 1 & 0 & 0 \\ 0 & \cos\alpha & 0 \\ 0 & 0 & \cos\alpha \end{pmatrix}\begin{pmatrix} I_x \\ I_y \\ I_z \end{pmatrix}. \tag{C.8}$$

The eigenvalues of the combined transformation $\mathcal{UM}$ are

$$\eta_z = \cos\alpha \tag{C.9}$$

$$\eta_\pm = \left(\cos\Phi \pm \sqrt{\mu^2 - \sin^2\Phi}\right)\cos^2(\alpha/2), \tag{C.10}$$

with $\mu = \tan^2(\alpha/2)$. The corresponding right eigenvectors are

$$\underline{v}_z^{\mathrm{R}} = \begin{pmatrix} 0 \\ 0 \\ 1 \end{pmatrix} \tag{C.11}$$

$$\underline{v}_\pm^{\mathrm{R}} = \begin{pmatrix} \cos\Phi\sin^2(\alpha/2) \pm \Delta \\ \sin\Phi \\ 0 \end{pmatrix}, \tag{C.12}$$

with $\Delta = \cos^2(\alpha/2)\sqrt{\mu^2 - \sin^2\Phi}$. The left eigenvectors are

$$\underline{v}_z^{\mathrm{L}} = \begin{pmatrix} 0 & 0 & 1 \end{pmatrix} \tag{C.13}$$

$$\underline{v}_\pm^{\mathrm{L}} = \frac{1}{2\Delta\sin\Phi}\begin{pmatrix} \pm\sin\Phi & \mp\cos\Phi\sin^2(\alpha/2) - \Delta & 0 \end{pmatrix}. \tag{C.14}$$

These eigenvectors satisfy the orthonormal conditions $\underline{v}_i^{\mathrm{L}}\underline{v}_j^{\mathrm{R}} = \delta_{ij}$ and $\underline{v}_+^{\mathrm{R}}\underline{v}_+^{\mathrm{L}} + \underline{v}_-^{\mathrm{R}}\underline{v}_-^{\mathrm{L}} + \underline{v}_z^{\mathrm{R}}\underline{v}_z^{\mathrm{L}} = 1$. When the target spin is initially in a fully unpolarized state, the heralded initialization polarizes the spin along x to $\underline{e}_x \sin\alpha$, with the unit vector along x $\underline{e}_x$. Since the following measurements, as well as the precession keeps the spin in the x-y plane, only the eigenstates with denotation $\pm$ are relevant for the transformation $\mathcal{UM}$ of the polarization. The correlation function then is

$$C(N) = \sin^2\alpha\left[\left(\underline{e}_x^{\mathrm{T}}\underline{v}_+^{\mathrm{R}}\underline{v}_+^{\mathrm{L}}\underline{e}_x\right)\eta_+^N + \left(\underline{e}_x^{\mathrm{T}}\underline{v}_-^{\mathrm{R}}\underline{v}_-^{\mathrm{L}}\underline{e}_x\right)\eta_-^N\right] \tag{C.15}$$

$$= \sin^2\alpha\left(\frac{\eta_+^N + \eta_-^N}{2} + \frac{\eta_+^N - \eta_-^N}{\eta_+ - \eta_-}\cos\Phi\sin^2(\alpha/2)\right). \tag{C.16}$$

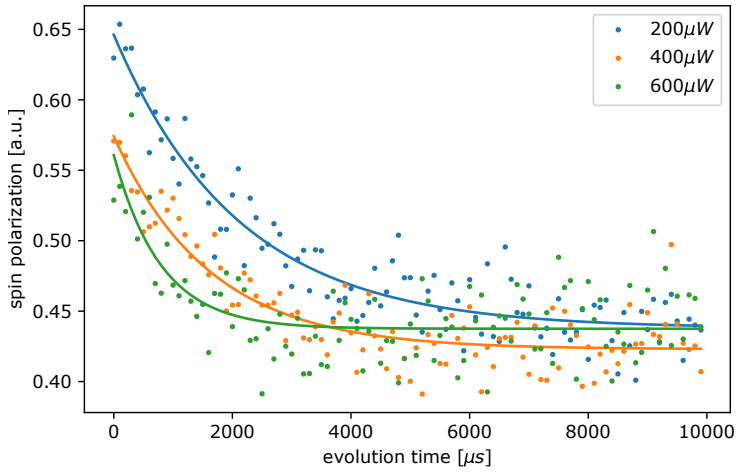

Figure C.2.: Measurement of the longitudinal spin relaxation time T_1 of an NV center electron spin. Depending on the applied excitation laser power, the T_1 time varies from 2.09 ms at 200 μW over 1.6 ms at 400 μW to 0.79 ms at 600 μW.

This can be transformed to the form from section 4.2

$$C(N) = \sin^2 \alpha \left(C_+ \eta_+^N + C_- \eta_-^N \right) /2 \tag{C.17}$$

$$\text{with } C_\pm = 1 \pm \frac{\mu \cos(\Phi)}{\sqrt{\mu^2 \sin^2 \Phi}}. \tag{C.18}$$

C.3. Longitudinal relaxation of NV center electron spins

The diamond sample used in chapter 4 shows an unexpectedly low NV center electron spin T_1 time. In fact, the measured T_1 time seems to depend on the applied laser power, see fig. C.2. This is an expected behavior when using a continuous wave laser, that is pulsed using an acousto-optic modulator (AOM). Since some laser light is transmitted even if the AOM is turned off, higher laser power means more leakage, and hence a shorter T_1 time. However, the excitation laser used for these experiments was a semiconductor laser diode, that can be switched on a timescale of nanoseconds, and therefore should not induce such behavior. The origin of this effect is supposed to stem from charged impurities in the vicinity of the NV center that are influenced by laser excitation. The optical excitation power hence affects the charge environment of the NV center. The observed T_1 decay is therefore a slow decay of the charge state from NV^- to NV^0, which seems like a decay of spin polarization[1].

[1] In principle, since NV^0 does have an electron spin $S = 1/2$, a change in charge state is at the same stime a change in spin state.

C.4. Signal-to-noise ratio in the Fourier transform

We assume random time-domain data S(N), with a normal distribution $\mathrm{N}(0, \sigma_t)$. When represented by a vector of the form $\mathbf{s} = \{S(1), S(2), S(N_{\mathrm{FT}})\}$, the Fourier transform is

$$\mathbf{f} = \mathbf{U}\mathbf{s}, \tag{C.19}$$

with the Fourier transform matrix

$$U_i j = e^{-i2(i-1)(j-1)\pi/N_{\mathrm{FT}}}. \tag{C.20}$$

The noise amplitude can then be extracted from the diagonal part of the averaged covariance matrix $\langle \mathbf{s}\mathbf{s}^T \rangle = \sigma_t^2 \mathbf{1}$, or as the normalized scalar product $\mathbf{s}^T\mathbf{s} = N_{\mathrm{FT}}\sigma_t^2$.
Denoting the real part $\mathbf{a} = \Re\mathbf{f}$ and the imaginary part $\mathbf{b} = \Im\mathbf{f}$ of the Fourier transform, the covariance of the Fourier transform can be written as

$$\langle \mathbf{a}\mathbf{a}^T \rangle = [\Re\mathbf{U}]\langle \mathbf{s}\mathbf{s}^T \rangle [\Re\mathbf{U}]^T \tag{C.21}$$

$$\langle \mathbf{b}\mathbf{b}^T \rangle = [\Im\mathbf{U}]\langle \mathbf{s}\mathbf{s}^T \rangle [\Im\mathbf{U}]^T \tag{C.22}$$

$$\langle \mathbf{a}\mathbf{b}^T \rangle = [\Re\mathbf{U}]\langle \mathbf{s}\mathbf{s}^T \rangle [\Im\mathbf{U}]^T \tag{C.23}$$

With the relations $\mathbf{U} = \mathbf{U}^T$ and $\mathbf{U}\mathbf{U}^\dagger = N_{\mathrm{FT}}$, the standard deviation of the real and imaginary part of the Fourier transformed signal can be calculated to be proportional to the standard deviation of the time domain signal

$$\delta S = \sigma_\omega = \sigma_t \sqrt{N_{\mathrm{FT}}/2}. \tag{C.24}$$

We assume a signal in time of the form

$$S^{\mathrm{time}}(N) = A_0 e^{-\gamma_{\mathrm{eff}} N} \cdot \cos(2\pi\nu t_{\mathrm{sample}} N), \tag{C.25}$$

with a decay rate γ_{eff} in units of measurements, and the sampling interval t_{sample}. The amplitude of the Fourier transformed spectrum then is

$$S(\nu) \approx \frac{1}{2} \min(\gamma_{\mathrm{eff}}^{-1}, N_{\mathrm{FT}}) A_0. \tag{C.26}$$

The signal to noise ratio $\frac{S}{\delta S}$ is therefore maximum, when choosing $N_{\mathrm{FT}} = \gamma_{\mathrm{eff}}^{-1}$ for the construction of the Fourier transformed spectrum. In that case, the signal-to-noise ratio

(SNR) can be expressed as

$$S/\delta S = \frac{A_0\sqrt{\gamma_{\text{eff}}^{-1}}}{2\sigma_t} \tag{C.27}$$

Bibliography

[1] Moritz V. Hauf, Patrick Simon, Nabeel Aslam, Matthias Pfender, Philipp Neumann, Sébastien Pezzagna, Jan Meijer, Jörg Wrachtrup, Martin Stutzmann, Friedemann Reinhard, and José A. Garrido. "Addressing Single Nitrogen-Vacancy Centers in Diamond with Transparent in-Plane Gate Structures." In: *Nano Letters* (Apr. 9, 2014). DOI: 10.1021/nl4047619 (cit. on pp. i, xi, xviii, 29, 30, 40, 97).

[2] Matthias Pfender, Nabeel Aslam, Patrick Simon, Denis Antonov, Gergő Thiering, Sina Burk, Felipe Fávaro de Oliveira, Andrej Denisenko, Helmut Fedder, Jan Meijer, Jose A. Garrido, Adam Gali, Tokuyuki Teraji, Junichi Isoya, Marcus William Doherty, Audrius Alkauskas, Alejandro Gallo, Andreas Grüneis, Philipp Neumann, and Jörg Wrachtrup. "Protecting a Diamond Quantum Memory by Charge State Control." In: *Nano Letters* 17.10 (Oct. 11, 2017), pp. 5931–5937. DOI: 10.1021/acs.nanolett.7b01796 (cit. on pp. i, xi, xviii, 29).

[3] Nabeel Aslam, Matthias Pfender, Philipp Neumann, Rolf Reuter, Andrea Zappe, Felipe Fávaro de Oliveira, Andrej Denisenko, Hitoshi Sumiya, Shinobu Onoda, Junichi Isoya, and Jörg Wrachtrup. "Nanoscale Nuclear Magnetic Resonance with Chemical Resolution." In: *Science* 357.6346 (July 7, 2017), pp. 67–71. DOI: 10.1126/science.aam8697. pmid: 28572453 (cit. on pp. i, xi, xviii, 43).

[4] Matthias Pfender, Nabeel Aslam, Hitoshi Sumiya, Shinobu Onoda, Philipp Neumann, Junichi Isoya, Carlos A. Meriles, and Jörg Wrachtrup. "Nonvolatile Nuclear Spin Memory Enables Sensor-Unlimited Nanoscale Spectroscopy of Small Spin Clusters." In: *Nature Communications* 8.1 (Oct. 10, 2017), p. 834. DOI: 10.1038/s41467-017-00964-z (cit. on pp. i, xi, xviii, 38, 43, 88, 94).

[5] Matthias Pfender, Ping Wang, Hitoshi Sumiya, Shinobu Onoda, Wen Yang, Durga Bhaktavatsala Rao Dasari, Philipp Neumann, Xin-Yu Pan, Junichi Isoya, Ren-Bao Liu, and J. Wrachtrup. "High-Resolution Spectroscopy of Single Nuclear Spins via Sequential Weak Measurements." In: (June 6, 2018). arXiv: 1806.02181 [cond-mat, physics:quant-ph] (cit. on pp. i, xi, xviii, 72).

[6] Nabeel Aslam, Matthias Pfender, Rainer Stöhr, Philipp Neumann, Marc Scheffler, Hitoshi Sumiya, Hiroshi Abe, Shinobu Onoda, Takeshi Ohshima, Junichi Isoya, and Jörg Wrachtrup. "Single Spin Optically Detected Magnetic Resonance with

60–90 GHz (E-Band) Microwave Resonators." In: *Review of Scientific Instruments* 86.6 (June 1, 2015), p. 064704. DOI: 10.1063/1.4922664 (cit. on pp. ii, 63).

[7] Liang Jin, Matthias Pfender, Nabeel Aslam, Philipp Neumann, Sen Yang, Jörg Wrachtrup, and Ren-Bao Liu. "Proposal for a Room-Temperature Diamond Maser." In: *Nature Communications* 6 (Sept. 23, 2015), p. 8251. DOI: 10.1038/ncomms9251 (cit. on pp. ii, 1).

[8] Thomas Häberle, Thomas Oeckinghaus, Dominik Schmid-Lorch, Matthias Pfender, Felipe Fávaro de Oliveira, Seyed Ali Momenzadeh, Amit Finkler, and Jörg Wrachtrup. "Nuclear Quantum-Assisted Magnetometer." In: *Review of Scientific Instruments* 88.1 (Jan. 2017), p. 013702. DOI: 10.1063/1.4973449 (cit. on pp. ii, 27).

[9] F. Jelezko, I. Popa, A. Gruber, C. Tietz, J. Wrachtrup, A. Nizovtsev, and S. Kilin. "Single Spin States in a Defect Center Resolved by Optical Spectroscopy." In: *Applied Physics Letters* 81.12 (Sept. 9, 2002), pp. 2160–2162. DOI: 10.1063/1.1507838 (cit. on p. 1).

[10] F. Jelezko, T. Gaebel, I. Popa, M. Domhan, A. Gruber, and J. Wrachtrup. "Observation of Coherent Oscillation of a Single Nuclear Spin and Realization of a Two-Qubit Conditional Quantum Gate." In: *Physical Review Letters* 93.13 (Sept. 20, 2004), p. 130501. DOI: 10.1103/PhysRevLett.93.130501 (cit. on p. 1).

[11] L. Childress, M. V. Gurudev Dutt, J. M. Taylor, A. S. Zibrov, F. Jelezko, J. Wrachtrup, P. R. Hemmer, and M. D. Lukin. "Coherent Dynamics of Coupled Electron and Nuclear Spin Qubits in Diamond." In: *Science* 314.5797 (Oct. 13, 2006), pp. 281–285. DOI: 10.1126/science.1131871. pmid: 16973839 (cit. on pp. 1, 13, 29, 37).

[12] Torsten Gaebel, Michael Domhan, Iulian Popa, Christoffer Wittmann, Philipp Neumann, Fedor Jelezko, James R. Rabeau, Nikolas Stavrias, Andrew D. Greentree, Steven Prawer, Jan Meijer, Jason Twamley, Philip R. Hemmer, and Jörg Wrachtrup. "Room-Temperature Coherent Coupling of Single Spins in Diamond." In: *Nature Physics* 2.6 (May 28, 2006), pp. 408–413. DOI: 10.1038/nphys318 (cit. on p. 1).

[13] M. V. Gurudev Dutt, L. Childress, L. Jiang, E. Togan, J. Maze, F. Jelezko, A. S. Zibrov, P. R. Hemmer, and M. D. Lukin. "Quantum Register Based on Individual Electronic and Nuclear Spin Qubits in Diamond." In: *Science* 316.5829 (Jan. 6, 2007), pp. 1312–1316. DOI: 10.1126/science.1139831 (cit. on pp. 1, 29).

[14] P. Neumann, N. Mizuochi, F. Rempp, P. Hemmer, H. Watanabe, S. Yamasaki, V. Jacques, T. Gaebel, F. Jelezko, and J. Wrachtrup. "Multipartite Entanglement Among Single Spins in Diamond." In: *Science* 320.5881 (June 6, 2008), pp. 1326–1329. DOI: 10.1126/science.1157233 (cit. on pp. 1, 11).

[15] P. Neumann, J. Beck, M. Steiner, F. Rempp, H. Fedder, P. R. Hemmer, J. Wrachtrup, and F. Jelezko. "Single-Shot Readout of a Single Nuclear Spin." In: *Science* 329.5991 (July 1, 2010), pp. 542–544. DOI: 10.1126/science.1189075 (cit. on pp. 1, 11, 12, 25, 32, 44, 48, 88).

[16] P. Neumann, R. Kolesov, B. Naydenov, J. Beck, F. Rempp, M. Steiner, V. Jacques, G. Balasubramanian, M. L. Markham, D. J. Twitchen, S. Pezzagna, J. Meijer, J. Twamley, F. Jelezko, and J. Wrachtrup. "Quantum Register Based on Coupled Electron Spins in a Room-Temperature Solid." In: *Nature Physics* 6.4 (2010), pp. 249–253. DOI: 10.1038/nphys1536 (cit. on p. 1).

[17] F. Dolde, I. Jakobi, B. Naydenov, N. Zhao, S. Pezzagna, C. Trautmann, J. Meijer, P. Neumann, F. Jelezko, and J. Wrachtrup. "Room-Temperature Entanglement between Single Defect Spins in Diamond." In: *Nature Physics* (2013). DOI: 10.1038/nphys2545 (cit. on pp. 1, 29).

[18] G. Waldherr, Y. Wang, S. Zaiser, M. Jamali, T. Schulte-Herbrüggen, H. Abe, T. Ohshima, J. Isoya, J. F. Du, P. Neumann, and J. Wrachtrup. "Quantum Error Correction in a Solid-State Hybrid Spin Register." In: *Nature* 506.7487 (Feb. 13, 2014), pp. 204–207. DOI: 10.1038/nature12919 (cit. on pp. 1, 3, 11, 29, 43).

[19] T. H. Taminiau, J. Cramer, T. van der Sar, V. V. Dobrovitski, and R. Hanson. "Universal Control and Error Correction in Multi-Qubit Spin Registers in Diamond." In: *Nature Nanotechnology* advance online publication (Feb. 2, 2014). DOI: 10.1038/nnano.2014.2 (cit. on pp. 1, 29).

[20] T. H. Taminiau, J. J. T. Wagenaar, T. van der Sar, F. Jelezko, V. V. Dobrovitski, and R. Hanson. "Detection and Control of Individual Nuclear Spins Using a Weakly Coupled Electron Spin." In: *Physical Review Letters* 109.13 (Sept. 25, 2012), p. 137602. DOI: 10.1103/PhysRevLett.109.137602 (cit. on pp. 1, 13, 24, 43, 66, 77, 81).

[21] Jonathan D. Breeze, Enrico Salvadori, Juna Sathian, Neil McN Alford, and Christopher W. M. Kay. "Continuous-Wave Room-Temperature Diamond Maser." In: *Nature* 555.7697 (Mar. 2018), p. 493. DOI: 10.1038/nature25970 (cit. on p. 1).

[22] J. R. Maze, P. L. Stanwix, J. S. Hodges, S. Hong, J. M. Taylor, P. Cappellaro, L. Jiang, M. V. Gurudev Dutt, E. Togan, A. S. Zibrov, A. Yacoby, R. L. Walsworth, and M. D. Lukin. "Nanoscale Magnetic Sensing with an Individual Electronic Spin in Diamond." In: *Nature* 455.7213 (Oct. 2, 2008), pp. 644–647. DOI: 10.1038/nature07279 (cit. on pp. 1, 43).

[23] Gopalakrishnan Balasubramanian, I. Y. Chan, Roman Kolesov, Mohannad Al-Hmoud, Julia Tisler, Chang Shin, Changdong Kim, Aleksander Wojcik, Philip R. Hemmer, Anke Krueger, Tobias Hanke, Alfred Leitenstorfer, Rudolf Bratschitsch, Fedor Jelezko, and Jörg Wrachtrup. "Nanoscale Imaging Magnetometry with Diamond Spins under Ambient Conditions." In: *Nature* 455.7213 (Oct. 2, 2008), pp. 648–651. DOI: 10.1038/nature07278 (cit. on pp. 1, 43).

[24] S. Steinert, F. Dolde, P. Neumann, A. Aird, B. Naydenov, G. Balasubramanian, F. Jelezko, and J. Wrachtrup. "High Sensitivity Magnetic Imaging Using an Array of Spins in Diamond." In: *Review of Scientific Instruments* 81.4 (2010), p. 043705. DOI: 10.1063/1.3385689 (cit. on p. 1).

[25] F. Dolde, H. Fedder, M. W. Doherty, T. Nöbauer, F. Rempp, G. Balasubramanian, T. Wolf, F. Reinhard, L. C. L. Hollenberg, F. Jelezko, and J. Wrachtrup. "Electric-Field Sensing Using Single Diamond Spins." In: *Nature Physics* 7.6 (2011), pp. 459–463. DOI: 10.1038/nphys1969 (cit. on pp. 1, 43).

[26] Florian Dolde, Marcus W. Doherty, Julia Michl, Ingmar Jakobi, Boris Naydenov, Sebastien Pezzagna, Jan Meijer, Philipp Neumann, Fedor Jelezko, Neil B. Manson, and Jörg Wrachtrup. "Nanoscale Detection of a Single Fundamental Charge in Ambient Conditions Using the NV- Center in Diamond." In: *Physical Review Letters* 112.9 (Mar. 3, 2014), p. 097603. DOI: 10.1103/PhysRevLett.112.097603 (cit. on p. 1).

[27] Julia Michl, Tokuyuki Teraji, Sebastian Zaiser, Ingmar Jakobi, Gerald Waldherr, Florian Dolde, Philipp Neumann, Marcus W. Doherty, Neil B. Manson, Junichi Isoya, and Jörg Wrachtrup. "Perfect Alignment and Preferential Orientation of Nitrogen-Vacancy Centers during Chemical Vapor Deposition Diamond Growth on (111) Surfaces." In: *Applied Physics Letters* 104.10 (Mar. 10, 2014), p. 102407. DOI: 10.1063/1.4868128 (cit. on p. 1).

[28] P. Neumann, I. Jakobi, F. Dolde, C. Burk, R. Reuter, G. Waldherr, J. Honert, T. Wolf, A. Brunner, J. H. Shim, D. Suter, H. Sumiya, J. Isoya, and J. Wrachtrup. "High-Precision Nanoscale Temperature Sensing Using Single Defects in Diamond." In: *Nano Letters* 13.6 (June 12, 2013), pp. 2738–2742. DOI: 10.1021/nl401216y (cit. on pp. 1, 43).

[29] V. M. Acosta, E. Bauch, M. P. Ledbetter, A. Waxman, L.-S. Bouchard, and D. Budker. "Temperature Dependence of the Nitrogen-Vacancy Magnetic Resonance in Diamond." In: *Physical Review Letters* 104.7 (Feb. 17, 2010), p. 070801. DOI: 10.1103/PhysRevLett.104.070801 (cit. on p. 1).

[30] G. Kucsko, P. C. Maurer, N. Y. Yao, M. Kubo, H. J. Noh, P. K. Lo, H. Park, and M. D. Lukin. "Nanometre-Scale Thermometry in a Living Cell." In: *Nature* 500.7460 (Aug. 2013), pp. 54–58. DOI: 10.1038/nature12373 (cit. on pp. 1, 43).

[31] Nan Zhao, Jan Honert, Bernhard Schmid, Michael Klas, Junichi Isoya, Matthew Markham, Daniel Twitchen, Fedor Jelezko, Ren-Bao Liu, Helmut Fedder, and Jörg Wrachtrup. "Sensing Single Remote Nuclear Spins." In: *Nature Nanotechnology* 7.10 (Oct. 2012), pp. 657–662. DOI: 10.1038/nnano.2012.152 (cit. on pp. 1, 13, 24, 66, 77, 81).

[32] Shimon Kolkowitz, Quirin P. Unterreithmeier, Steven D. Bennett, and Mikhail D. Lukin. "Sensing Distant Nuclear Spins with a Single Electron Spin." In: *Physical Review Letters* 109.13 (Sept. 25, 2012), p. 137601. DOI: 10.1103/PhysRevLett.109.137601 (cit. on pp. 1, 13, 24, 66, 77, 81).

[33] T. Staudacher, F. Shi, S. Pezzagna, J. Meijer, J. Du, C. A. Meriles, F. Reinhard, and J. Wrachtrup. "Nuclear Magnetic Resonance Spectroscopy on a (5-Nanometer)3 Sample Volume." In: *Science* 339.6119 (Jan. 2, 2013), pp. 561–563. DOI: 10.1126/science.1231675 (cit. on pp. 1, 13, 24, 43, 54, 62, 72, 73).

[34] A. Ajoy, U. Bissbort, M. D. Lukin, R. L. Walsworth, and P. Cappellaro. "Atomic-Scale Nuclear Spin Imaging Using Quantum-Assisted Sensors in Diamond." In: *Physical Review X* 5.1 (Jan. 7, 2015), p. 011001. DOI: 10.1103/PhysRevX.5.011001 (cit. on pp. 1, 43).

[35] H. J. Mamin, M. Kim, M. H. Sherwood, C. T. Rettner, K. Ohno, D. D. Awschalom, and D. Rugar. "Nanoscale Nuclear Magnetic Resonance with a Nitrogen-Vacancy Spin Sensor." In: *Science* 339.6119 (Jan. 2, 2013), pp. 557–560. DOI: 10.1126/science.1231540. pmid: 23372008 (cit. on pp. 1, 13, 24, 43, 54, 62).

[36] T. Häberle, D. Schmid-Lorch, F. Reinhard, and J. Wrachtrup. "Nanoscale Nuclear Magnetic Imaging with Chemical Contrast." In: *Nature Nanotechnology* 10.2 (Feb. 2015), pp. 125–128. DOI: 10.1038/nnano.2014.299 (cit. on pp. 1, 24, 43, 54, 62, 73).

[37] Bernhard Grotz, Johannes Beck, Philipp Neumann, Boris Naydenov, Rolf Reuter, Friedemann Reinhard, Fedor Jelezko, Jörg Wrachtrup, David Schweinfurth, Biprajit Sarkar, and Philip Hemmer. "Sensing External Spins with Nitrogen-Vacancy Diamond." In: *New Journal of Physics* 13.5 (May 1, 2011), p. 055004. DOI: 10.1088/1367-2630/13/5/055004 (cit. on p. 1).

[38] S. Steinert, F. Ziem, L. T. Hall, A. Zappe, M. Schweikert, N. Götz, A. Aird, G. Balasubramanian, L. Hollenberg, and J. Wrachtrup. "Magnetic Spin Imaging under Ambient Conditions with Sub-Cellular Resolution." In: *Nature Communications* 4 (Mar. 19, 2013), p. 1607. DOI: 10.1038/ncomms2588 (cit. on p. 1).

[39] Florestan C. Ziem, Nicolas S. Götz, Andrea Zappe, Steffen Steinert, and Jörg Wrachtrup. "Highly Sensitive Detection of Physiological Spins in a Microfluidic Device." In: *Nano Letters* 13.9 (Sept. 11, 2013), pp. 4093–4098. DOI: 10.1021/nl401522a (cit. on p. 1).

[40] Fazhan Shi, Qi Zhang, Pengfei Wang, Hongbin Sun, Jiarong Wang, Xing Rong, Ming Chen, Chenyong Ju, Friedemann Reinhard, Hongwei Chen, Jörg Wrachtrup, Junfeng Wang, and Jiangfeng Du. "Single-Protein Spin Resonance Spectroscopy under Ambient Conditions." In: *Science* 347.6226 (June 3, 2015), pp. 1135–1138. DOI: 10.1126/science.aaa2253. pmid: 25745170 (cit. on p. 1).

[41] M. Werner and R. Locher. "Growth and Application of Undoped and Doped Diamond Films." In: *Reports on Progress in Physics* 61.12 (1998), p. 1665. DOI: 10.1088/0034-4885/61/12/002 (cit. on p. 1).

[42] J Walker. "Optical Absorption and Luminescence in Diamond." In: *Reports on Progress in Physics* 42.10 (Oct. 1, 1979), pp. 1605–1659. DOI: 10.1088/0034-4885/42/10/001 (cit. on p. 1).

[43] F. P. Bundy, H. T. Hall, H. M. Strong, and R. H. Wentorf Jun. "Man-Made Diamonds." In: *Nature* 176.4471 (July 1955), pp. 51–55. DOI: 10.1038/176051a0 (cit. on p. 2).

[44] Jan Isberg, Johan Hammersberg, Erik Johansson, Tobias Wikström, Daniel J. Twitchen, Andrew J. Whitehead, Steven E. Coe, and Geoffrey A. Scarsbrook. "High Carrier Mobility in Single-Crystal Plasma-Deposited Diamond." In: *Science* 297.5587 (Sept. 6, 2002), pp. 1670–1672. DOI: 10.1126/science.1074374. pmid: 12215638 (cit. on p. 2).

[45] N. Mizuochi, J. Isoya, J. Niitsuma, T. Sekiguchi, H. Watanabe, H. Kato, T. Makino, H. Okushi, and S. Yamasaki. "Isotope Effects between Hydrogen and Deuterium Microwave Plasmas on Chemical Vapor Deposition Homoepitaxial Diamond Growth." In: *Journal of Applied Physics* 101.10 (May 15, 2007), p. 103501. DOI: 10.1063/1.2727380 (cit. on p. 2).

[46] G. Davies and M. F. Hamer. "Optical Studies of the 1.945 eV Vibronic Band in Diamond." In: *Proceedings of the Royal Society of London. A. Mathematical and Physical Sciences* 348.1653 (Feb. 24, 1976), pp. 285–298. DOI: 10.1098/rspa.1976.0039 (cit. on pp. 2, 3).

[47] Marcus W. Doherty, Neil B. Manson, Paul Delaney, Fedor Jelezko, Jörg Wrachtrup, and Lloyd C. L. Hollenberg. "The Nitrogen-Vacancy Colour Centre in Diamond." In: *Physics Reports*. The nitrogen-vacancy colour centre in diamond 528.1 (July 1, 2013), pp. 1–45. DOI: 10.1016/j.physrep.2013.02.001 (cit. on pp. 2, 5, 61).

[48] A. Gruber, A. Dräbenstedt, C. Tietz, L. Fleury, J. Wrachtrup, and C. von Borczyskowski. "Scanning Confocal Optical Microscopy and Magnetic Resonance on Single Defect Centers." In: *Science* 276.5321 (June 27, 1997), pp. 2012–2014. DOI: 10.1126/science.276.5321.2012 (cit. on pp. 2, 5).

[49] J. Meijer, B. Burchard, M. Domhan, C. Wittmann, T. Gaebel, I. Popa, F. Jelezko, and J. Wrachtrup. "Generation of Single Color Centers by Focused Nitrogen Implantation." In: *Applied Physics Letters* 87.26 (Dec. 21, 2005), p. 261909. DOI: 10.1063/1.2103389 (cit. on p. 3).

[50] J. R. Rabeau, P. Reichart, G. Tamanyan, D. N. Jamieson, S. Prawer, F. Jelezko, T. Gaebel, I. Popa, M. Domhan, and J. Wrachtrup. "Implantation of Labelled Single Nitrogen Vacancy Centers in Diamond Using N15." In: *Applied Physics Letters* 88.2 (Jan. 9, 2006), p. 023113. DOI: 10.1063/1.2158700 (cit. on pp. 3, 98).

[51] N.B. Manson and J.P. Harrison. "Photo-Ionization of the Nitrogen-Vacancy Center in Diamond." In: *Diamond and Related Materials* 14.10 (Oct. 2005), pp. 1705–1710. DOI: 10.1016/j.diamond.2005.06.027 (cit. on pp. 3, 29).

[52] T. Gaebel, M. Domhan, C. Wittmann, I. Popa, F. Jelezko, J. Rabeau, A. Greentree, S. Prawer, E. Trajkov, P.R. Hemmer, and J. Wrachtrup. "Photochromism in Single Nitrogen-Vacancy Defect in Diamond." In: *Applied Physics B: Lasers and Optics* 82.2 (2006), pp. 243–246. DOI: 10.1007/s00340-005-2056-2 (cit. on pp. 3, 29).

[53] Kyu Young Han, Seong Keun Kim, Christian Eggeling, and Stefan W. Hell. "Metastable Dark States Enable Ground State Depletion Microscopy of Nitrogen Vacancy Centers in Diamond with Diffraction-Unlimited Resolution." In: *Nano Letters* 10.8 (Aug. 11, 2010), pp. 3199–3203. DOI: 10.1021/nl102156m (cit. on p. 3).

[54] G. Waldherr, J. Beck, M. Steiner, P. Neumann, A. Gali, Th. Frauenheim, F. Jelezko, and J. Wrachtrup. "Dark States of Single Nitrogen-Vacancy Centers in Diamond Unraveled by Single Shot NMR." In: *Physical Review Letters* 106.15 (Apr. 14, 2011), p. 157601. DOI: 10.1103/PhysRevLett.106.157601 (cit. on pp. 3, 27, 31, 32, 34, 37, 40, 55, 58).

[55] N Aslam, G Waldherr, P Neumann, F Jelezko, and J Wrachtrup. "Photo-Induced Ionization Dynamics of the Nitrogen Vacancy Defect in Diamond Investigated by Single-Shot Charge State Detection." In: *New Journal of Physics* 15.1 (Jan. 31, 2013), p. 013064. DOI: 10.1088/1367-2630/15/1/013064 (cit. on pp. 3, 29, 31, 34, 56, 58).

[56] Matthias Pfender, Nabeel Aslam, Gerald Waldherr, Philipp Neumann, and Jörg Wrachtrup. "Single-Spin Stochastic Optical Reconstruction Microscopy." In: *Proceedings of the National Academy of Sciences* (Sept. 29, 2014), p. 201404907. DOI: 10.1073/pnas.1404907111. pmid: 25267655 (cit. on p. 3).

[57] Yuki Doi, Takahiro Fukui, Hiromitsu Kato, Toshiharu Makino, Satoshi Yamasaki, Toshiyuki Tashima, Hiroki Morishita, Shinji Miwa, Fedor Jelezko, Yoshishige Suzuki, and Norikazu Mizuochi. "Pure Negatively Charged State of the NV Center in n-Type Diamond." In: *Physical Review B* 93.8 (Feb. 3, 2016), p. 081203. DOI: 10.1103/PhysRevB.93.081203 (cit. on p. 3).

[58] A. Lenef and S. C. Rand. "Electronic Structure of the N-V Center in Diamond: Theory." In: *Physical Review B* 53.20 (May 15, 1996), pp. 13441–13455. DOI: 10.1103/PhysRevB.53.13441 (cit. on p. 5).

[59] P Neumann, R Kolesov, V Jacques, J Beck, J Tisler, A Batalov, L Rogers, N B Manson, G Balasubramanian, F Jelezko, and J Wrachtrup. "Excited-State Spectroscopy of Single NV Defects in Diamond Using Optically Detected Magnetic Resonance." In: *New Journal of Physics* 11.1 (Jan. 7, 2009), p. 013017. DOI: 10.1088/1367-2630/11/1/013017 (cit. on pp. 5, 25).

[60] A. T. Collins, M. F. Thomaz, and M. I. B. Jorge. "Luminescence Decay Time of the 1.945 eV Centre in Type Ib Diamond." In: *Journal of Physics C: Solid State Physics* 16.11 (1983), p. 2177. DOI: 10.1088/0022-3719/16/11/020 (cit. on p. 5).

[61] K. Jensen, N. Leefer, A. Jarmola, Y. Dumeige, V. M. Acosta, P. Kehayias, B. Patton, and D. Budker. "Cavity-Enhanced Room-Temperature Magnetometry Using Absorption by Nitrogen-Vacancy Centers in Diamond." In: *Physical Review Letters* 112.16 (Apr. 23, 2014), p. 160802. DOI: 10.1103/PhysRevLett.112.160802 (cit. on p. 5).

[62] L. J. Rogers, M. W. Doherty, M. S. J. Barson, S. Onoda, T. Ohshima, and N. B. Manson. "Singlet Levels of the NV - Centre in Diamond." In: *New Journal of Physics* 17.1 (2015), p. 013048. DOI: 10.1088/1367-2630/17/1/013048 (cit. on p. 5).

[63] N. B. Manson, J. P. Harrison, and M. J. Sellars. "Nitrogen-Vacancy Center in Diamond: Model of the Electronic Structure and Associated Dynamics." In: *Physical Review B* 74.10 (2006), p. 104303. DOI: 10.1103/PhysRevB.74.104303 (cit. on pp. 5, 61).

[64] V. M. Acosta, A. Jarmola, E. Bauch, and D. Budker. "Optical Properties of the Nitrogen-Vacancy Singlet Levels in Diamond." In: *Physical Review B* 82.20 (Nov. 17, 2010), p. 201202. DOI: 10.1103/PhysRevB.82.201202 (cit. on p. 5).

[65] J Harrison, M. J Sellars, and N. B Manson. "Optical Spin Polarisation of the N-V Centre in Diamond." In: *Journal of Luminescence*. Proceedings of the 8th International Meeting on Hole Burning, Single Molecule, and Related Spectroscopies: Science and Applications 107.1 (May 1, 2004), pp. 245–248. DOI: 10.1016/j.jlumin.2003.12.020 (cit. on p. 5).

[66] Charles P. Slichter. *Principles of Magnetic Resonance*. 3rd ed. Springer Series in Solid-State Sciences. Berlin Heidelberg: Springer-Verlag, 1990 (cit. on p. 9).

[67] Philipp Neumann. "Towards a Room Temperature Solid State Quantum Processor - the Nitrogen-Vacancy Center in Diamond." In: (2012). DOI: http://dx.doi.org/10.18419/opus-5067 (cit. on pp. 11, 12, 25).

[68] Albert W. Overhauser. "Polarization of Nuclei in Metals." In: *Physical Review* 92.2 (Oct. 15, 1953), pp. 411–415. DOI: 10.1103/PhysRev.92.411 (cit. on p. 12).

[69] Stephen J. DeVience, Linh M. Pham, Igor Lovchinsky, Alexander O. Sushkov, Nir Bar-Gill, Chinmay Belthangady, Francesco Casola, Madeleine Corbett, Huiliang Zhang, Mikhail Lukin, Hongkun Park, Amir Yacoby, and Ronald L. Walsworth. "Nanoscale NMR Spectroscopy and Imaging of Multiple Nuclear Species." In: *Nature Nanotechnology* 10.2 (Feb. 2015), pp. 129–134. DOI: 10.1038/nnano.2014.313 (cit. on pp. 13, 24, 43, 54, 62).

[70] A. Jarmola, V. M. Acosta, K. Jensen, S. Chemerisov, and D. Budker. "Temperature- and Magnetic-Field-Dependent Longitudinal Spin Relaxation in Nitrogen-Vacancy Ensembles in Diamond." In: *Physical Review Letters* 108.19 (May 11, 2012). DOI: 10.1103/PhysRevLett.108.197601 (cit. on pp. 13, 38, 52, 55).

[71] E. L. Hahn. "Spin Echoes." In: *Physical Review* 80.4 (Nov. 15, 1950), pp. 580–594. DOI: 10.1103/PhysRev.80.580 (cit. on pp. 14, 18).

[72] Gopalakrishnan Balasubramanian, Philipp Neumann, Daniel Twitchen, Matthew Markham, Roman Kolesov, Norikazu Mizuochi, Junichi Isoya, Jocelyn Achard, Johannes Beck, Julia Tissler, Vincent Jacques, Philip R. Hemmer, Fedor Jelezko, and Jörg Wrachtrup. "Ultralong Spin Coherence Time in Isotopically Engineered Diamond." In: *Nature Materials* 8.5 (Apr. 6, 2009), pp. 383–387. DOI: 10.1038/nmat2420 (cit. on p. 17).

[73] Florian Rempp. "Decoherence Properties of the NV-Center in Diamond." In: *PhD Thesis (University of Stuttgart)* (2011) (cit. on p. 17).

[74] Lan Luan, Michael S. Grinolds, Sungkun Hong, Patrick Maletinsky, Ronald L. Walsworth, and Amir Yacoby. "Decoherence Imaging of Spin Ensembles Using a Scanning Single-Electron Spin in Diamond." In: *Scientific Reports* 5 (Jan. 29, 2015), p. 8119. DOI: 10.1038/srep08119 (cit. on p. 19).

[75] Zhi-Hui Wang and Susumu Takahashi. "Spin Decoherence and Electron Spin Bath Noise of a Nitrogen-Vacancy Center in Diamond." In: *Physical Review B* 87.11 (Mar. 15, 2013), p. 115122. DOI: 10.1103/PhysRevB.87.115122 (cit. on p. 19).

[76] Abdelghani Laraoui, Jonathan S. Hodges, and Carlos A. Meriles. "Magnetometry of Random Ac Magnetic Fields Using a Single Nitrogen-Vacancy Center." In: *Applied Physics Letters* 97.14 (Oct. 4, 2010), p. 143104. DOI: 10.1063/1.3497004 (cit. on p. 20).

[77] H. Y. Carr and E. M. Purcell. "Effects of Diffusion on Free Precession in Nuclear Magnetic Resonance Experiments." In: *Physical Review* 94.3 (May 1, 1954), pp. 630–638. DOI: 10.1103/PhysRev.94.630 (cit. on p. 20).

[78] S. Meiboom and D. Gill. "Modified Spin-Echo Method for Measuring Nuclear Relaxation Times." In: *Review of Scientific Instruments* 29.8 (Aug. 1, 1958), pp. 688–691. DOI: 10.1063/1.1716296 (cit. on p. 20).

[79] Alexandre M. Souza, Gonzalo A. Álvarez, and Dieter Suter. "Robust Dynamical Decoupling." In: *Philosophical Transactions of the Royal Society of London A: Mathematical, Physical and Engineering Sciences* 370.1976 (Oct. 13, 2012), pp. 4748–4769. DOI: 10.1098/rsta.2011.0355. pmid: 22946039 (cit. on p. 21).

[80] A. A Maudsley. "Modified Carr-Purcell-Meiboom-Gill Sequence for NMR Fourier Imaging Applications." In: *Journal of Magnetic Resonance (1969)* 69.3 (Oct. 1, 1986), pp. 488–491. DOI: 10.1016/0022-2364(86)90160-5 (cit. on p. 21).

[81] Terry Gullion, David B Baker, and Mark S Conradi. "New, Compensated Carr-Purcell Sequences." In: *Journal of Magnetic Resonance (1969)* 89.3 (Oct. 1, 1990), pp. 479–484. DOI: 10.1016/0022-2364(90)90331-3 (cit. on p. 21).

[82] Lorenza Viola, Emanuel Knill, and Seth Lloyd. "Dynamical Decoupling of Open Quantum Systems." In: *Physical Review Letters* 82.12 (Mar. 22, 1999), pp. 2417–2421. DOI: 10.1103/PhysRevLett.82.2417 (cit. on p. 21).

[83] M. J. Biercuk, A. C. Doherty, and H. Uys. "Dynamical Decoupling Sequence Construction as a Filter-Design Problem." In: *Journal of Physics B: Atomic, Molecular and Optical Physics* 44.15 (2011), p. 154002. DOI: 10.1088/0953-4075/44/15/154002 (cit. on pp. 21, 72).

[84] Abdelghani Laraoui, Florian Dolde, Christian Burk, Friedemann Reinhard, Jörg Wrachtrup, and Carlos A. Meriles. "High-Resolution Correlation Spectroscopy of 13C Spins near a Nitrogen-Vacancy Centre in Diamond." In: *Nature Communications* 4 (Apr. 3, 2013), p. 1651. DOI: 10.1038/ncomms2685 (cit. on pp. 22, 43, 44, 66, 71, 94).

[85] T. Staudacher, N. Raatz, S. Pezzagna, J. Meijer, F. Reinhard, C. A. Meriles, and J. Wrachtrup. "Probing Molecular Dynamics at the Nanoscale via an Individual Paramagnetic Centre." In: *Nature Communications* 6 (Oct. 12, 2015), p. 8527. DOI: 10.1038/ncomms9527 (cit. on pp. 22, 66, 71, 94).

[86] Xi Kong, Alexander Stark, Jiangfeng Du, Liam P. McGuinness, and Fedor Jelezko. "Towards Chemical Structure Resolution with Nanoscale Nuclear Magnetic Resonance Spectroscopy." In: *Physical Review Applied* 4.2 (Aug. 6, 2015), p. 024004. DOI: 10.1103/PhysRevApplied.4.024004 (cit. on pp. 22, 43, 44, 66, 71).

[87] Fei Xue, D. P. Weber, P. Peddibhotla, and M. Poggio. "Measurement of Statistical Nuclear Spin Polarization in a Nanoscale GaAs Sample." In: *Physical Review B* 84.20 (Nov. 21, 2011), p. 205328. DOI: 10.1103/PhysRevB.84.205328 (cit. on p. 23).

[88] G. Feher. "Observation of Nuclear Magnetic Resonances via the Electron Spin Resonance Line." In: *Physical Review* 103.3 (Aug. 1, 1956), pp. 834–835. DOI: 10.1103/PhysRev.103.834 (cit. on p. 24).

[89] K Iakoubovskii, G J Adriaenssens, and M Nesladek. "Photochromism of Vacancy-Related Centres in Diamond." In: *Journal of Physics: Condensed Matter* 12.2 (Jan. 17, 2000), pp. 189–199. DOI: 10.1088/0953-8984/12/2/308 (cit. on p. 29).

[90] I N Kupriyanov, V A Gusev, Yu N Pal'yanov, and Yu M Borzdov. "Photochromic Effect in Irradiated and Annealed Nearly IIa Type Synthetic Diamond." In: *Journal of Physics: Condensed Matter* 12.35 (Sept. 4, 2000), pp. 7843–7856. DOI: 10.1088/0953-8984/12/35/318 (cit. on p. 29).

[91] J. W. Steeds, S. J. Charles, J. Davies, and I. Griffin. "Photoluminescence Microscopy of TEM Irradiated Diamond." In: *Diamond and Related Materials* 9.3 (Apr. 1, 2000), pp. 397–403. DOI: 10.1016/S0925-9635(99)00360-X (cit. on p. 29).

[92] M. V. Hauf, B. Grotz, B. Naydenov, M. Dankerl, S. Pezzagna, J. Meijer, F. Jelezko, J. Wrachtrup, M. Stutzmann, F. Reinhard, and J. A. Garrido. "Chemical Control of the Charge State of Nitrogen-Vacancy Centers in Diamond." In: *Physical Review B* 83.8 (Feb. 14, 2011), p. 081304. DOI: 10.1103/PhysRevB.83.081304 (cit. on pp. 29, 40).

[93] G. Waldherr, P. Neumann, S. F. Huelga, F. Jelezko, and J. Wrachtrup. "Violation of a Temporal Bell Inequality for Single Spins in a Diamond Defect Center." In: *Physical Review Letters* 107.9 (Aug. 24, 2011), p. 090401. DOI: 10.1103/PhysRevLett.107.090401 (cit. on pp. 29, 38).

[94] J. Cramer, N. Kalb, M. A. Rol, B. Hensen, M. S. Blok, M. Markham, D. J. Twitchen, R. Hanson, and T. H. Taminiau. "Repeated Quantum Error Correction on a Continuously Encoded Qubit by Real-Time Feedback." In: *Nature Communications* 7 (May 5, 2016), p. 11526. DOI: 10.1038/ncomms11526 (cit. on p. 29).

[95] B. Hensen, H. Bernien, A. E. Dréau, A. Reiserer, N. Kalb, M. S. Blok, J. Ruitenberg, R. F. L. Vermeulen, R. N. Schouten, C. Abellán, W. Amaya, V. Pruneri, M. W. Mitchell, M. Markham, D. J. Twitchen, D. Elkouss, S. Wehner, T. H. Taminiau, and R. Hanson. "Loophole-Free Bell Inequality Violation Using Electron Spins Separated by 1.3 Kilometres." In: *Nature* 526.7575 (Oct. 29, 2015), pp. 682–686. DOI: 10.1038/nature15759 (cit. on p. 29).

[96] Wolfgang Pfaff, Tim H. Taminiau, Lucio Robledo, Hannes Bernien, Matthew Markham, Daniel J. Twitchen, and Ronald Hanson. "Demonstration of Entanglement-by-Measurement of Solid-State Qubits." In: *Nature Physics* 9.1 (Jan. 2013), pp. 29–33. DOI: 10.1038/nphys2444 (cit. on p. 29).

[97] I Jakobi, S A Momenzadeh, F Fávaro de Oliveira, J Michl, F Ziem, M Schreck, P Neumann, A Denisenko, and J Wrachtrup. "Efficient Creation of Dipolar Coupled Nitrogen-Vacancy Spin Qubits in Diamond." In: *Journal of Physics: Conference Series* 752 (Sept. 2016), p. 012001. DOI: 10.1088/1742-6596/752/1/012001 (cit. on p. 29).

[98] John J. L. Morton, Alexei M. Tyryshkin, Richard M. Brown, Shyam Shankar, Brendon W. Lovett, Arzhang Ardavan, Thomas Schenkel, Eugene E. Haller, Joel W. Ager, and S. A. Lyon. "Solid-State Quantum Memory Using the 31P Nuclear Spin." In: *Nature* 455.7216 (Oct. 23, 2008), pp. 1085–1088. DOI: 10.1038/nature07295 (cit. on pp. 29, 39, 41).

[99] Kamyar Saeedi, Stephanie Simmons, Jeff Z. Salvail, Phillip Dluhy, Helge Riemann, Nikolai V. Abrosimov, Peter Becker, Hans-Joachim Pohl, John J. L. Morton, and Mike L. W. Thewalt. "Room-Temperature Quantum Bit Storage Exceeding 39 Minutes Using Ionized Donors in Silicon-28." In: *Science* 342.6160 (Nov. 15, 2013), pp. 830–833. DOI: 10.1126/science.1239584. pmid: 24233718 (cit. on pp. 29, 39, 41).

[100] Andrea Morello, Jarryd J. Pla, Floris A. Zwanenburg, Kok W. Chan, Kuan Y. Tan, Hans Huebl, Mikko Möttönen, Christopher D. Nugroho, Changyi Yang, Jessica A. van Donkelaar, Andrew D. C. Alves, David N. Jamieson, Christopher C. Escott, Lloyd C. L. Hollenberg, Robert G. Clark, and Andrew S. Dzurak. "Single-Shot Readout of an Electron Spin in Silicon." In: *Nature* 467.7316 (Oct. 7, 2010), pp. 687–691. DOI: 10.1038/nature09392. pmid: 20877281 (cit. on pp. 29, 39, 41).

[101] Jarryd J. Pla, Kuan Y. Tan, Juan P. Dehollain, Wee H. Lim, John J. L. Morton, Floris A. Zwanenburg, David N. Jamieson, Andrew S. Dzurak, and Andrea Morello. "High-Fidelity Readout and Control of a Nuclear Spin Qubit in Silicon." In: *Nature* 496.7445 (Apr. 18, 2013), pp. 334–338. DOI: 10.1038/nature12011. pmid: 23598342 (cit. on pp. 29, 39, 41).

[102] S. Felton, A. M. Edmonds, M. E. Newton, P. M. Martineau, D. Fisher, and D. J. Twitchen. "Electron Paramagnetic Resonance Studies of the Neutral Nitrogen Vacancy in Diamond." In: *Physical Review B* 77.8 (Feb. 6, 2008), p. 081201. DOI: 10.1103/PhysRevB.77.081201 (cit. on p. 32).

[103] Sebastian Zaiser, Torsten Rendler, Ingmar Jakobi, Thomas Wolf, Sang-Yun Lee, Samuel Wagner, Ville Bergholm, Thomas Schulte-Herbrüggen, Philipp Neumann, and Jörg Wrachtrup. "Enhancing Quantum Sensing Sensitivity by a Quantum Memory." In: *Nature Communications* 7 (Aug. 10, 2016), p. 12279. DOI: 10.1038/ncomms12279 (cit. on pp. 38, 43, 44, 46).

[104] P. C. Maurer, G. Kucsko, C. Latta, L. Jiang, N. Y. Yao, S. D. Bennett, F. Pastawski, D. Hunger, N. Chisholm, M. Markham, D. J. Twitchen, J. I. Cirac, and M. D. Lukin. "Room-Temperature Quantum Bit Memory Exceeding One Second." In: *Science* 336.6086 (Aug. 6, 2012), pp. 1283–1286. DOI: 10.1126/science.1220513 (cit. on pp. 38, 55, 56, 58, 88).

[105] Felipe Fávaro de Oliveira, S. Ali Momenzadeh, Denis Antonov, Jochen Scharpf, Christian Osterkamp, Boris Naydenov, Fedor Jelezko, Andrej Denisenko, and Jörg Wrachtrup. "Toward Optimized Surface δ-Profiles of Nitrogen-Vacancy Centers Activated by Helium Irradiation in Diamond." In: *Nano Letters* 16.4 (Apr. 13, 2016), pp. 2228–2233. DOI: 10.1021/acs.nanolett.5b04511 (cit. on p. 40).

[106] Felipe Fávaro de Oliveira, Seyed Ali Momenzadeh, Denis Antonov, Helmut Fedder, Andrej Denisenko, and Jörg Wrachtrup. "On the Efficiency of Combined Ion Implantation for the Creation of Near-Surface Nitrogen-Vacancy Centers in Diamond." In: *physica status solidi (a)* 213.8 (Aug. 1, 2016), pp. 2044–2050. DOI: 10.1002/pssa.201600326 (cit. on p. 40).

[107] B. K. Ofori-Okai, S. Pezzagna, K. Chang, M. Loretz, R. Schirhagl, Y. Tao, B. A. Moores, K. Groot-Berning, J. Meijer, and C. L. Degen. "Spin Properties of Very Shallow Nitrogen Vacancy Defects in Diamond." In: *Physical Review B* 86.8 (Aug. 13, 2012), p. 081406. DOI: 10.1103/PhysRevB.86.081406 (cit. on p. 40).

[108] Y. Romach, C. Müller, T. Unden, L. J. Rogers, T. Isoda, K. M. Itoh, M. Markham, A. Stacey, J. Meijer, S. Pezzagna, B. Naydenov, L. P. McGuinness, N. Bar-Gill, and F. Jelezko. "Spectroscopy of Surface-Induced Noise Using Shallow Spins in Diamond." In: *Physical Review Letters* 114.1 (Jan. 6, 2015), p. 017601. DOI: 10.1103/PhysRevLett.114.017601 (cit. on p. 40).

[109] C. Schreyvogel, V. Polyakov, R. Wunderlich, J. Meijer, and C. E. Nebel. "Active Charge State Control of Single NV Centres in Diamond by In-Plane Al-Schottky Junctions." In: *Scientific Reports* 5 (July 16, 2015), p. 12160. DOI: 10.1038/srep12160 (cit. on p. 40).

[110] Christoph Schreyvogel, Vladimir Polyakov, Sina Burk, Helmut Fedder, Andrej Denisenko, Felipe Fávaro de Oliveira, Ralf Wunderlich, Jan Meijer, Verena Zuerbig, Jörg Wrachtrup, and Christoph E Nebel. "Active and Fast Charge-State Switching of Single NV Centres in Diamond by in-Plane Al-Schottky Junctions." In: *Beilstein Journal of Nanotechnology* 7 (Nov. 16, 2016), pp. 1727–1735. DOI: 10.3762/bjnano.7.165. pmid: 28144522 (cit. on pp. 40, 41).

[111] M. I. Landstrass and K. V. Ravi. "Resistivity of Chemical Vapor Deposited Diamond Films." In: *Applied Physics Letters* 55.10 (Sept. 4, 1989), pp. 975–977. DOI: 10.1063/1.101694 (cit. on p. 40).

[112] B. E. Kane. "A Silicon-Based Nuclear Spin Quantum Computer." In: *Nature* 393.6681 (May 14, 1998), pp. 133–137. DOI: 10.1038/30156 (cit. on p. 41).

[113] Marcus W. Doherty, Viktor V. Struzhkin, David A. Simpson, Liam P. McGuinness, Yufei Meng, Alastair Stacey, Timothy J. Karle, Russell J. Hemley, Neil B. Manson, Lloyd C. L. Hollenberg, and Steven Prawer. "Electronic Properties and Metrology Applications of the Diamond NV- Center under Pressure." In: *Physical Review Letters* 112.4 (Jan. 31, 2014), p. 047601. DOI: 10.1103/PhysRevLett.112.047601 (cit. on p. 43).

[114] Kurt Wüthrich. *The Way to NMR Structures of Proteins*. Nov. 1, 2001. URL: https://www.nature.com/articles/nsb1101-923 (visited on 07/10/2018) (cit. on pp. 43, 63, 86).

[115] Hartmut Oschkinat, Christian Griesinger, Per J. Kraulis, Ole W. Sørensen, Richard R. Ernst, Angela M. Gronenborn, and G. Marius Clore. "Three-Dimensional NMR Spectroscopy of a Protein in Solution." In: *Nature* 332.6162 (Mar. 1988), pp. 374–376. DOI: 10.1038/332374a0 (cit. on pp. 43, 63, 86).

[116] W. P. Aue, E. Bartholdi, and R. R. Ernst. "Two-dimensional Spectroscopy. Application to Nuclear Magnetic Resonance." In: *The Journal of Chemical Physics* 64.5 (Mar. 1, 1976), pp. 2229–2246. DOI: 10.1063/1.432450 (cit. on pp. 43, 63, 86).

[117] Michael A. Nielsen and Isaac L. Chuang. *Quantum Computation and Quantum Information*. Cambridge ; New York: Cambridge University Press, Oct. 23, 2000. 700 pp. (cit. on p. 53).

[118] J. R. Johansson, P. D. Nation, and Franco Nori. "QuTiP 2: A Python Framework for the Dynamics of Open Quantum Systems." In: *Computer Physics Communications* 184.4 (Apr. 1, 2013), pp. 1234–1240. DOI: 10.1016/j.cpc.2012.11.019 (cit. on p. 53).

[119] Adam Gali. "Theory of the Neutral Nitrogen-Vacancy Center in Diamond and Its Application to the Realization of a Qubit." In: *Physical Review B* 79.23 (June 30, 2009), p. 235210. DOI: 10.1103/PhysRevB.79.235210 (cit. on p. 55).

[120] A. Abragam and M. Goldman. *Nuclear Magnetism: Order and Disorder*. First Edition edition. Oxford : New York: Oxford University Press, May 20, 1982. 626 pp. (cit. on pp. 65, 66).

[121] Tobias Rosskopf, Jonathan Zopes, Jens M. Boss, and Christian L. Degen. "A Quantum Spectrum Analyzer Enhanced by a Nuclear Spin Memory." In: *npj Quantum Information* 3.1 (Aug. 30, 2017), p. 33. DOI: 10.1038/s41534-017-0030-6 (cit. on p. 68).

[122] Simon Schmitt, Tuvia Gefen, Felix M. Stürner, Thomas Unden, Gerhard Wolff, Christoph Müller, Jochen Scheuer, Boris Naydenov, Matthew Markham, Sebastien Pezzagna, Jan Meijer, Ilai Schwarz, Martin Plenio, Alex Retzker, Liam P. McGuinness, and Fedor Jelezko. "Submillihertz Magnetic Spectroscopy Performed with a Nanoscale Quantum Sensor." In: *Science* 356.6340 (May 26, 2017), pp. 832–837. DOI: 10.1126/science.aam5532. pmid: 28546208 (cit. on pp. 71, 74, 75, 85).

[123] J. M. Boss, K. S. Cujia, J. Zopes, and C. L. Degen. "Quantum Sensing with Arbitrary Frequency Resolution." In: *Science* 356.6340 (May 26, 2017), pp. 837–840. DOI: 10.1126/science.aam7009. pmid: 28546209 (cit. on pp. 71, 74, 75).

[124] David R. Glenn, Dominik B. Bucher, Junghyun Lee, Mikhail D. Lukin, Hongkun Park, and Ronald L. Walsworth. "High-Resolution Magnetic Resonance Spectroscopy Using a Solid-State Spin Sensor." In: *Nature* 555.7696 (Mar. 2018), pp. 351–354. DOI: 10.1038/nature25781 (cit. on p. 71).

[125] Yakir Aharonov, David Z. Albert, and Lev Vaidman. "How the Result of a Measurement of a Component of the Spin of a Spin-1/2 Particle Can Turn out to Be 100." In: *Physical Review Letters* 60.14 (Apr. 4, 1988), pp. 1351–1354. DOI: 10.1103/PhysRevLett.60.1351 (cit. on p. 72).

[126] Wen-Long Ma and Ren-Bao Liu. "Angstrom-Resolution Magnetic Resonance Imaging of Single Molecules via Wave-Function Fingerprints of Nuclear Spins." In: *Physical Review Applied* 6.2 (Aug. 26, 2016), p. 024019. DOI: 10.1103/PhysRevApplied.6.024019 (cit. on pp. 77, 81).

[127] Carlo Presilla, Roberto Onofrio, and Ubaldo Tambini. "Measurement Quantum Mechanics and Experiments on Quantum Zeno Effect." In: *Annals of Physics* 248.1 (May 25, 1996), pp. 95–121. DOI: 10.1006/aphy.1996.0052 (cit. on pp. 80, 85).

[128] Wayne M. Itano, D. J. Heinzen, J. J. Bollinger, and D. J. Wineland. "Quantum Zeno Effect." In: *Physical Review A* 41.5 (Mar. 1, 1990), pp. 2295–2300. DOI: 10.1103/PhysRevA.41.2295 (cit. on pp. 80, 85).

[129] Alexander N. Korotkov. "Selective Quantum Evolution of a Qubit State Due to Continuous Measurement." In: *Physical Review B* 63.11 (Feb. 23, 2001), p. 115403. DOI: 10.1103/PhysRevB.63.115403 (cit. on p. 80).

[130] Andrew N. Jordan and Markus Büttiker. "Quantum Nondemolition Measurement of a Kicked Qubit." In: *Physical Review B* 71.12 (Mar. 29, 2005), p. 125333. DOI: 10.1103/PhysRevB.71.125333 (cit. on p. 80).

[131] Andrew N. Jordan and Alexander N. Korotkov. "Qubit Feedback and Control with Kicked Quantum Nondemolition Measurements: A Quantum Bayesian Analysis." In: *Physical Review B* 74.8 (Aug. 9, 2006), p. 085307. DOI: 10.1103/PhysRevB.74.085307 (cit. on p. 80).

[132] Alexandre M. Souza, Gonzalo A. Álvarez, and Dieter Suter. "Robust Dynamical Decoupling for Quantum Computing and Quantum Memory." In: *Physical Review Letters* 106.24 (June 14, 2011), p. 240501. DOI: 10.1103/PhysRevLett.106.240501 (cit. on pp. 80, 81).

[133] Gang-Qin Liu, Jian Xing, Wen-Long Ma, Ping Wang, Chang-Hao Li, Hoi Chun Po, Yu-Ran Zhang, Heng Fan, Ren-Bao Liu, and Xin-Yu Pan. "Single-Shot Readout of a Nuclear Spin Weakly Coupled to a Nitrogen-Vacancy Center at Room Temperature." In: *Physical Review Letters* 118.15 (Apr. 12, 2017), p. 150504. DOI: 10.1103/PhysRevLett.118.150504 (cit. on p. 81).

[134] L. Jiang, J. S. Hodges, J. R. Maze, P. Maurer, J. M. Taylor, D. G. Cory, P. R. Hemmer, R. L. Walsworth, A. Yacoby, A. S. Zibrov, and M. D. Lukin. "Repetitive Readout of a Single Electronic Spin via Quantum Logic with Nuclear Spin Ancillae." In: *Science* 326.5950 (Sept. 10, 2009), pp. 267–272. DOI: 10.1126/science.1176496. pmid: 19745117 (cit. on p. 88).

[135] Tuvia Gefen, Maxim Khodas, Liam P. McGuinness, Fedor Jelezko, and Alex Retzker. "Quantum Spectroscopy of Single Spins Assisted by a Classical Clock." In: *Physical Review A* 98.1 (July 27, 2018), p. 013844. DOI: 10.1103/PhysRevA.98.013844 (cit. on pp. 91, 93).

Acknowledgments

First of all, I would like to thank Prof. Jörg Wrachtrup for giving me the opportunity to do my PhD thesis on a very interesting project, combining techniques of quantum information processing with nanoscale metrology.
I also thank Prof. Sebastian Loth for taking the time to evaluate this thesis, as well as Prof. Maria Daghofer for chairing my PhD defense.
Furthermore, one cannot overestimate the contribution by Philipp Neumann, who, with wit and spirit, kept me and other PhD students focused and on track. Thank you for this!
During my time at the 3. Institute of Physics, for my Diploma as well as my PhD thesis, I always worked on projects together with Nabeel Aslam. I am glad to have found a friend as a colleague, with whom even heated arguments were possible.
For a PhD student, the every day job does for the most part not consist of physics, but rather of technical problems of different kinds. And when things are not working as one wants, help could always be found in the office. Nabeel Aslam, Sebastian Zaiser and Nikolas Abt were not only capable in assisting with problems, but also created a comfortable environment to work in.
I would also like to thank other members of the institute, who contributed to my thesis. First and foremost, Andrej Denisenko, Rolf Reuter and Andrea Zappe come to mind. For technical advise, Matthias Niethammer, Torsten Rendler and Matthias Widmann always were a good place to go to. Discussions about physics and life in general could always be held with Jan Honert, Thomas Oeckinghaus, Thomas Häberle, Dominik Schmid-Lorch, Andreas Brunner, Julia Michl, Ingmar Jakobi, Florestan Ziem, Sina Burk, Farida Shagieva, Nathan Chejanovsky, Ilja Gerhardt, Thomas Wolf, Denis Antonov, Durga Dasari, Amit Finkler, Sen Yang, Felipe Fávaro de Oliveiry, Ali Momenzadeh and Roland Nagy.
As is the case with scientific articles, people named last are not insignificant, but indeed the ones who keep things running. In that sense, I would like to thank Claudia Unger, Britta Lenz, Stephan Hirschmann, Ivanka Spajic, Joachim Lefèvre, Bernd Stobel and Dario Profetto.

During my thesis, I furthermore had help from national, as well as international collaborators. My thanks to Moritz Hauf, Patrick Simon, Marc Scheffler, Junichi Isoya, Liang Jin, Ren-Bao Liu, Adam Gali, Tokuyuki Teraji, Marcus Doherty, Carlos A. Meriles, Ping

Wang and Wen Yang.

At this point, I would also like to thank my friends and family[1]. During most of the work at the 3. Institute of Physics, I lived in a four persons WG. I could not imagine better flatmates than Arne Brien, Daniel Pavelka, Timo Frey, Hannes Krieger, Moritz Kappler and Lukas Ostrowski, when it comes to getting my mind of work, even if just for a few hours.

Moving out of this apartment was no easy choice, and was only enabled by the opportunity to move in with my girlfriend Ann-Sophie, whom I love and cherish greatly.

Another constant during this time was my family[2]. I'd like to thank my parents Roland and Gabi, my brothers Ralph and Marius, for their constant support and help.

[1]Even though many of the people named above could be mentioned here, I'll refrain from writing their names a second time.

[2]Actually, they have been a constant for a much longer time.

Hiermit versichere ich, dass ich die vorliegende Arbeit selbstständig verfasst habe und keine anderen als die angegeben Quellen und Hilfsmittel benutzt habe, dass alle Stellen der Arbeit, die wörtlich oder sinngemäß aus den Quellen entnommen wurden kenntlich gemacht wurden und dass diese Arbeit in gleicher oder ähnlicher Form noch keiner Prüfungsbehörde vorgelegt wurde.

Stuttgart, den

Matthias Pfender